Development of Cellular and Tissue Models to Simulate the Effect of Fibroblast-Myocyte Coupling on Cardiac Pacemaking and Conduction

A thesis submitted to The University of Manchester

for the degree of Master of Philosophy

in the Faculty of Engineering and Physical Science

2016

Le Qiao

School of Physics and Astronomy

Contents

List of Tables

List of Figures

Abstract

The University of Manchester,
Le Qiao
Degree Program: Master of Philosophy
Thesis Title: Development of Cellular and Tissue Models to Simulate the Effect of Fibroblast-Myocyte Coupling on Cardiac Pacemaking and Conduction
Date of Submission: 01 July 2016

Constituting 90-95% of the cardiac non-myocyte cell population, cardiac fibroblasts can electrically couple to cardiac myocytes by forming gap junctions. The electrical interaction between cardiac myocytes and fibroblasts plays a vital role in cardiac fibrosis and arrhythmia related heart disease.

In this thesis, cellular models of fibroblast-myocyte coupling in the rabbit sinoatrial node (SAN) and atrium were developed to explore the mechanism underlying the coupling. The effects of coupling fibroblast number and coupling strength between fibroblast and myocyte on electrical activities of the coupled myocyte were also investigated. 2D SAN-atrium tissue models with fibroblasts coupled in different ways were then developed to investigate the effects of the coupling fibroblast number and coupling strength on action potential initiation and propagation in cardiac tissue.

Our simulation found that the coupling exerts significant effects on the action potential (AP) waveform of coupled myocyte in the SAN centre under weak coupling (the gap junction conductance (G_{gap}) is less than 0.2 nS), showing a smaller action potential amplitude (APA), a less negative maximum diastolic potential (MDP), a shortened APD_{90}, and a decreased dV/dt_{max} after coupling with a larger G_{gap} or more fibroblasts. Moreover, the spontaneous activity in the SAN centre is abolished under strong coupling ($G_{gap} > 1$ nS). In contrast, there is no significant changes in AP characteristics of coupled myocytes in the SAN periphery and atrium under weak coupling. The APD_{90} increases along with the coupling fibroblast number or G_{gap} in atrium and SAN periphery under strong coupling. In the 2D tissue model, the conduction velocity (CV) increases in coupling regions after coupling with a larger G_{gap} or more fibroblasts in the attachment models. However, it increases in the SAN centre and decreases in the SAN periphery and atrium in the insertion models. Conduction blocks can be observed in both models after coupling with a certain number of fibroblasts. Therefore, fibroblasts are not only able to modulate the electrical activities of individual cells but also can modify the pacemaking activities and the AP conduction in cardiac tissue. However, the extent of changes is highly dependent on the electrophysiological properties of coupled myocytes, coupling fibroblast number and coupling strength between the myocyte and the fibroblast.

Declaration

I declare that no portion of the work referred to in the thesis has been submitted in support of an application for another degree or qualification of this or any other university or other institute of learning.

Copyright

Acknowledgements

First and foremost, I would like to express my heartfelt thanks to supervisor Prof. Henggui Zhang for his supervision and invaluable advice on my thesis. Without his support and guidance, I would never be able to finish this project. Moreover, I really appreciate the warm help from my colleagues, Haibo, Ruoxi, Shanzhuo, Weijian and Yang during my MPhil study in the biophysics group. Finally, a big thank you to my parents, Xu Qiao and Xiuxiu Song, for their love and support for all those years.

Acronyms

AP	Action Potential
APA	Action Potential Amplitude
APD	Action Potential Duration
APD_{50}	AP Duration at 50% Repolarization
APD_{90}	AP Duration at 90% Repolarization
AT	Activation Time
AVN	Atrioventricular Node
Cf	Cardiac Fibroblast
CL	Cycle Length
C_m	Cell Membrane Capacitance
CSAN	SAN Centre
CT	Crista Terminalis
CV	Conduction Velocity
CX	Connexin
dV/dt_{max}	Maximum Upstroke Velocity of AP
ECM	Extracellular Matrix
Endo	Endocardium
Epi	Epicardium
FASN	Model with Fibroblasts Attached in the Sinoatrial Node Centre
FAT	Model with Fibroblasts Attached in the Whole Tissue
FIT	Model with Fibroblasts Inserted in the Whole Tissue
FDM	Finite Difference Method

FISN	Model with Fibroblasts Inserted in the Sinoatrial Node Centre
G_f	Membrane Capacitance of the Fibroblast
G_{gap}	Gap Junction Conductance
I_{bCa}	Background Ca^{2+} Current
I_{bK}	Background K^+ Current
I_{bNa}	Background Na^+ Current
I_{CaL}	L-Type Inward Ca^{2+} Current
Icap	Sarcoplasmic Ca^{2+} Pump Current
I_{CaT}	T-Type Inward Ca^{2+} current
Igap	Gap Junction Current
I_{K1}	Inward Rectifier K^+ Current
I_{Kr}	Rapid Delayed Rectifier K^+ Current
I_{Ks}	Slow Delayed Rectifier K^+ Current
I_{Kur}	Ultra Rapid Delayed Rectifier K^+ Current
I_{kv}	Time and Voltage-Dependent Fibroblast K^+ Current
I_{Na}	Fast Inward Na^+ Current
I_{NaCa}	Na^+-Ca^{2+} Pump Current
I_{NaK}	Na^+-K^+ Pump Current
I_{to}	Transient Outward K^+ Current
IVC	Inferior Vena Cava
LV	Left Ventricle
MDP	Maximum Diastolic Potential
MV	Mitral Valve

NCX	Na^+-Ca^{2+} Exchanger
ODE	Ordinary Differential Equation
PA	Peak Action Potential
PF	Purkinje Fibre
PSAN	SAN Periphery
RA	Right Atrial Appendage
R_I	Membrane Resistance of ‘Leak Current'
R_K	Membrane Resistance of K^+
RMP	Resting Membrane Potential
R_{Na}	Membrane Resistance Of Na^+
RV	Right Ventricle
SAN	Sinoatrial Node
SEP	Interatrial Septum
SVC	Superior Vena Cave
TV	Tricuspid Valve
V_f	Membrane Potential of the Fibroblast
V_m	Membrane Potential of the Myocyte

Chapter 1. Introduction

1.1 Cardiac Anatomy and Physiology

1.1.1 The Heart

The heart is the core component in the circulatory system of human and other animals, pumping oxygenated blood around the whole body and deoxygenated blood to the lungs by periodic contractions [1]. The human heart normally weighs between 250 and 350 g [2], [3] and is located approximately in the middle of the chest between the two lungs. As shown in Figure 1.1, the heart is divided by a muscular wall (the septum) into two functionally distinct pumps: the left heart and right heart. The tricuspid valve separates the right heart into the right atrium and ventricle, and the mitral valve separates the left heart into the left atrium and ventricle. The right atrium collects the deoxygenated blood from the whole body through the superior and inferior vena cava and then passes it into the lower right ventricle, where it is pumped into the lungs through the pulmonary artery. The blood is oxygenated by releasing the carbon dioxide in the lungs and it then flows into the left atrium through the pulmonary veins. The oxygenated blood finally circulates into the left ventricle, where it is pumped to the whole body through the aorta.

1.1.2 The Sinoatrial Node

The sinoatrial node (SAN) is the natural pacemaker of the heart, first discovered by Martin Flack in a mole's heart in 1907 [4]. In 1963, Trautwein and Uchizono reported the relationships between the function and anatomy of the SAN for the first time [5]. As shown in Figure 1.2, The SAN lies at the junction of the crista terminalis (CT) and the intercaval near the opening of superior vena cava (SVC).

The SAN is a complex heterogeneous tissue that mainly contains fibroblasts and collagen [6]. No obvious border has been found between the SAN and the surrounding atrial muscle [7], [8]. From the centre to the periphery of the SAN, the shape and size as well as the arrangement of the cells change gradually and become more similar to the cells in the surrounding atrial muscle. As shown in Figure 1.2B and C, the stippled area represents the small interweaving SAN cell region (SAN centre), the yellow area indicates the large transitional SAN cell region, and the dashed yellow line indicates the peripheral SAN tissue, where SAN cells intermingle with atrial cells.

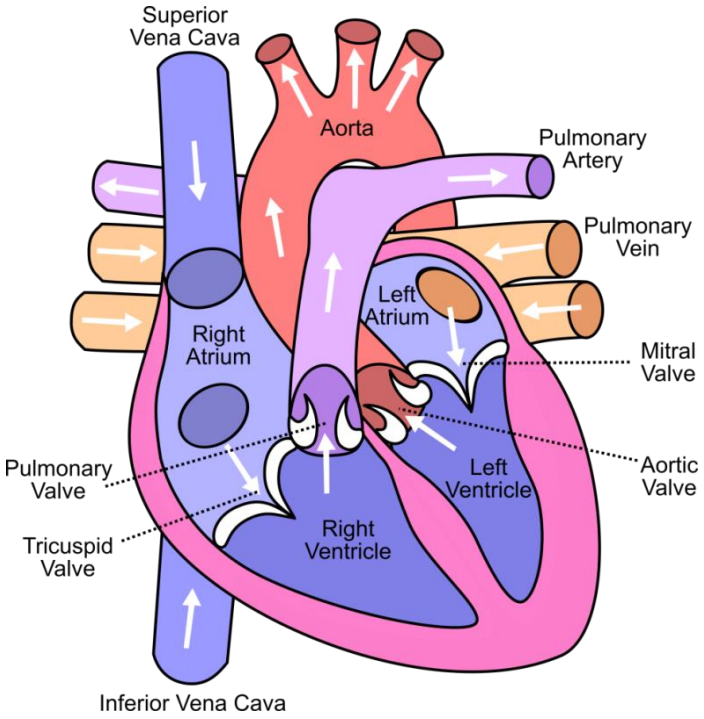

Figure 1.1 Schematic diagram of the gross anatomy of the human heart. Major structures and blood vessels are labelled. Arrows imply the directions of the blood flow. Adapted from Wikimedia Commons and created by Wapcaplet in Sodipodi. The file is licensed under the 'Creative Commons Attribution-Share Alike 3.0 Unported' license.

1.1.3 The Cardiac Myocyte

Cardiac myocytes (Figure 1.3A) are the muscle cells that form the chambers of the heart, constituting the majority of the myocardial mass. The size and shape of the cardiac myocytes vary in different organs in different species, it has been found that the cardiac myocytes are typically cylindrical and have a length of about 100-130 µm in rat and guinea pig ventricle [9], a length of around 100 µm in rabbit ventricle [10], a length of roughly 50 to 150 µm and a diameter of 5 to 10 µm in human heart [11], and a length of around 25 to 30 µm and a diameter of < 8 µm in rabbit SAN [12]. Cardiac myocytes are connected via intercalated disc bridges (porous gap junctions), which allows the ionic currents to diffuse from cell to cell, forming a strong mechanical and electrical connection between the neighbouring cells in the myocardium [13]. Gap junctions are composed of connexin (Cx) proteins. The most abundant gap junctional protein that has been found in the working myocardium is connexin43 (Cx43); other Cxs such as Cx40 and Cx45 are also present in the atrial tissue and pacemaker, which

together with Cx43 play an important role in AP propagation [14]–[16].

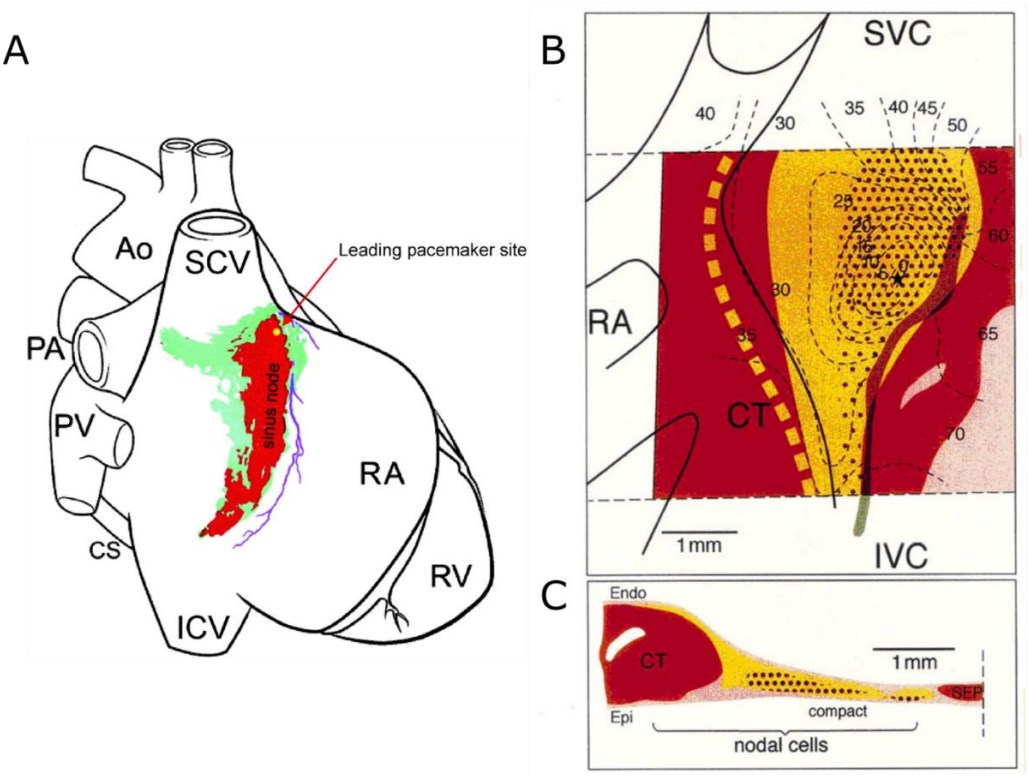

Figure 1.2 Schematic diagram of SAN location in the heart and histology of rabbit SAN. (A) A dorsal view of rabbit heart showing location and extent of central (red) and peripheral (green) sinus node tissue; the yellow dot is the leading pacemaker site [17]. (B) An endocardial view of SAN–atrial muscle preparation. (C) A cross section through the crista terminalis and intercaval region [7]. The star represents the leading pacemaker site. The dark yellow represents the SAN cells. The dashed yellow line represents the extent of SAN tissue overlying the atrial muscle of the crista terminalis. The brown area represents the atrial muscle. The pink region indicates the connective tissue. The stippled area indicates the interweaving SAN cells. The grey area represents the block zone. The superior vena cava (SVC or SCV), interatrial septum (SEP), inferior vena cava (IVC or ICV) and crista terminalis (CT), Aorta (Ao), pulmonary vein (PV), pulmonary Artery (PA), coronary sinus (CS), right atrial appendage (RA), right ventricle (RV), endocardium (Endo), and epicardium (Epi) are also labelled.

1.1.4 The Cardiac Fibroblast

The heart contains about 70% non-myocytes and 30% myocytes. The cardiac fibroblast (CF), constituting 90-95% of the cardiac non-myocyte cell population, is

one of the most abundant non-myocyte cells in the heart [14], [18], [19]. The fibroblasts are widely distributed in cardiac tissue and act as the gap cells separating the cardiac myocytes. Fibroblasts have diverse morphologies in different locations of the tissue and during different metabolic activity. However, generally, fibroblasts are flat and spindle-shaped cells with multiple processes extending from the main cell [18], which normally contains an oval nucleus and has no basement membrane. Moreover, the cardiac fibroblasts are sensitive to the chemical and mechanical changes as well as the electrical signals in the cardiac tissue. Fibroblasts can form a 3D network (Figure 1.3B) by synthesising and expressing the extracellular matrix (ECM) as a response to those changes to ensure the proper function of the heart.

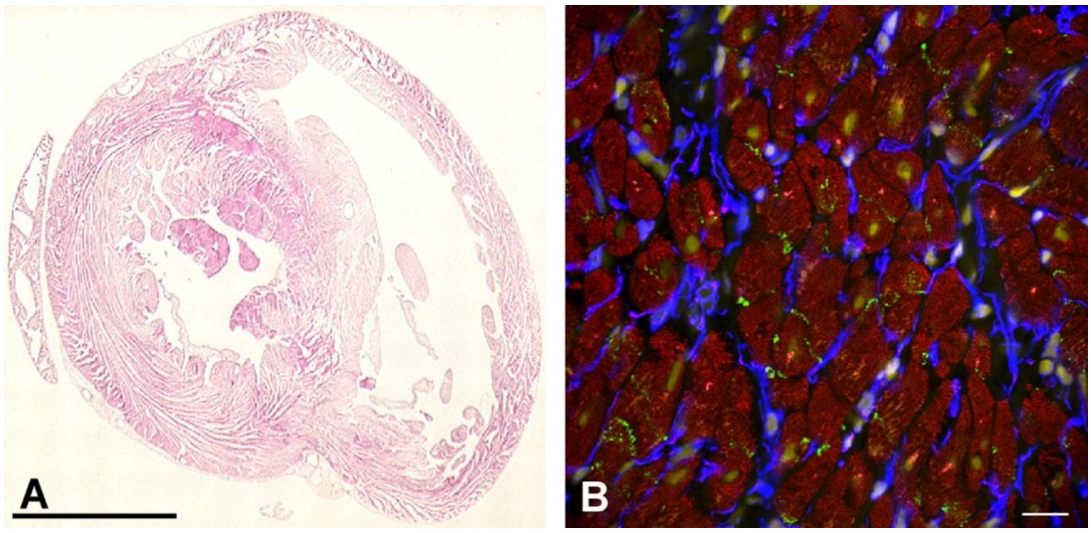

Figure 1.3 Cardiac tissue structure overview. (A) Histological diagram (transversal cross-section) of rabbit ventricular myocardium; cardiac muscle cells are labelled pink, non-myocytes are un-labelled. (B) The network of fibroblasts that surrounds myocyte clusters of 2–4 cells. Myocytes are labelled red and fibroblasts are labelled blue. The bright green dots represent the Cx43 and pale yellow-green patches represent the nucleus. Scale bars of 5 mm in A and 20 μm in B.

1.2 Cardiac Electrophysiology

1.2.1 Cell Membrane

The cell membrane is a thin phospholipid bilayer containing a hydrophilic head facing outward and a hydrophobic tail facing inward (Figure 1.4), separating the intracellular cytosol from the extracellular environment. The bilayer is impermeable to polar solutes, including nucleic acids, proteins, and ions, but permits the passive diffusion of the

hydrophobic molecules. Ions can only be transported through the cell membrane via some specialised integral protein structures, such as ion channels, ion exchangers, and ionic pumps.

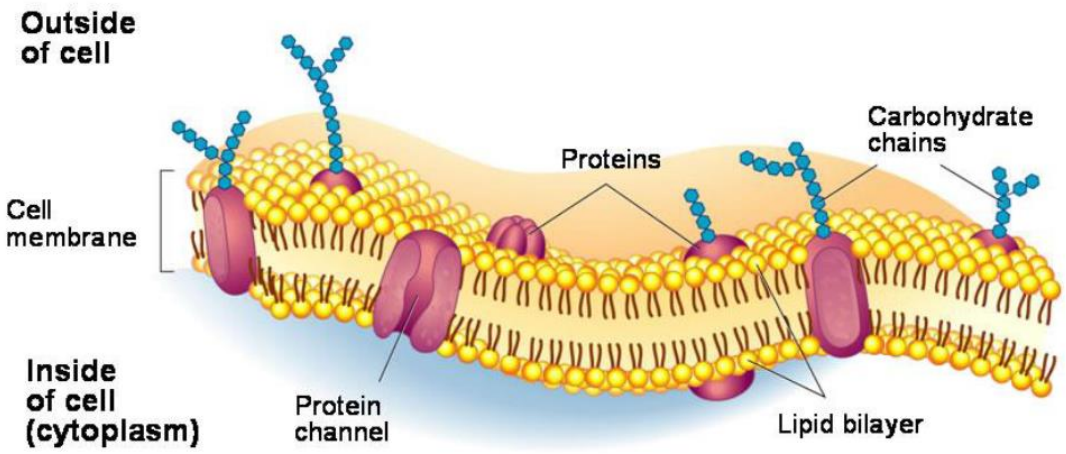

Figure 1.4 Schematic diagram of the physical structure of the cell membrane. The yellow polar head groups separate the brown hydrophobic tails from the aqueous cytosolic and the extracellular environment. The embedded protein channels are also shown.

1.2.2 Ion Channels, Exchangers, and Pumps

Ion channels are macromolecular pores in the sarcolemma (see Figure 1.3) that allow the ions to move through the cell membrane according to the electrochemical gradient formed by the different ion concentrations in the two sides of the cell membrane [20]. Normally, the ions move from a high to a low concentration. Ion channels are the most abundant structure that ions can pass through and have selective permeability for ions. Generally, each type of channel is only permeable for one specific type of ion, and it has two distinct processes, activation and inactivation, referred to as gates [20]. Whether or not a current can pass through the ion channel depends on the state of the gates.

As shown in Figure 1.5, extracellular ions tend to flow into a cell because of the electrochemical gradient towards the intracellular space. Ions can flow into the cell in state B (Figure 1.5 B). However, for states C and D, as the inactivation gates are inactivated, the currents cannot flow through the ion channel even though the activation gate in state C is open.

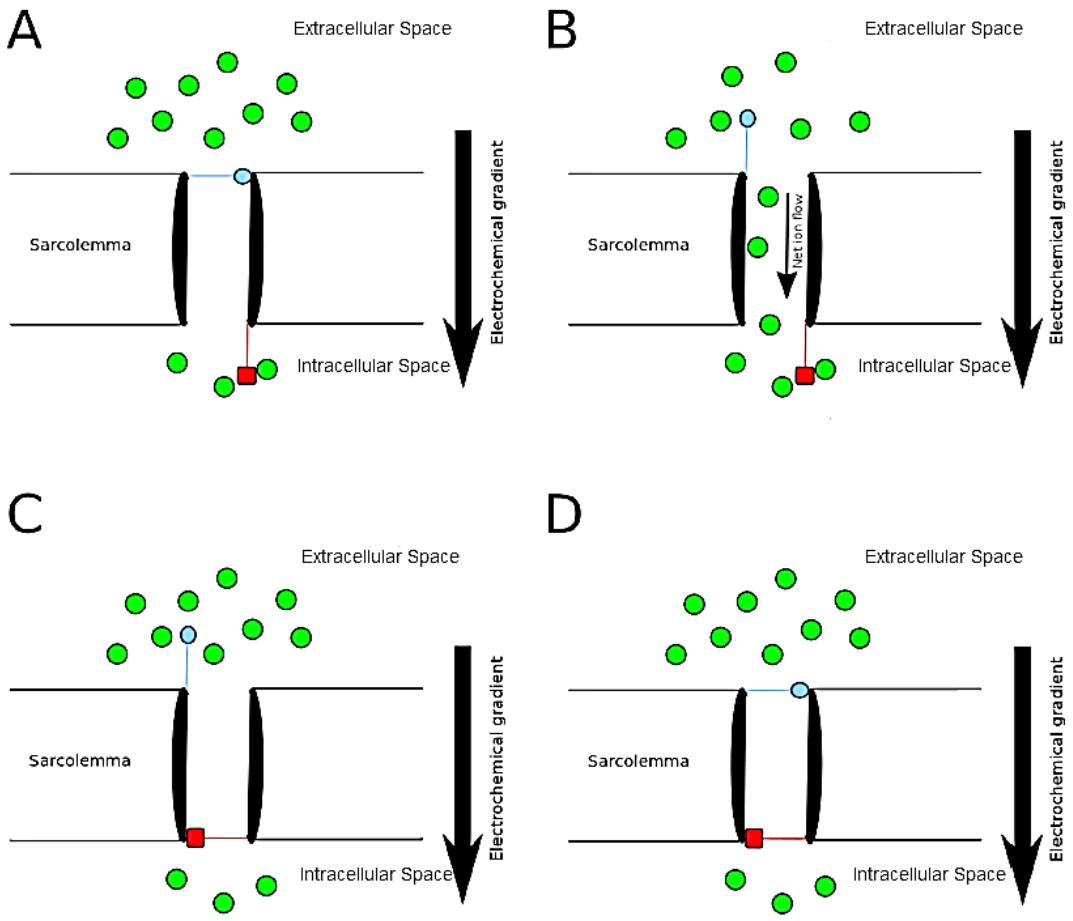

Figure 1.5 Schematic diagram of an ion channel. The activation gate (blue) and inactivation (red) gates in four different states are shown: (A) closed (deactivation), (B) open, (C) closed (inactivation), (D) closed (deactivation and inactivation). Figure adapted from [21].

Similar to the ion channels, ion pumps also have selectivity in ion transportation, they are permeable for one or two types of ions. Moreover, ion pumps can transport ions against the electrochemical gradient by metabolising energy. For example, through the Na^+/K^+ pump, two K^+ are actively transported into the cell regardless the higher intracellular concentration; meanwhile, the three Na^+ are moving out the cell despite the fact that the electrochemical gradient is inward. The ion exchangers can exchange ions in opposite directions. The directions depend on the concentrations of the ion on both sides of the cell membrane. The Na^+/Ca^{2+} exchanger can exchange a single Ca^{2+} with three Na^+ driven by the electrochemical gradient of Na^+.

1.2.3 Action Potential

The cardiac action potential (AP) is the change in the membrane potential (rise and fall) during a short period after an electrical stimulus is applied. The AP arises from the transportation of ions through the membrane following the stimulus.

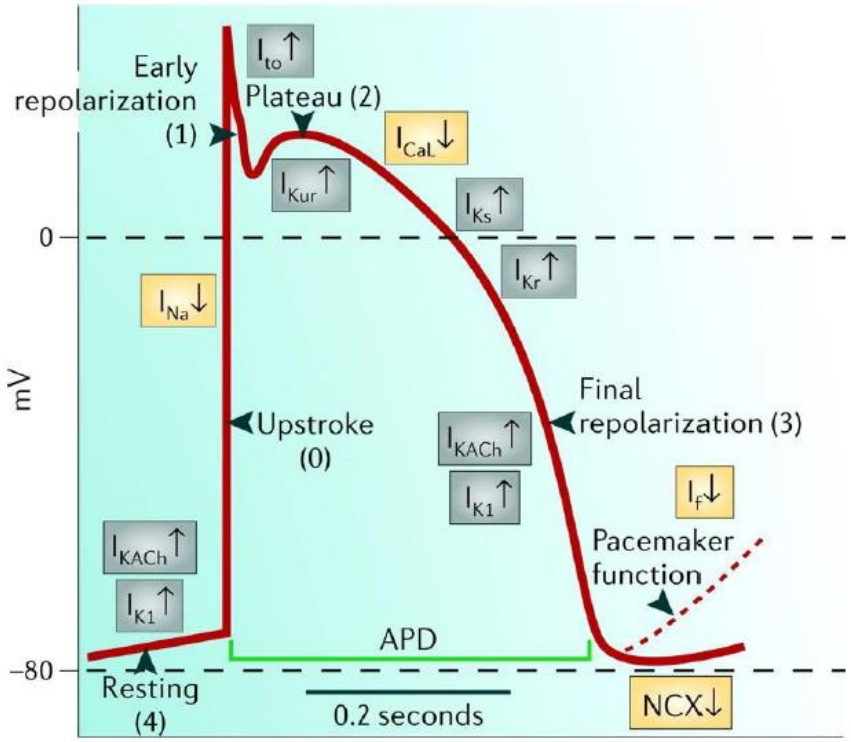

Figure 1.6 Schematic diagram of an example of cardiac action potential as a function of time. Five phases are presented: resting (phase 4), upstroke (phase 0), early repolarisation (phase 1), plateau (phase 2), and final repolarisation (phase 3). The inward currents (I_{Na}, I_{Ca}, I_f, and Na^+-Ca^{2+} exchanger (NCX)) are marked by ↓ in yellow boxes. The outward currents (I_{KACh}, I_{K1}, I_{to}, I_{Kur}, I_{Kr}, and I_{Ks}) are marked by ↑ in grey boxes. The figure is from [22].

Figure 1.6 shows the morphology of a typical AP (phases 0 to 4) with related ionic currents labelled. Phase 0 is the depolarisation phase, also called the upstroke of the AP, during which, the fast Na^+ channel is activated; then the Na^+ current (I_{Na}) flows into the cell in a short time. Therefore, the membrane potential becomes more positive and cells are depolarised. Phase 1 is the early repolarisation, during which the Na^+ channel is inactivated and the K^+ channels is activated, the outward transient K^+ current becomes the major current, as a result, the membrane potential becomes less negative. Phase 2 is the plateau of the AP resulting from the short-term balance of

influx and efflux currents (mainly the L-type Ca^{2+} current, rectifier K^+ currents, NCX, and Na^+-K^+ pump currents). In phase 3, because of the closing of L-type Ca^{2+} channels and the opening of K^+ channels, the delayed K^+ current and inward rectifier K^+ current become the dominant currents. A dramatic decrease in the membrane potential can be observed in this phase; the cells become more repolarised. Phase 4 is the resting phase. The delayed rectifier K^+ channels are inactivated, and the membrane potential returns to its resting value.

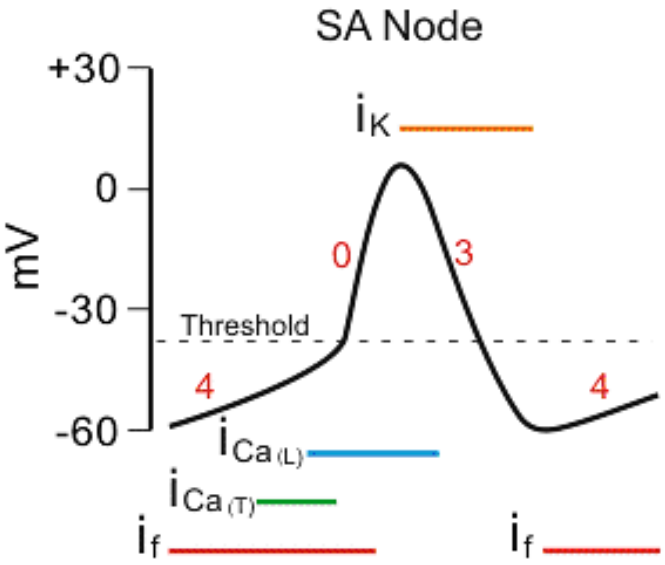

Figure 1.7 Schematic diagram of an example of cardiac action potential as a function of time in the SAN cell. The major ionic currents are labelled during the three phases: phase 0 (upstroke), phase 3 (rapid repolarisation), and phase 4 (diastolic depolarisation) [23].

Figure 1.7 shows the AP in the SAN with the main ionic currents labelled. As the primary pacemaker cells in the heart, the SAN cells show different AP characteristics from the AP of non-pacemaker cells in the heart. It normally has no true resting potential but is able to generate regular spontaneous APs. In phase 4, the slow Ca^{2+} currents (I_{CaT} and I_{CaL}) are the major depolarising currents versus the fast Na^+ currents in non-pacemaker cells. The AP is then triggered when the membrane potential reaches the threshold value (-40 and -30 mV). When it enters phase 3, the K^+ currents are activated, the AP begins to repolarize and finally reaches a maximum diastolic potential of -60 mV.

1.2.4 The Cardiac Conduction System

The adjacent myocytes in the myocardial tissue are normally connected with gap junctions, which are made of proteins as connexins. The ions can transfer between the myocytes freely through the abundant ion channels in the gap junctions, therefore, the APs can be propagated between myocytes via gap junctions (An initial electrical stimulus is needed for the non-pacemaker myocyte to trigger the AP).

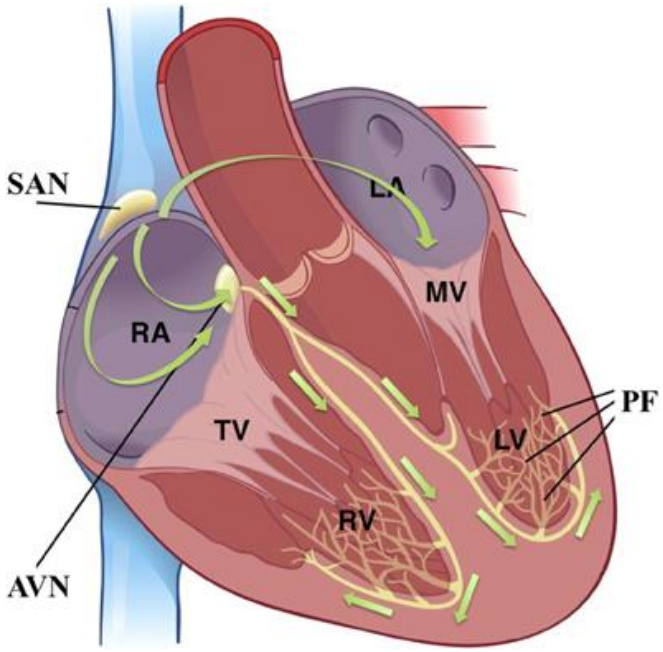

Figure 1.8 Schematic diagram of the cardiac conduction system. Green arrows indicate the cardiac activation sequence during sinus rhythm. The SAN (sinoatrial node), AVN (atrioventricular node), PF (Purkinje fibre), RA (right atrium), LA (left atrium), RV (right ventricle), LV (left ventricle), TV (tricuspid valve), and MV (mitral valve) are shown. [CC-BY-3.0 (www.creativecommons.org/licenses/by/3.0)], via Wikimedia Commons. Image by Madhero88.

The SAN located at the top of the right atrium (Figure 1.8) is the natural pacemaker of the heart. It can spontaneously depolarise and initiate APs. The Bachmann's bundle propagates the APs from the RA to the LA. Because of its high conduction efficiency, the RA and LA can contract at the same rhythm. The atrioventricular node is the secondary pacemaker in the heart, located in the inferior part of the inter-atrial septum. It can electrically connect the atrium with ventricle and pass the APs to the

atrioventricular bundle, where AP can be further propagated to the Purkinje fibres and then to the ventricular septum in the left and right ventricles.

1.3 Myocyte–Fibroblast Interaction

Individual cardiac fibroblasts have sheet-like structures. They are capable of spreading and interspersing between myocytes around the myocardium by going through extended 'spindle-like' processes [24]. The connections with myocytes and other fibroblasts are bridged by connexin junctions. In situ experiments have reported that fibroblasts have a very large membrane surface area, roughly 720 μm^2 in rabbit SAN (membrane folds and cell extensions are not taken into account) [6]. There are high possibilities that the cardiac fibroblast can interact and communicate with the cardiac myocytes or other fibroblasts in different ways because of the large membrane surface area.

1.3.1 Myocyte–Fibroblast Coupling

Traditionally, fibroblasts have been thought simply to be non-excitable cells that structurally support adjacent myocytes by expressing ECM (such as collagen and elastin fibres) and have no electrical communication with cardiac myocytes [19]. However, more recent research both *in vitro* [25]–[31] and *in vivo* [32]–[34] has demonstrated that cardiac fibroblasts can electrically couple to neighbouring myocytes and fibroblasts by forming gap junctions. According to the morphology of fibroblast and myocyte distribution found by immunohistochemically labelling and confocal microscopy technology, three dominant configurations of myocyte–fibroblast electrical interactions have been reported by Kohl et al. As shown in Figure 1.9 [35], they are the zero-sided, single-sided, and double-sided connection. In the zero-sided connection, the fibroblast acts as an obstacle decoupling myocyte pairs. In the single-sided connection, the fibroblasts are electrically connected to a single myocyte via gap junctions. In the double-sided connection, the fibroblast serves as a conductor interconnecting the separate myocytes or fibroblasts.

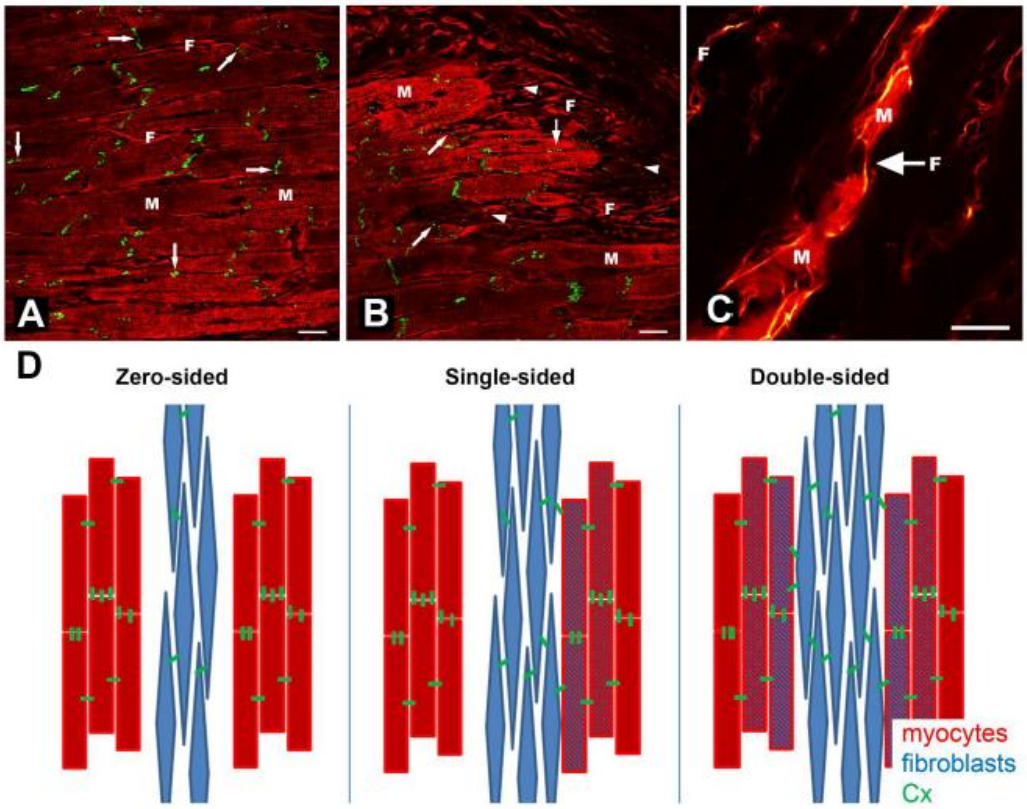

Figure 1.9 Myocyte-fibroblast connections in the cardiac tissue. A) Cx43 distribution at myocyte-myocyte junctions and occasional myocyte–fibroblast junctions in normal sheep myocardium. B) Cx43 distribution at F–M junctions in normal sheep myocardium. C) Confocal image of dyed myocyte–fibroblast–myocyte coupling in rabbit right atrial tissue. D) Conceptual myocyte–fibroblast connections by Cx proteins. Scale bars = 20 μm.

1.3.2 The Significance of Myocyte–Fibroblast Coupling

It has been reported that electrical couplings between fibroblasts and myocytes play important roles in maintaining the proper AP initiation and conduction. Cardiac fibroblasts have been found to have a high density in pacemaker tissue. It takes up about 50% -75% of the cell population in rabbit SAN, much more abundant than in ventricles[25], [35]. Fibroblasts in the SAN are thought to be able to electrically connect the separate pacemaker cells and therefore allow synchronic spontaneous activity in leading the pacemaker and ensure that the sinus impulse is propagated to the surrounding atrial cells properly [24]. In the atrium and ventricle, the fibroblasts can modulate the AP propagation by coupling in different ways to maintain the synchronisation of the electrical conductivity [6], [36], [37]. The positive effects of

injected fibroblasts on AP conduction in infarcted myocardium reported by *in vitro* experiments suggest that myocyte–fibroblast couplings can improve the AP conduction in injured cardiac tissue [30], [38], [39]. However, in order to better understand the therapeutic effect on heart injury, the mechanism underlying the myocyte–fibroblast electrical coupling in different species still needs to be explored in detail.

1.4 Overview and Aim of the Thesis

There are two main purposes of this thesis:

1. Give insight into the electrophysiological role of fibroblasts in fibroblast–myocyte coupling.
2. Explore the effects of coupling fibroblast number and coupling strength on electrical activities in pacemaker and atrial cells.
3. Discuss the coupling effects on AP initiation and propagation in cardiac tissue.

The background knowledge of cardiac physiology and electrophysiology is introduced in Chapter 1. The numerical methods and the mathematical formula of cell and tissue models are provided in Chapter 2. The development of cellular models of myocyte–fibroblast coupling in the SAN and atrium is introduced in Chapter 3. The simulation effects of coupling fibroblast number and coupling strength on the electrical activities in myocytes are also presented. The simulation results of the coupling effects on AP initiation and propagation in tissue models are illustrated in Chapter 4. Finally, In Chapter 5, the simulation results in cellular and tissue models are discussed. The conclusions, limitations, and future work are also presented.

Chapter 2. Mathematical and Physical Basis

2.1 Membrane Current and Potential

2.1.1 Hodgkin-Huxley Equations

To describe the relationship between current and voltage in the membrane of giant squid axons, Alan Lloyd Hodgkin and Andrew Huxley developed the Hodgkin-Huxley model in 1952 [40]. It incorporated three ionic currents (Na^+, K^+, and a 'leak current') and is the basis of most mathematical models to describe excitable cells. As shown in Figure 2.1, the cell is analogous to a simplified circuit, in which the capacitor represents the bi-layer cell membrane (Figure 1.4) and the resistances represent the ion channels.

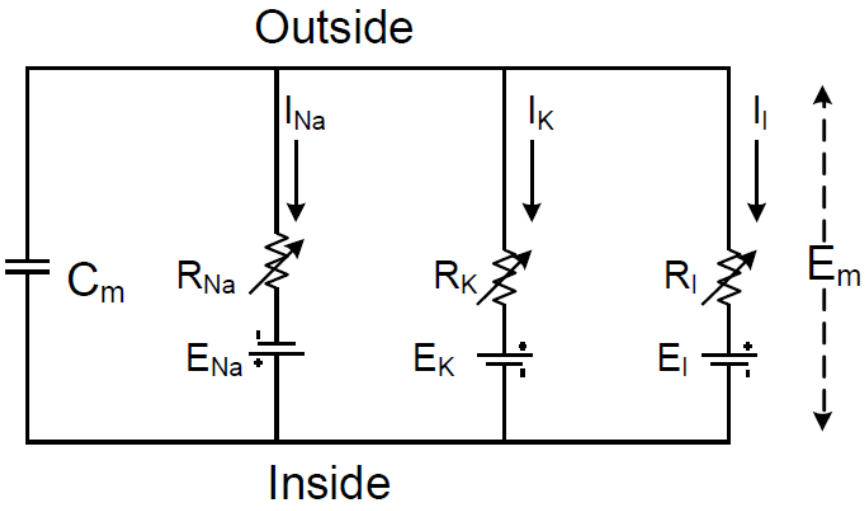

Figure 2.1 Schematic diagram of the electric circuit model of the membrane. C_m represents the membrane capacitance. I_{Na}, I_K, and I_l indicate the corresponding inward Na^+ current, outward K^+ current, and 'leak current', respectively. R_{Na}, R_K, and R_l represent the membrane resistance, while E_{Na}, E_K, and E_l represent the equilibrium potential. Figure adapted from [41].

The different ion concentrations on either side of the cell membrane result in a membrane potential difference across the membrane:

$$V = \phi_i - \phi_o , \tag{2.1}$$

where ϕ_i represents the intracellular potential and ϕ_o is the extracellular potential.

Therefore, in the capacitor,

$$V = \frac{Q}{C_m}, \tag{2.2}$$

where C_m is the capacitance, V is the potential difference across the capacitor, and Q is the change of the capacitor. Thus, the change rate of the membrane potential is governed by

$$\frac{dV}{dt} = \frac{1}{C_m}\frac{dQ}{dt}. \tag{2.3}$$

Therefore,

$$C_m \frac{dV}{dt} = I_c, \tag{2.4}$$

where I_c is the capacitive current. The resistance and each ionic current across the membrane can be expressed by

$$I_i = g_i(E - E_i), \tag{2.5}$$

where i represents the particular ion, I_i is the ionic current, $g_i = 1/R_i$ is the conductance of the channel, E is the membrane potential, and E_i is the equilibrium potential.

According to the Nernst equations [42], the equilibrium potential for each ion is

$$E_i = \frac{RT}{zF}\ln(\frac{[i]_o}{[i]_i}), \tag{2.6}$$

where R is the universal gas constant, R is the temperature, z is the valance of the ion, F is Faraday's constant, $[i]_o$ is the extracellular concentration, and $[i]_i$ is the intracellular concentration. According to the Kirchhoff's first law, the algebraic sum of currents in a network of conductors meeting at a point is zero; thus, combining Equation 2.4 and Equation 2.5 yields

$$I_c + \sum I_i = 0, \tag{2.7}$$

thus,

$$C_m \frac{dV}{dt} = -\sum I_i \,. \tag{2.8}$$

As three ionic currents (the inward Na^+ current, outward K^+ current. and 'leak current) were considered in the HH model,

$$-\sum I_i = -g_{Na}(V_{Na} - E_{Na}) + g_K(V_K - E_K) + g_L(V_L - E_L)\,. \tag{2.9}$$

2.2 Action Potential Propagation

The AP propagation in cardiac tissue depends on the gap junction channels, which bridge the cells and allow ions to flow between the neighbouring cells. Thus, the cells can share similar electrophysiological features because of the ionic communication. For example, the concentration of intracellular Na^+ and the membrane potential is increased during the upstroke in the excited cell; as a result, more Na^+ flows to the neighbouring cells via gap junction channels and elevates their membrane potentials. When the membrane potentials in the neighbouring cells are increased to their thresholds, their APs will be triggered.

2.2.1 Monodomain Model

The monodomain model was used in this thesis to describe the AP propagation in cardiac tissue. The cardiac tissue is assumed to be isotropic in the monodomain model to reduce the complexity of computation. Both the intracellular and extracellular potential fields are assumed to have the same anisotropy ratio [43]. Thus, the AP propagation can be described by

$$\frac{\partial V}{\partial t} = \nabla \cdot \mathbf{D}(\nabla V) - \frac{I_{ion}}{C_m}\,, \tag{2.10}$$

where I_{ion} is the total transmembrane ionic current, representing $\sum I_i$ in Equation 2.8, C_m is the membrane capacitance, ∇ is the spatial gradient operator, V is the membrane potential, and $\mathbf{D}$ is a tensor of diffusion coefficient that depends on the coupling conductance [44]. In most of the simulations, the coupling conductance is constant; thus, Equation 2.10 can be written as

$$\frac{\partial V}{\partial t} = D\nabla^2 V - \frac{I_{ion}}{C_m}, \tag{2.11}$$

where D is the diffusion coefficient.

2.2.2 Boundary Conditions

The "no-flux" boundary [45] conditions were applied in our study. It is assumed that there is no current flow normal to the boundaries in an isolated tissue, which means that the gradient of the voltage in the direction is zero:

$$\mathbf{n} \cdot \mathbf{D}\nabla V = 0, \tag{2.12}$$

where **n** is the unit vector normal to the tissue surface. The direction of **n** varies in real tissue; therefore, an approximation is needed when identifying the normal on the tissue surface.

In our 2D real tissue simulation (Chapter 4), the 2D slice were discretized into structured grids and each grid represents a tissue cell. A layer of "ghost cell" was added on the boundary [46]. In order to make the gradient of the voltage for each cell in boundary (∇V) equal to zero, the voltage of the "ghost cell" is set to be same as the voltage of the adjacent boundary cell, therefore, the "no-flux" boundary condition in real tissue can be ensured.

2.3 Numerical Methods

2.3.1 The Forward Euler Method

The forward Euler method was first proposed by Leonhard Euler and is the simplest method for solving an ordinary differential equation (ODE) with a given initial value. The differential equation can be expressed as follows:

$$\frac{dy}{dx} = f(x, y(\mathrm{x})) \cdot \tag{2.13}$$

Given an initial value x_0, and a increment, Δx (from x_n to x_{n+1}), according to Taylor's expansion, we can obtain

$$y_{n+1} = y_n + \Delta x \cdot f(x_n, y(\mathrm{x}_n)) + \mathrm{O}(\Delta x^2), \tag{2.14}$$

where $\mathrm{O}(\Delta x^2)$ is the local error, which can be reduced with a forward step that is small

enough.

2.3.2 The Finite Difference Method

The finite difference method (FDM) is a common numerical method to approximate the solution of a partial differential equation (PDE) by discretizing the space domains into structured grids. In a 1D monodomain, the approximation of the second space derivative at position x can be obtained by using the second-order central difference:

$$f^{''}(x) = \frac{f(x+\Delta x) + f(x-\Delta x) - 2f(x)}{\Delta x^2}, \tag{2.15}$$

where Δx is the spacing step in the grid. Using the forward time difference (Δt) and applying Equation 2.14 to the monodomain model (Equation 2.10), the membrane potential at time t and position x is governed by

$$V_x^t = V_x^{t-\Delta t} + \Delta t \frac{D(V_{x-\Delta x}^{t-\Delta t} + V_{x+\Delta x}^{t-\Delta t} - 2V_x^{t-\Delta t})}{(\Delta x)^2} - \Delta t \frac{I_{ion}}{C_m}, \tag{2.16}$$

where V is the function for the membrane potential, I_{ion} is the total transmembrane ionic current, D is the diffusion coefficient at x, Δt and Δx are the time and space step, respectively.

2.3.3 Stability Criterion

In order to solve the monodomain equation (2.16) in a stable domain, the following relationship must be satisfied[21], [46]:

$$\Delta t \leq \frac{\Delta x^2}{D} \ldots\ldots\ldots\ldots\ldots\ldots\ldots\ldots\ldots\ldots\ldots \text{(2.17)}$$

where Δt and Δx are the time and space step, respectively. D is the diffusion coefficient.

2.4 Characterizing Action Potentials in Excitable Cells

As shown in Figure 2.2, both the pacemaker cells and the non-pacemaker cells show an upstroke during the depolarisation. The maximum upstroke velocity (dV/dt_{max}) is the maximum rate of the membrane potential change during depolarisation. The time corresponding to the maximum upstroke velocity is defined as the activation point. The time from activation point to the 90% of repolarisation is defined as APD_{90}. The

peak amplitude (PA) is the most depolarised potential. The resting membrane potential (RMP) is the potential of the non-pacemaker cells during the flat resting phase. The maximum diastolic potential (MDP) refers to the most negative diastolic potential in the pacemaker cells. The cycle length (CL) in pacemaker cells is the interval between the MDPs.

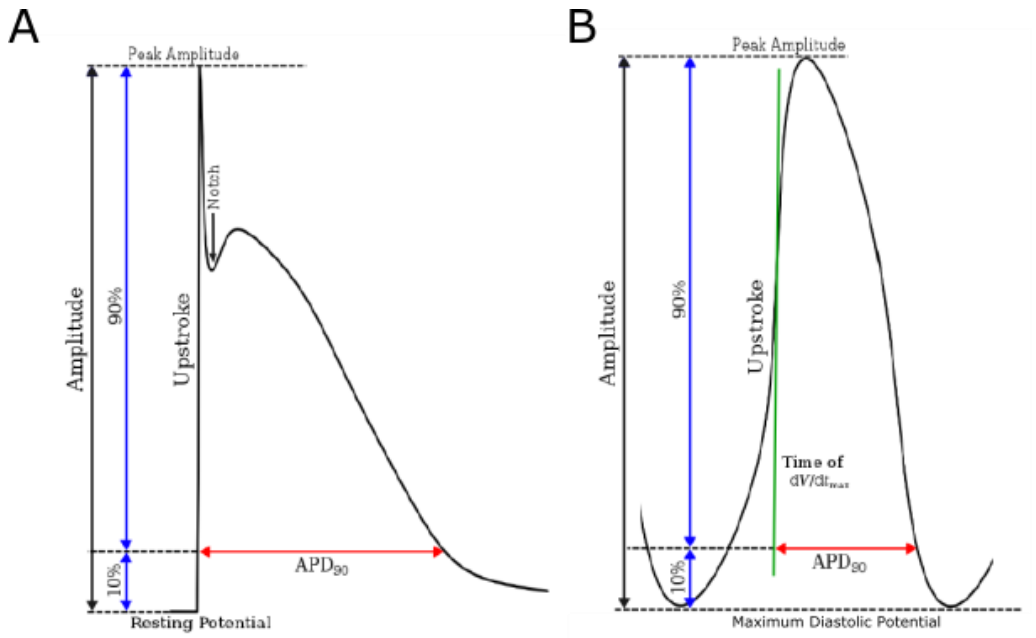

Figure 2.2 Distinguishing features of the action potential in (A) non-pacemaking and (B) pacemaking cell. The amplitude, peak amplitude, resting potential, maximum diastolic potential upstroke, notch, and APD_{90} are labelled. Figure adapted from [46].

Chapter 3. The Myocyte-Fibroblast Coupling in Cellular Models

3.2 Introduction

Originating from mesenchymal stem cells, fibroblasts constitute 90-95% of the cardiac non-myocyte cell population. The interaction between cardiac myocytes and fibroblasts plays a vital role in cardiac fibrosis and arrhythmia related heart disease. Pathological fibrosis and myocardial remodelling caused by injury, ageing, inflammation, infarction, hypertrophy, and ischemia are closely associated with increasing fibroblast density and ECM accumulation in the heart [31], [47], [48]. It is particularly important to understand the mechanism underlying the myocyte–fibroblast interaction physiologically and pathologically.

In vitro experiments have directly demonstrated the existence of electrical coupling between cardiac myocytes and fibroblasts. The effects of fibroblasts on the electrical activities in cardiac cells and tissues have been widely studied. Miragoli et al. [27] studied impulse conduction in a cultured neonatal-rat myocyte strand with coated fibroblasts and found that the conduction velocity (CV) of voltage impulse in the myocyte strand was slowed down and the maximum upstroke velocity (dV/dt_{max}) of myocytes was decreased after coating more fibroblasts. McSpadden et al. also reported that the CV in the cultured monolayer of neonatal-rat cardiac myocytes was decreased along with the increasing density of fibroblasts [49]. Gaudesius et al. illustrated that an electrical impulse was propagated between myocytes interconnected with a strand fibroblast of a length of up to 300μm in their co-cultured experiment. A larger conduction delay was shown after increasing the length of the interconnecting fibroblast strand [26], [27].

Some computational models also have been developed *in silico* to investigate the more detailed mechanism underlying the electrical interactions between myocytes and fibroblasts. Kohl and Noble [50] developed a cellular model of a SAN myocyte with a single fibroblast coupled and found that the myocyte–fibroblast coupling could increase the pacemaking rate. By integrating Tusscher-Noble-Noble-Panfilov's human ventricular myocyte model with an active fibroblast model, MacCannell et al. found that fibroblast–myocyte coupling could result in a more hyperpolarised action

potential plateau, a shortened action potential duration (APD), and a more positive resting membrane potential (RMP) in coupled myocyte [51]. Malecker et al. [52] simulated the coupling effects on the excitability and repolarisation of myocytes by coupling two different types of fibroblast models to a human atrial myocyte. Their results demonstrated that the changes in the waveform of myocytes are highly dependent on the coupling strength, electrophysiology of the fibroblast, and coupling frequencies.

Studies of coupling mechanism in cellular models have been conducted since the 1990s. According to the most recent research, cardiac fibroblasts are a capacitor that is charged during depolarisation phase of coupled myocyte and discharged during repolarisation phase. However, most of the conclusions come from computer simulations in non-pacemaker cells. Whether there are different coupling mechanisms in pacemaker because of their unique electrophysiological properties is still unknown. Therefore, in this thesis, we developed cellular models of fibroblasts coupling with SAN centre, periphery, and atrial cells to explore the mechanisms underlying coupling in detail. The effects of coupling fibroblast number and coupling strength were also studied.

3.2 Method

3.2.1 Myocyte–Fibroblast Coupling

To study the myocyte–fibroblast coupling effects on the SAN and atrial myocytes, we used the cell-to-cell coupling model introduced by MacCannell [51]. As shown in Figure 3.1, a selected number of fibroblasts were assigned to couple with a single myocyte via gap junctions. The membrane potential of the myocyte is governed by the following differential equation:

$$\frac{dV_m}{dt} = -\frac{1}{C_m}\left[I_m\left(V_m, t\right) + I_{stim} + \sum_{i=0}^{n} G_{gap}\left(V_m - V_f\right) \right], \tag{3.1}$$

where V_m and V_f represent the membrane potential of myocytes and fibroblasts, respectively. C_m is the membrane capacitance of the myocyte, I_m is the sum of ionic currents of the myocyte, and I_{stim} represents the stimulus current applied to atrial myocytes, which is set to 0 in the SAN cells. G_{gap} is the gap junction conductance, and

i=0 represents no fibroblast is coupled to the myocyte, n represents the number of fibroblasts coupling.

Similarly, the membrane potential of fibroblast is regulated by the following differential equation:

$$\frac{dV_f}{dt} = -\frac{1}{C_f}\left[I_f\left(V_f, t\right) + G_{gap}(V_f - V_m)\right], \tag{3.2}$$

where C_f represents the membrane capacitance of the fibroblast and I_f is the transmembrane current of fibroblast.

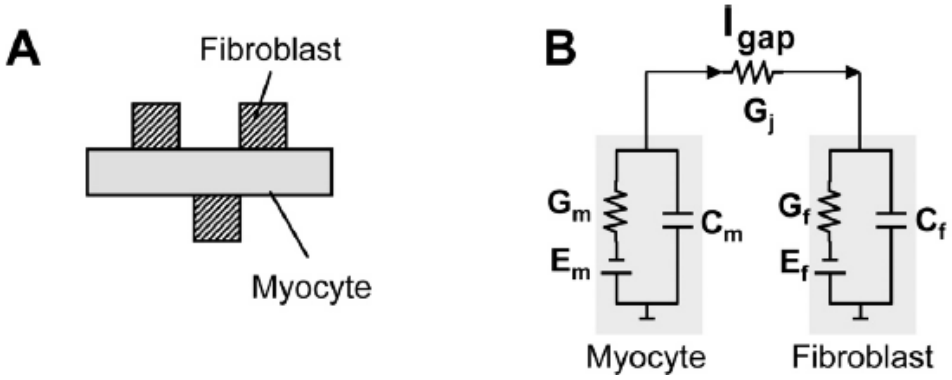

Figure 3.1 Schematic diagram of the myocyte-fibroblast coupling. (A) A single myocyte is coupled to a selected number of fibroblasts. (B) An electrical circuit of a myocyte-fibroblast coupling. Figure adapted from [53].

G_{gap} is a very important parameter in myocyte-fibroblast coupling representing the coupling strength. According to the co-cultured experiment on neonatal rat cardiac myocytes coupled with fibroblasts conducted by Rook et al., it varies from 0.31 nS to 8 nS [25]. In computational models, the G_{gap} value was set in a very wide range of 0.05 - 80 nS. In our study, G_{gap} was set in the range of 0 - 8 nS; when G_{gap} is 0 nS, there is no coupling between the fibroblast and myocyte. In addition, we consider it as a weak coupling when G_{gap} is less than 0.2 nS and a strong coupling when G_{gap} is larger than 1 nS.

A myocyte–fibroblast–myocyte model (M-nF-M, corresponding to the double-sided connection) was also developed to investigate the capability and the efficiency of the propagation of APs in a strand of fibroblasts. A G_{gap} of 0 - 30 nS was selected for myocyte–fibroblast coupling; the value of G_{gap} for fibroblast–fibroblast coupling was

assumed to be the same as it is in fibroblast–myocyte coupling. Therefore, the transmembrane potential for the myocyte is shown in the following differential equation:

$$\frac{dV_m}{dt} = -\frac{1}{C_m}\left[I_m\left(V_m, t\right) + I_{stim} + G_{gap}(V_m - V_{f,a}) \right], \tag{3.3}$$

where $V_{f,a}$ represents the membrane potential of the first or last fibroblast in the strand and I_{stim} is the stimulus applied (set to 0 for the last myocyte).

The membrane potential for the k^{th} fibroblast in the strand is governed by Equation 3.4:

$$\frac{dV_{f,k}}{dt} = -\frac{1}{C_f}\left[I_{f,k}\left(V_{f,k}, t\right) + G_{gap}(2V_{f,k} - V_{f,k-1} - V_{f,k+1}) \right], \tag{3.4}$$

where $V_{f,k}$ and $I_{f,k}$ are the membrane potential and total ionic current of the k^{th} fibroblast, respectively, while $V_{f,k-1}$ and $V_{f,k+1}$ are the membrane potentials of the previous and next fibroblast, respectively. For the first fibroblast in the strand, $V_{f,k-1}$ is replaced by V_m of the first myocyte, similarly for the last fibroblast, $V_{f,k+1}$ is replaced by V_m for the last myocyte.

3.2.2 Models of SAN

To explore the coupling effects of fibroblasts on central and peripheral SAN myocytes, we used Zhang's rabbit SAN model [44], [54]. As shown in Equation 3.5, the total ionic current ($I_{tot,SAN}$) in SAN incorporates a TTX-sensitive Na^+ current (I_{Na}), L-type Ca^{2+} current (I_{CaL}), T-type Ca^{2+} current (I_{CaT}), 4-AP-sensitive currents (I_{to} and I_{sus}), rapid delayed rectifying K^+ current (I_{Kr}), slow delayed rectifying K^+ current (I_{Ks}), hyperpolarisation-activated current (I_f), pump current (I_p), exchanger currents (I_{NaCa}), and background current (I_b including I_{bNa}, I_{bCa}, and I_{bK}). Cells were assumed to be larger in the SAN periphery with a membrane capacitance of 65 pF and relatively small in the SAN centre with a membrane capacitance of 20 pF.

$$I_{tot,SAN} = I_{Na} + I_{Ca,\mathrm{L}} + I_{Ca,\mathrm{T}} + I_{to} + I_{sus} + I_{K,r} + I_{K,s} + I_f + I_b + I_{NaCa} + I_p \quad \ldots\ldots\ldots\ldots\ldots\ldots (3.5)$$

3.2.3 Model of Atrial Myocyte

We used the cell model in rabbit right atrium developed by Lindblad [55] and modified by Aslanidi [56]. As shown in Equation 3.6, the total ionic current of the atrial myocyte ($I_{tot,atrium}$) incorporates the fast Na^+ current (I_{Na}), L-type Ca^{2+} current (I_{CaL}), T-type Ca^{2+} current (I_{CaT}), and transient and sustained outward currents (I_{to} and I_{sus}), fast, slow, and inward delayed rectifier K^+ currents (I_{Kr}, I_{Ks}, and I_{K1}), background currents (I_{bNa}, I_{bCa}), pump current (I_{NaK}), and exchanger current (I_{NaCa}). The membrane capacitance of the atrial cell model was set to 50 pF. The cycle length (CL) was set to 500 ms.

$$I_{tot,atrium} = I_{Na} + I_{Ca,\mathrm{L}} + I_{Ca,\mathrm{T}} + I_{to} + I_{sus} + I_{K,r} + I_{K,s} + I_{K1} + I_{b,Na} + I_{b,Ca} + I_{NaK} + I_{NaCa} \quad ..(3.6)$$

3.2.4 Model of Cardiac Fibroblast

We used the 'active' fibroblast model developed by MacCannell et al. [51], which incorporates four ionic currents; as shown in Equation 3.7, they are the time- and voltage-dependent fibroblast K^+ current (I_{Kv}), inward-rectifying K^+ current (I_{K1}), pump current (I_{NaK}), background Na^+ current (I_{bNa}). The membrane capacitance of fibroblast was set to 6.3 pF, according to the experimental data measured from an isolated cardiac fibroblast.

$$I_{tot,\mathrm{fibro}} = I_{Kv} + I_{K1} + I_{b,Na} + I_{NaK} \quad \ldots\ldots\ldots\ldots\ldots\ldots\ldots\ldots\ldots\ldots(3.7)$$

3.3 Results

3.3.1 Effects of Coupling Strength under Weak Coupling

To investigate the effect of coupling strength on the electrical activity in SAN and atrial myocytes under weak coupling (definition in section 3.2). A single fibroblast was coupled to the myocyte in the SAN centre (CSAN), SAN periphery (PSAN), and atrium (G_{gap} = 0 - 0.2 nS), respectively.

Generally, as shown in Figure 3.2G–I, when there is no coupling (G_{gap} = 0 nS) the membrane potential of the fibroblast remains at its resting potential level and there are no gap junction current flows between fibroblasts and myocytes. After a fibroblast is coupled to the myocyte, the I_{gap} changes along with time, which is negative during the early depolarisation and late repolarisation phase of the AP of coupled myocytes, suggesting an inward current flowing from the fibroblast to the coupled myocyte. The I_{gap} remains positive during the rest of the depolarisation and repolarisation phase,

indicating an outward current from the coupled myocyte to the corresponding fibroblast. Meanwhile, the membrane potential of the fibroblast mimics the AP in the coupled myocyte and forms an action potential-like shape but with a much lower peak amplitude (PA) (Figure 3.2D–F). The PA of the myocyte and the corresponding coupled fibroblast depends on the gap junction conductance (G_{gap}). After coupling with a larger G_{gap}, the PA of the coupled fibroblasts and the peak I_{gap} increased; the PA of the myocyte is reduced in the CSAN, but remains almost unchanged in the PSAN and atrium.

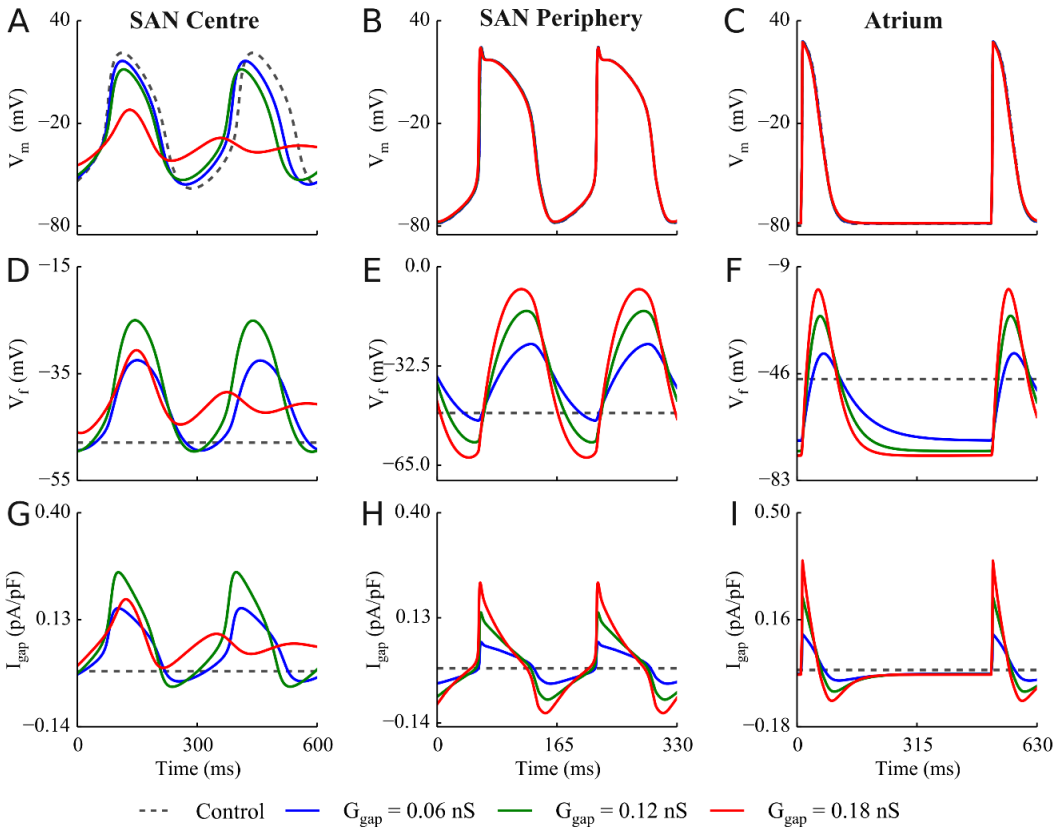

Figure 3.2 Effects of G_{gap} on electrical activities of the myocytes and coupled fibroblasts as a function of time. The membrane potential of the myocyte (A, B, and C) and the coupled fibroblast (D, E, and F) as well as the gap junction current (I_{gap}) (G, H, and I) in the CSAN, PSAN, and atrium after coupling with a single fibroblast with a G_{gap} of 0, 0.06 nS, 0.12 nS and 0.18 nS.

In the CSAN, the quantified changes in AP characteristics are shown in Figure 3.3. After coupling with a larger G_{gap}, the PA becomes less depolarised and the MDP becomes more positive; as a result, the myocyte APA shows marked reductions (reduced by 9% with a G_{gap} of 0.06 nS and 18.5% with a G_{gap} of 0.12 nS compared to

the control value). The spontaneous activity is abolished with a G_{gap} of 0.18nS (Figure 3.3A). Meanwhile, a decreased dV/dt_{max} (from 2.66 V/s to 1.35 V/s), a shortened CL (by 14%), and a shortened APD_{90} (by 13.5%) can also be observed in Figure 3.3B–D when G_{gap} is increased from 0nS to 0.18 nS, which indicates a slower upstroke and a faster pacemaking rate.

Figure 3.4A shows the total transmembrane current (I_{tot}) of the myocyte under control conditions and weak coupling. A reduction in the I_{tot} can be observed after coupling with a larger G_{gap}. For example, it is decreased by 7.9% with a G_{gap} of 0.06nS and 14.7 % with a G_{gap} of 0.12nS compared to the control value, and it finally vanishes when G_{gap} is increased to 0.18nS. When the G_{gap} is increased from 0 to 0.06nS and 0.12nS, the peak I_{CaL} decreases by 12.3% and 24.5%, and the peak I_{kr} is decreased by 10.6% and 19.4% (Figure 3.4C and B). Both currents vanish when G_{gap} is increased to 0.18 nS. The reductions in I_{to}, I_{CaT}, and I_f can also be observed in Figure 3.4D–F after G_{gap} is increased.

In the PSAN, as shown in Figure 3.5, the changes in AP characteristics of myocyte are relatively small as compared to the CSAN. When the G_{gap} is increased from 0 to 0.18 nS, the dV/dt_{max} declines by 4.6% from 67.6 V/s to 64.5 V/s (Figure 3.5B), which indicates a slower depolarisation rate. The APD_{90} is shortened and the CL is increased slightly after coupling with a larger G_{gap}. Moreover, after increasing G_{gap} to 0.18 nS, the changes in the PA and MDP are much smaller in comparison to the CSAN. The changes in the I_{tot} and each individual current are much smaller compared in the CSAN model (Figure 3.6A).

In the atrium (Figure 3.7), after the G_{gap} is increased from 0 to 0.18 nS, the dV/dt_{max} shows only a small decrease, the APD_{50} is shortened by 3.6% decreasing from 51.6 ms to 49.7 ms, the APD_{90} is shortened first and then increased to 86.1 ms versus 85.3 ms in control, the PA decreases slightly, and the RMP becomes less negative. The coupling effects on the transmembrane currents are shown in Figure 3.8. When the G_{gap} is increased from 0 to 0.18 nS, the I_{CaL}, I_{Na} and I_{to} do not show significant changes, in contrast, the I_{Kr} and I_{Ks} are weakened by 7.6% and 8.5%, respectively.

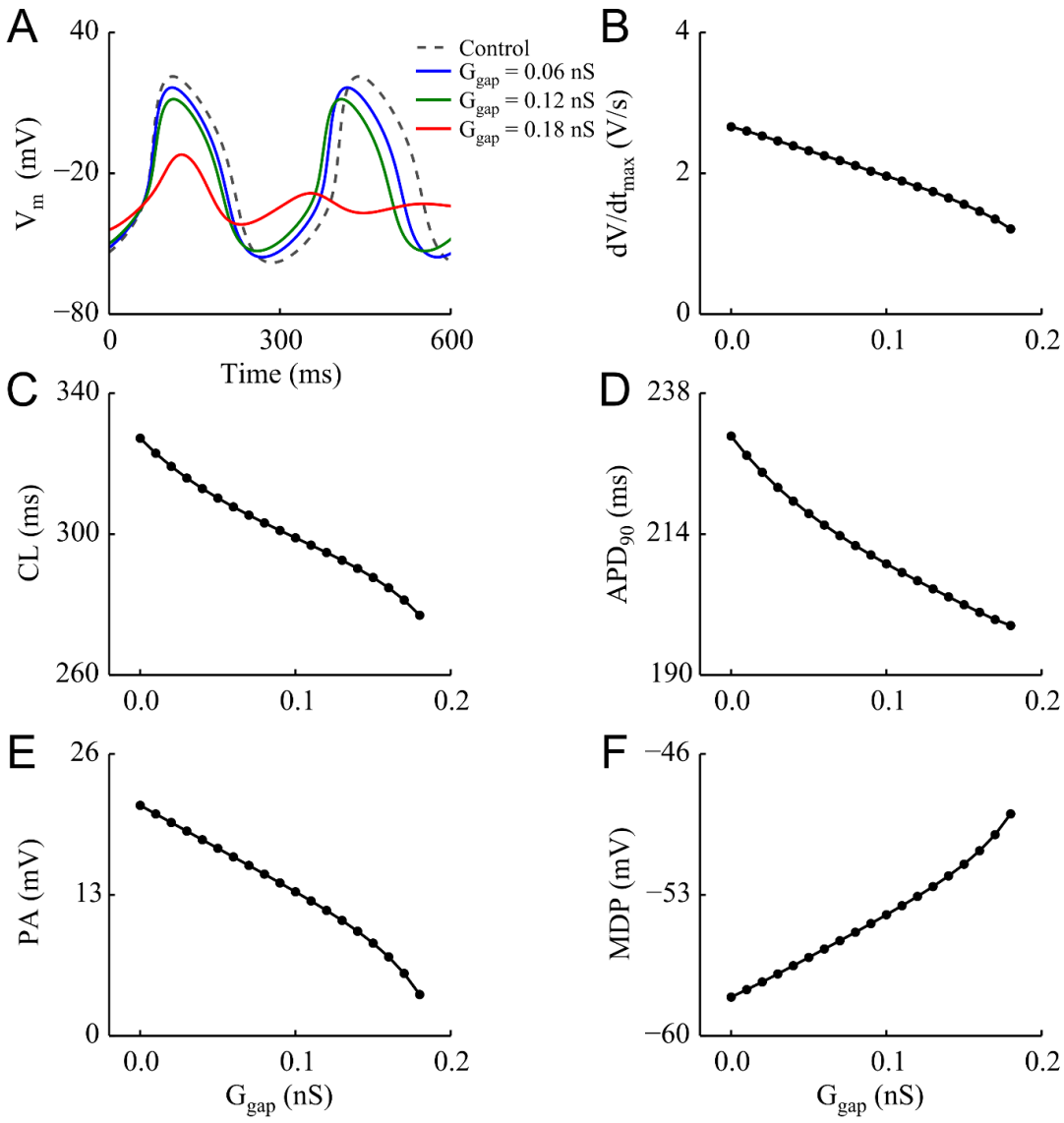

Figure 3.3 Effects of G_{gap} on the AP characteristics of myocytes in CSAN under weak coupling. Changes in the (A) AP, (B) dV/dt_{max}, (C) CL, (D) APD_{90}, (E) PA, and (F) MDP of the coupled myocytes.

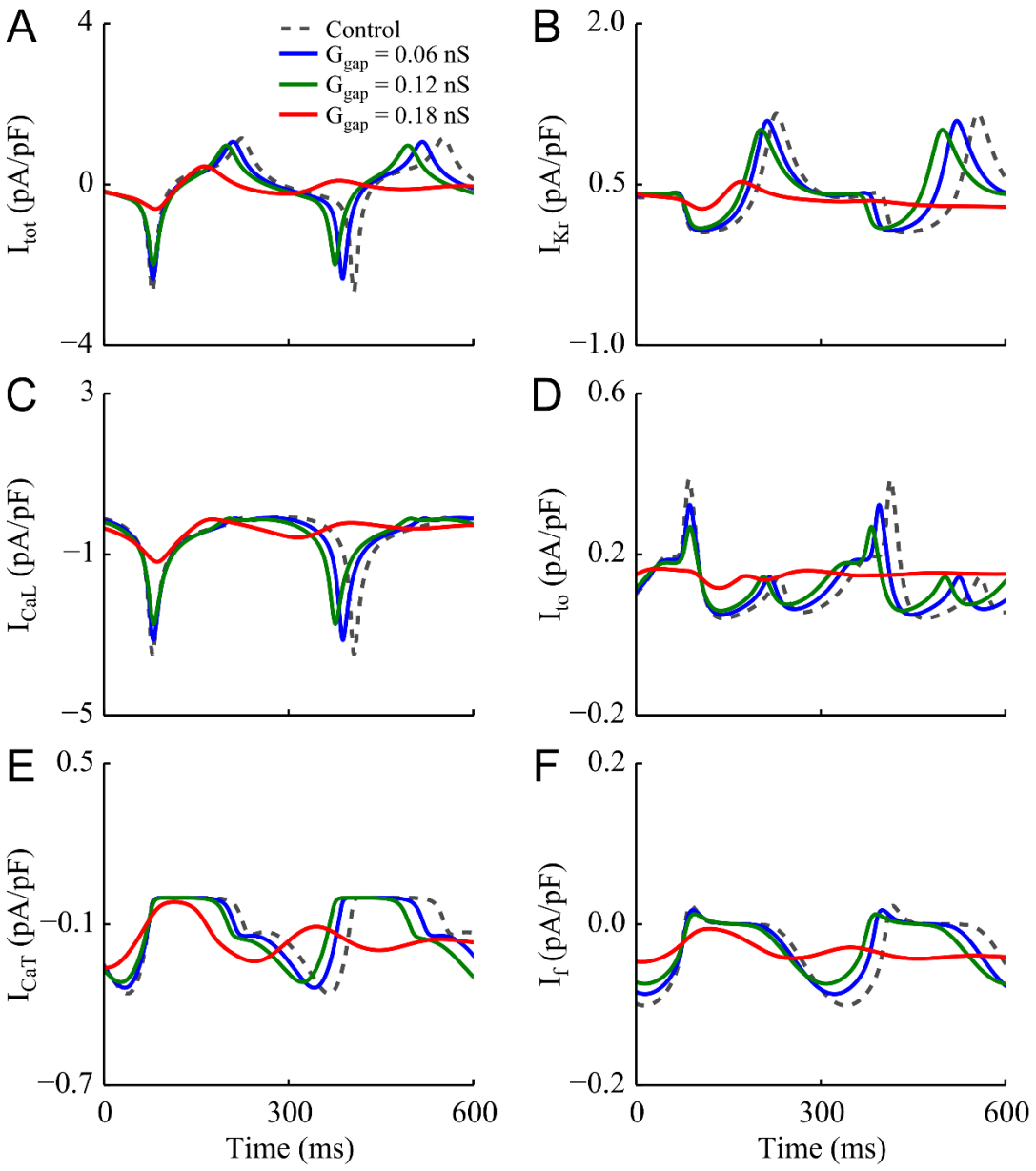

Figure 3.4 Effects of G_{gap} on the transmembrane currents of myocytes in the CSAN under weak coupling as a function of time. Changes in the (A) I_{tot}, (B) I_{Kr}, (C) I_{CaL}, (D) I_{to}, (E) I_{CaT}, and (F) I_f of myocytes after coupling with a single fibroblast with a G_{gap} of 0, 0.06 nS, 0.12 nS and 0.18 nS, respectively.

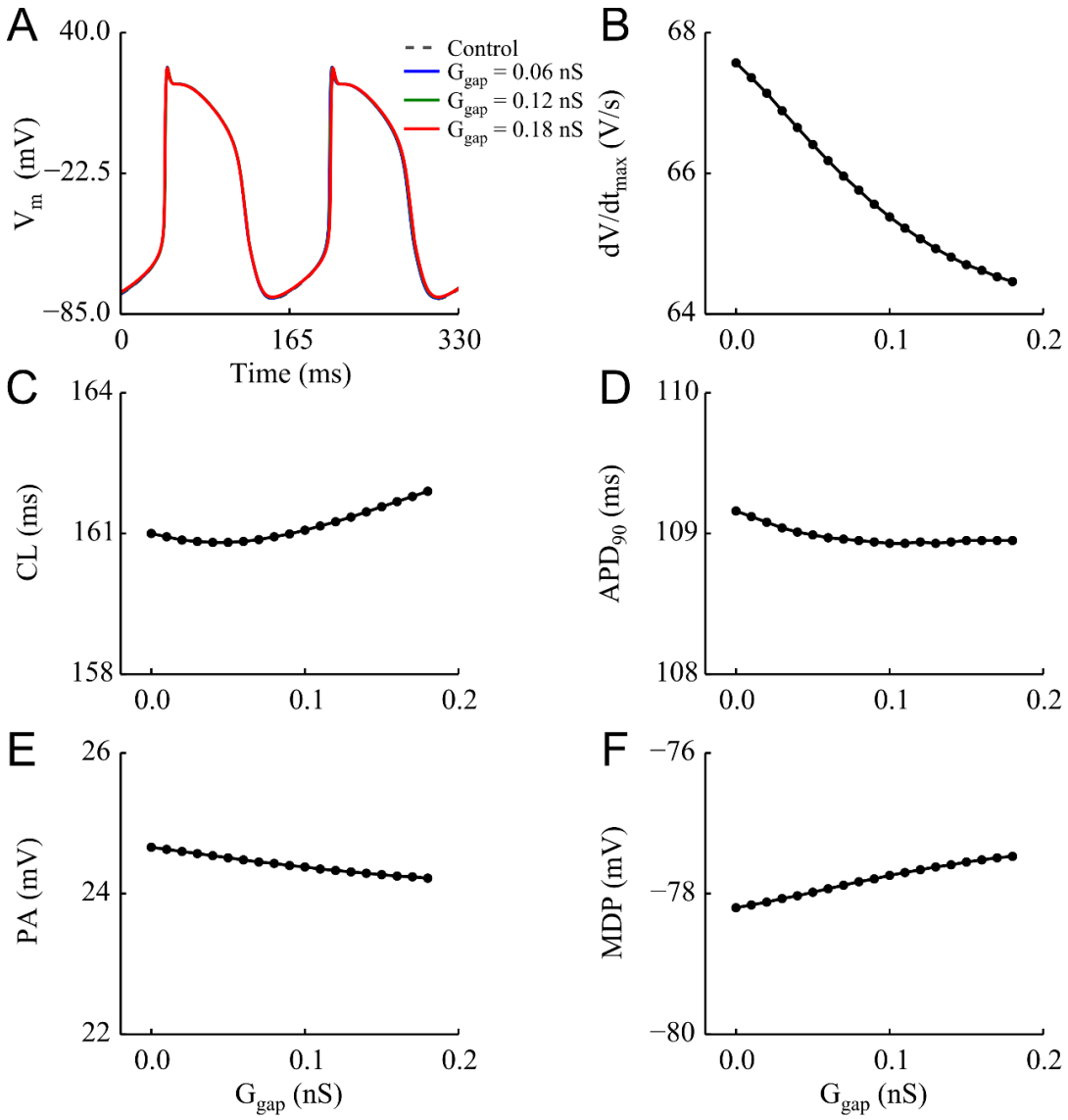

Figure 3.5 Effects of *G_{gap}* on the AP characteristics of myocytes in PSAN under weak coupling. Changes in the (A) AP, (B) dV/dt_{max}, (C) CL, (D) APD_{90}, (E) PA, and (F) MDP in the myocytes.

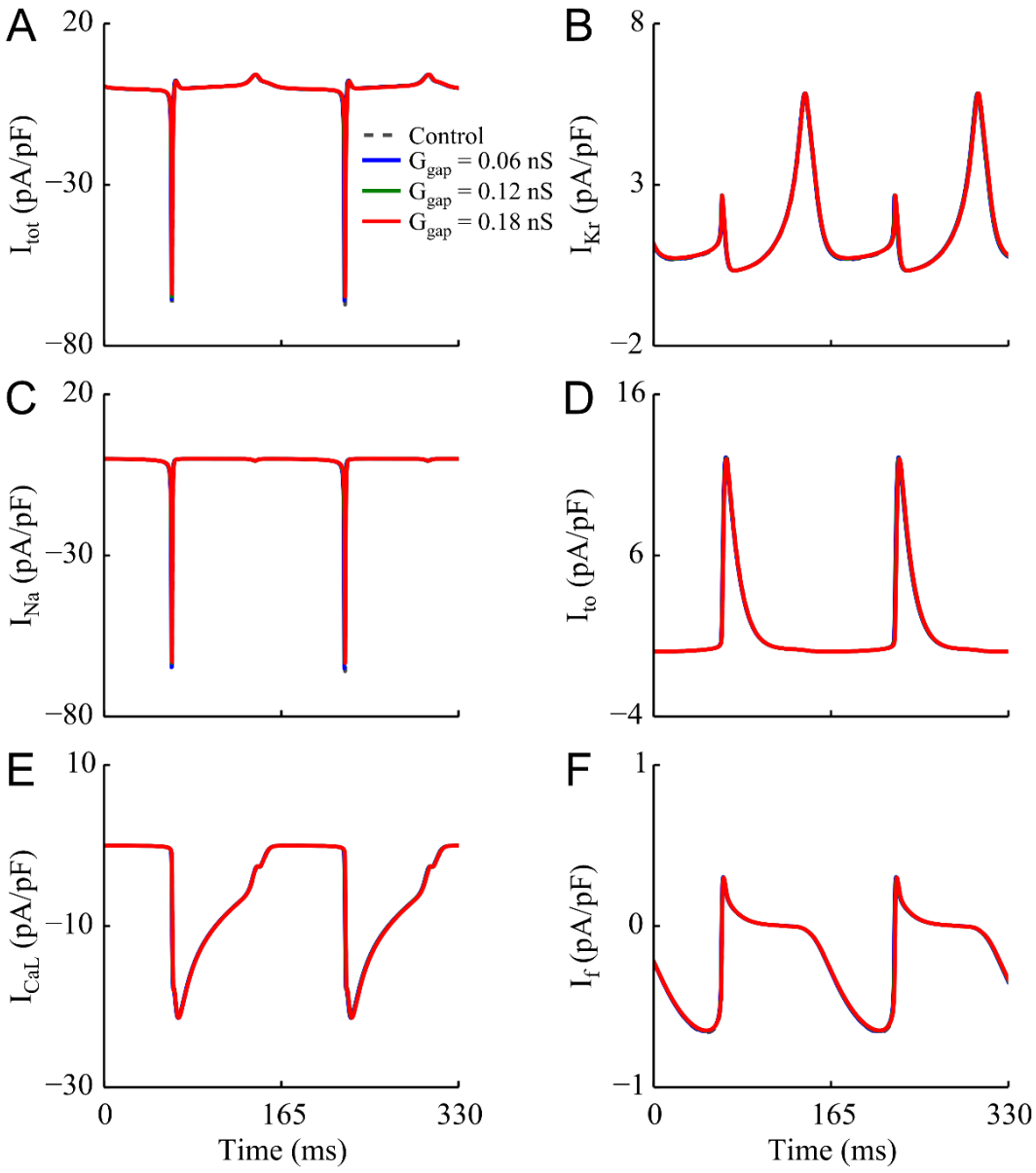

Figure 3.6 Effects of G_{gap} on the transmembrane currents in the myocyte in PSAN under weak coupling as a function of time. Changes in the (A) I_{tot}, (B) I_{Kr}, (C) I_{Na}, (D) I_{to}, (E) I_{CaL}, and\ (F) I_f of myocytes after coupling with a single fibroblast with a G_{gap} of 0.06 nS, 0.12 nS and 0.18 nS, respectively.

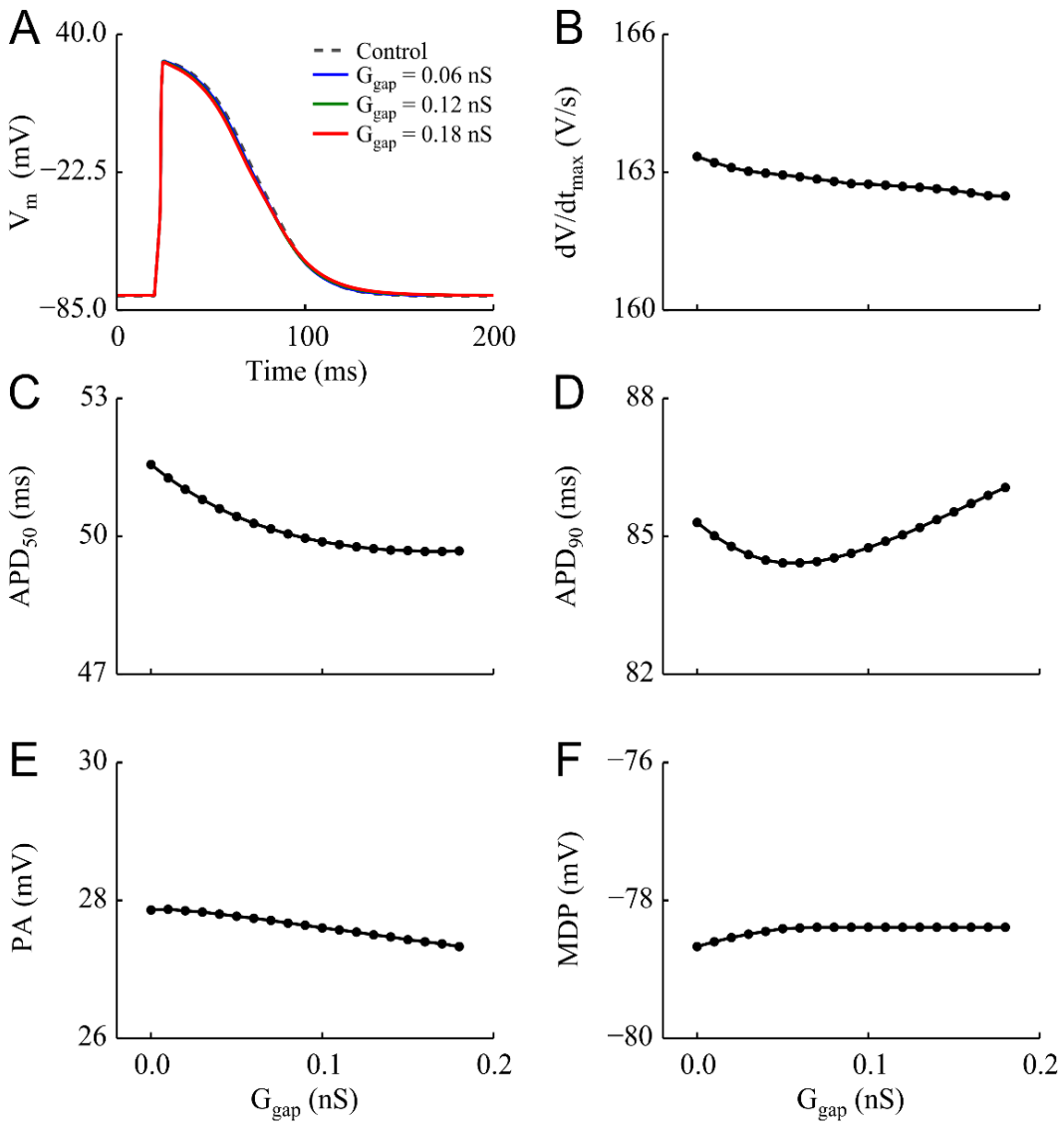

Figure 3.7 Effects of G_{gap} on the AP characteristics of myocytes in the atrium under weak coupling. Changes in the (A) AP, (B) dV/dt_{max}, (C) CL, (D) APD_{90}, (E) PA, and (F) MDP in myocytes.

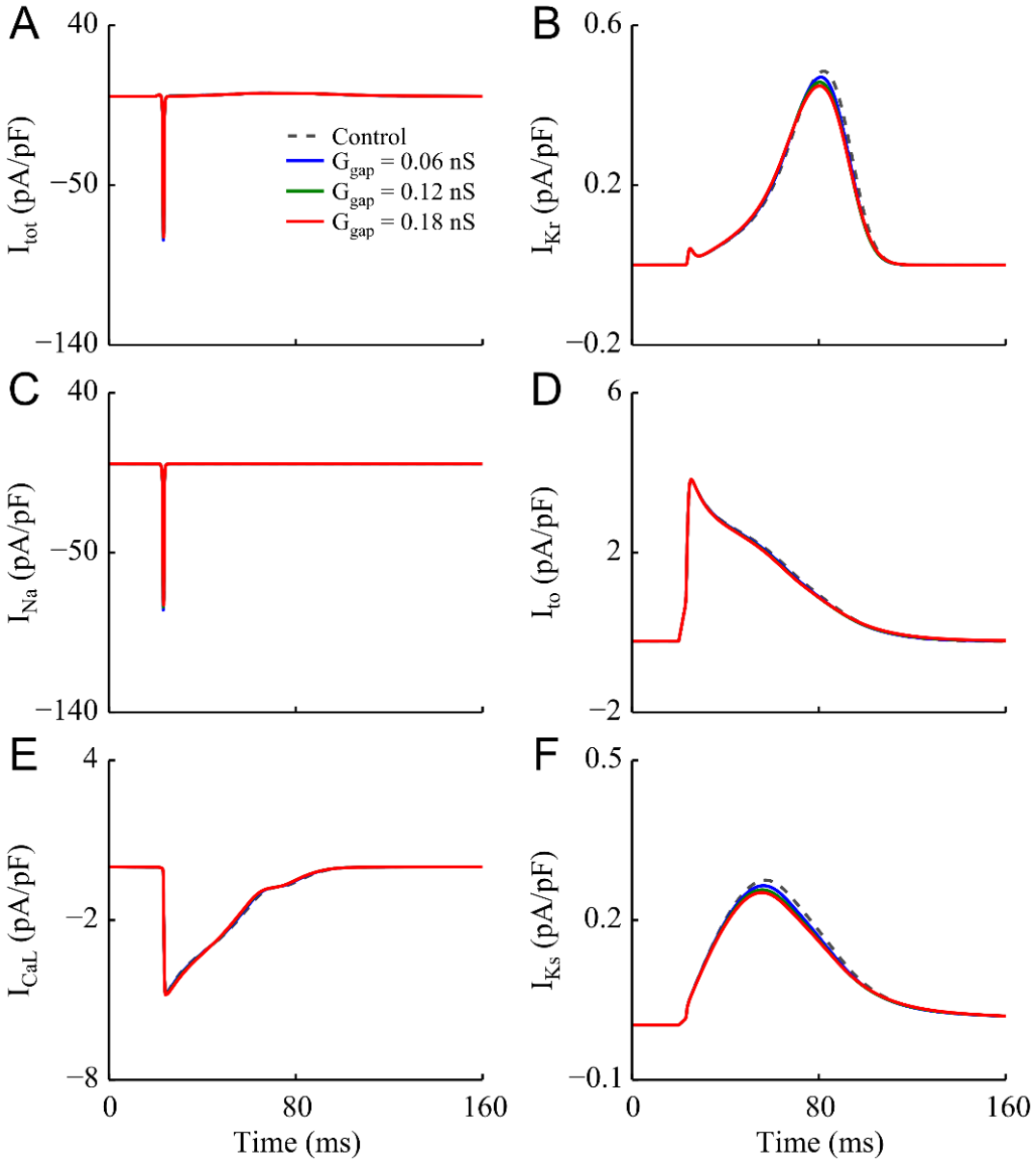

Figure 3.8 Effects of G_{gap} on the transmembrane currents in myocytes in the atrium under weak coupling as a function of time. Changes in the (A) I_{tot}, (B) I_{Kr}, (C) I_{Na}, (D) I_{to}, (E) I_{CaL}, and (F) I_{Ks} of myocytes after coupling with a single fibroblast with a G_{gap} of 0.06 nS, 0.12 nS and 0.18 nS, respectively.

3.3.2 Effects of Coupling Strength under Strong Coupling

The spontaneous activity is abolished when G_{gap} is larger than 0.18 nS in the CSAN. Therefore, in this section, we study only strong myocyte–fibroblast coupling in the PSAN and atrium by coupling a single fibroblast to a myocyte with a G_{gap} of 2 nS, 4 nS and 8 nS, respectively. As shown in Figure 3.9A, when the G_{gap} is increased from 2 nS to 4 nS, the dV/dt_{max} is decreased from 64.9 V/s to 63.34 V/s while the APD_{90} is

slightly prolonged. The strong coupling results in a larger PA in the fibroblast. It increases along with G_{gap} (from 16 mV with a G_{gap} of 2 nS to 17.86 mV with a G_{gap} of 4 nS and 21.3 mV with a G_{gap} of 8 nS). The peak outflow current ($I_{gap} > 0$) is strengthened, but the outflow duration is shortened, which means that the modifications in the depolarisation of coupled myocytes become greater.

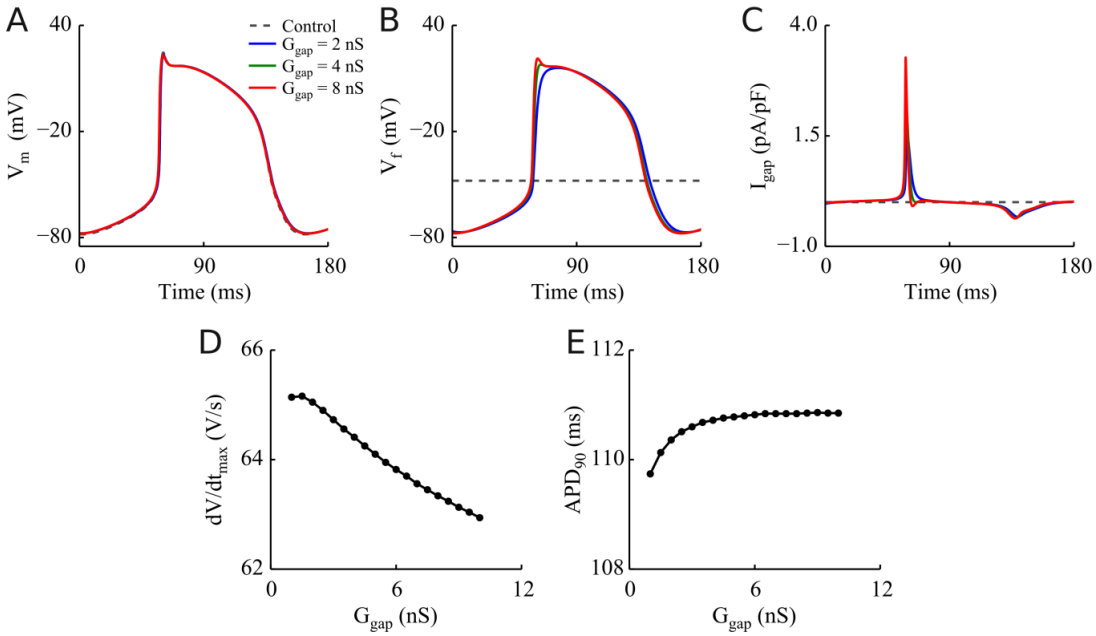

Figure 3.9 Effects of G_{gap} on the AP characteristics of myocytes in the PSAN under strong coupling. Changes in the (A) AP of myocytes, (B) membrane potential of fibroblasts, (C) I_{gap}, (D) dV/dt_{max}, and (E) APD_{90} in the coupled myocyte.

Figure 3.10 shows the coupling effects on transmembrane currents in control conditions and under strong coupling. After coupling with a G_{gap} of 2 nS, the I_{tot} and each individual current is slightly weakened, and the CL of each current is also prolonged with respect to the control value. However, the further increase in G_{gap} does not exert significant effects on each individual current.

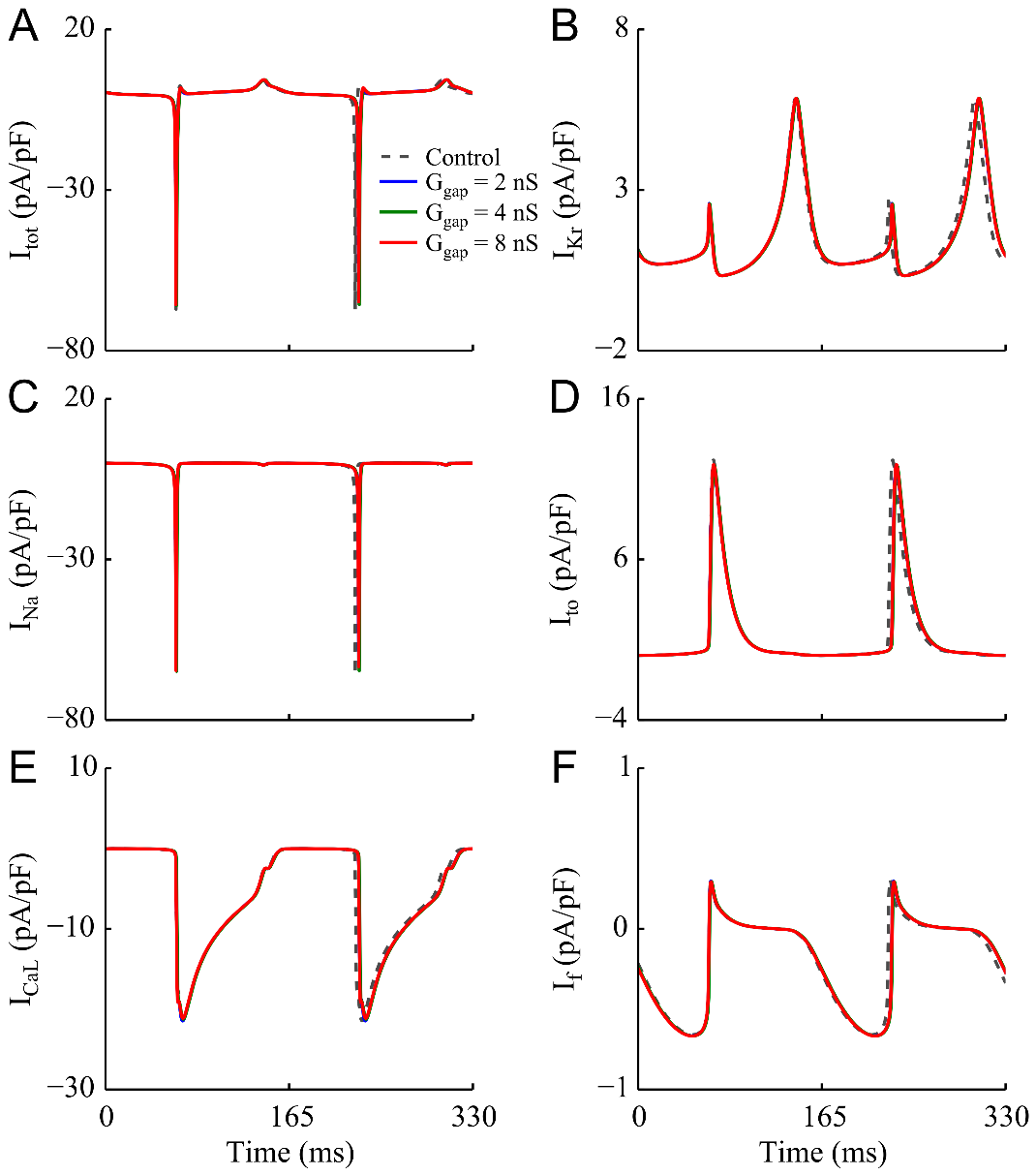

Figure 3.10 Effects of G_{gap} on the transmembrane currents of myocytes in the PSAN under strong coupling as a function of time. Changes in the (A) I_{tot}, (B) I_{Kr}, (C) I_{Na}, (D) I_{to}, (E) I_{CaL}, and (F) I_f in the myocytes after coupling with a single fibroblast with a G_{gap} of 0, 2 nS, 4 nS and 8 nS.

In the atrium, as shown in Figure 3.11A, the PA of myocytes under strong coupling is small versus the control value. After the G_{gap} is increased from 2 to 15 nS, the dV/dt_{max} is decreased from 160.6 V/s (control) to 151.78 V/s (G_{gap} = 15 nS), suggesting a decrease in the depolarisation rate (Figure 3.11D). The APD_{90} shows a distinct change compared to the weak coupling case, which is first prolonged (by 1.9%) and then followed by a plateau when G_{gap} is over 6 nS (Figure 3.11E). The PA of the coupled

fibroblast becomes larger comparing to under weak coupling, which increases along with the G_{gap}.

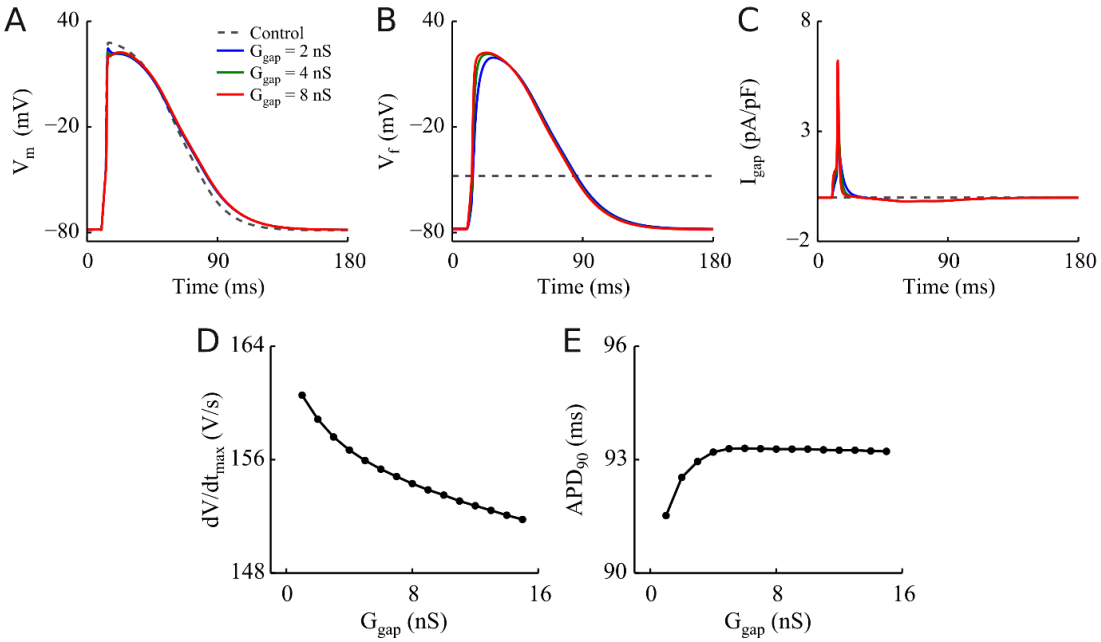

Figure 3.11 Effects of G_{gap} on the AP characteristics of myocytes in the atrium under strong coupling. Changes in the (A) AP of myocytes, (B) membrane potential of fibroblast, (C) I_{gap}, (D) dV/dt_{max}, and (E) APD_{90}.

Figure 3.12 shows the coupling effects on transmembrane currents under control condition and strong coupling (G_{gap} = 2, 4, 8 nS). After coupling a fibroblast with a G_{gap} of 2 nS, the I_{CaL} and I_{Na} are strengthened by 4% and 4.1%, respectively (Figure 3.12C and E). The outward currents including I_{Kr}, I_{to}, and I_{ks} are weakened (Figure 3.12B, D and F). Further increasing G_{gap} to 8 nS, the peak I_{tot} and I_{Na} are declined dramatically (28.2% in I_{tot} and 26.5% in I_{Na}), while the outward currents do not show significant changes.

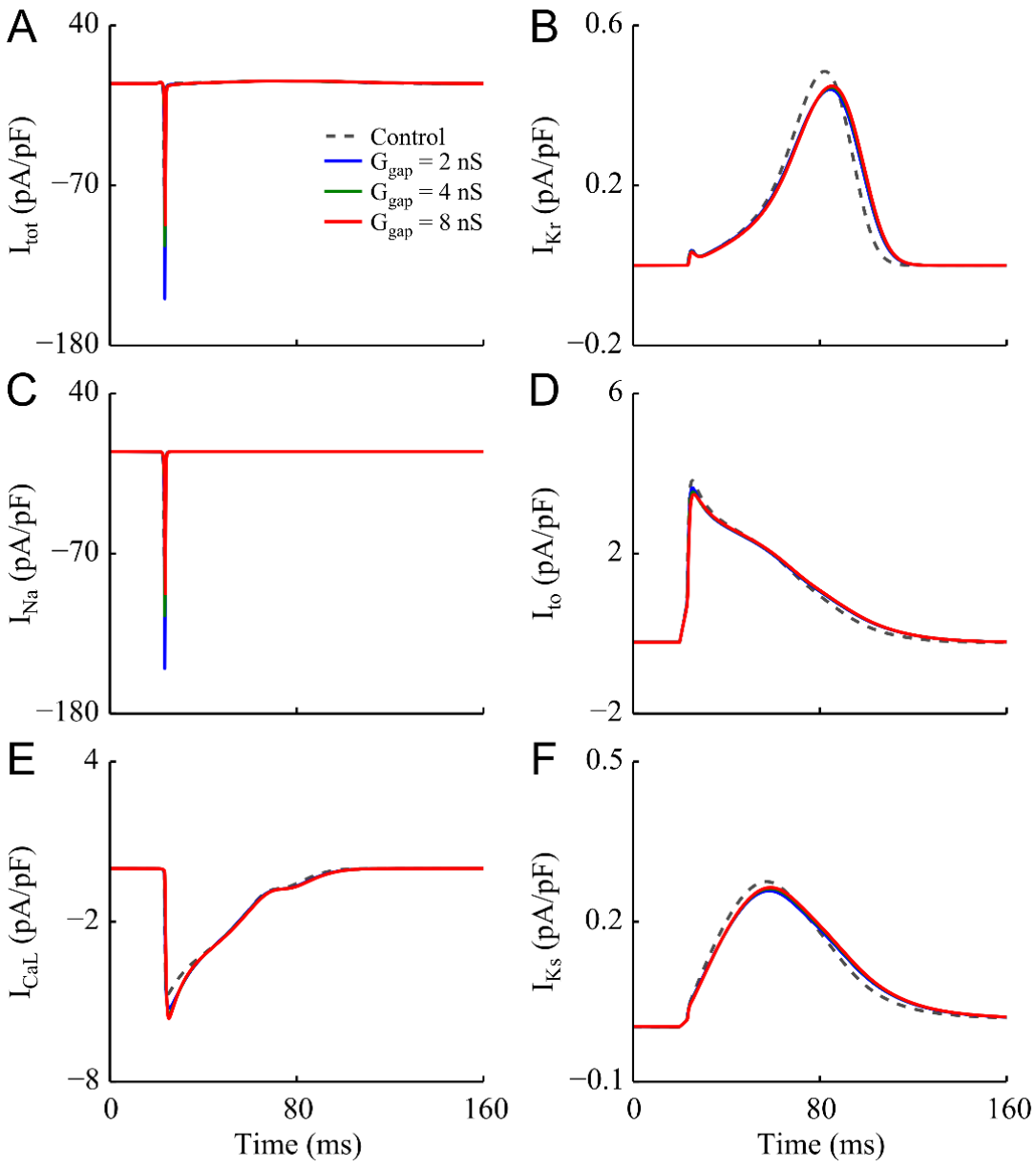

Figure 3.12 Effects of G_{gap} on the transmembrane currents of myocytes in the atrium under strong coupling as a function of time. (A) I_{tot}, (B) I_{Kr}, (C) I_{Na}, (D) I_{to}, (E)I_{CaL}, and (F) I_f in myocytes after coupling with a single fibroblast with a G_{gap} of 0, 2 nS, 4 nS and 8 nS, respectively.

3.3.3 Effects of Coupling Fibroblast Number under Weak Coupling

To investigate the effect of coupling fibroblast number on electrical activity in the SAN and atrium under weak coupling, a myocyte was coupled to a varying number of fibroblasts (0 to 15) with a fixed G_{gap} of 0.01 nS. Generally, after coupling with more fibroblasts, the peak I_{gap} is enlarged (Figure 3.13G–I), and the membrane potential amplitude of each coupled fibroblast decreases in the CSAN but does not show

significant changes in the PSAN and atrium (Figure 3.13D–F). After coupling with 15 fibroblasts in CSAN, the spontaneous activity in myocytes is abolished, the I_{gap} vanishes and the membrane potential of each coupled fibroblast decreases to its resting value. The myocyte APA shows a marked reduction in the CSAN but does not change significantly in the PSAN and atrium.

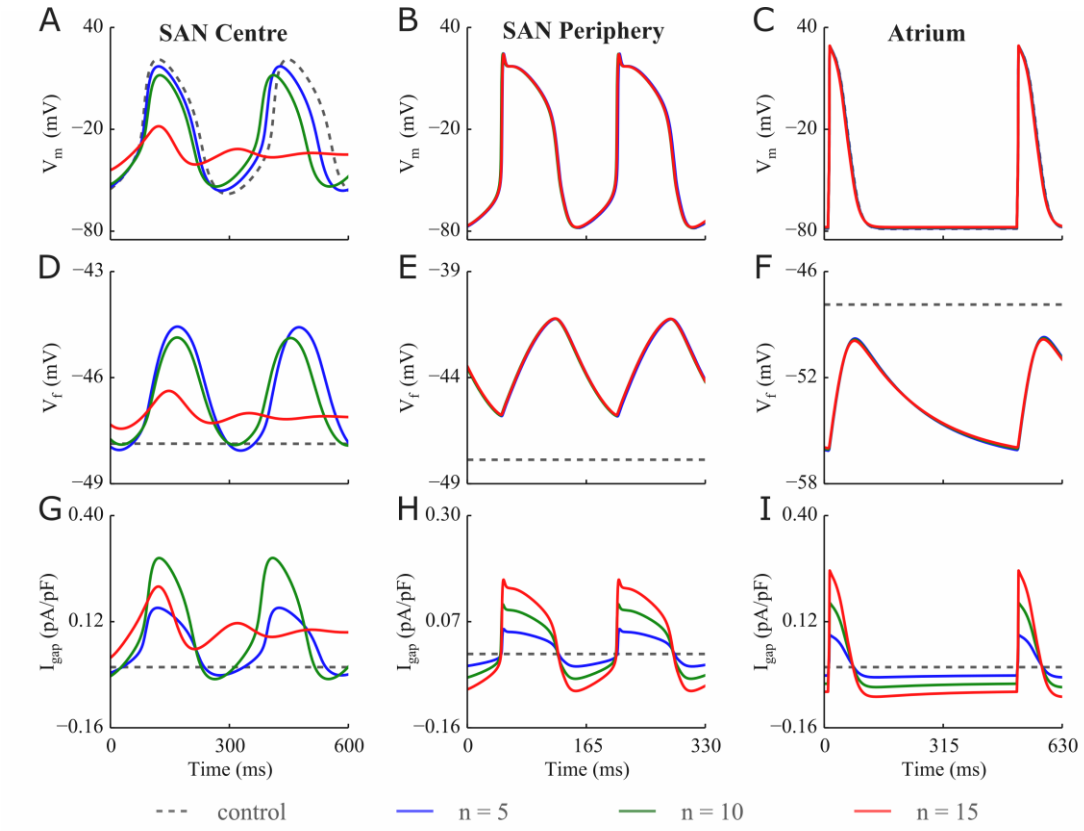

Figure 3.13 Effects of coupling fibroblast number on electrical activity in the myocytes and coupled fibroblasts in the SAN and atrium under weak coupling as a function of time. The simulated membrane potential changes in myocytes (A, B, and C) and coupled fibroblasts (D, E, and F) as well as the gap junction current (G, H, and I) in the CSAN, PSAN, and atrium after coupling with a G_{gap} of 0.01 nS.

In CSAN, as shown in Figure 3.14, after coupling with more fibroblasts, the PA decreases and the MDP becomes less negative in myocytes. The APA is declined by 7.7% with 5 fibroblasts and 17.3% with 10 fibroblasts. The dV/dt_{max} also shows a reduction of 12.8% and 28.9% after coupling with 5 and 10 fibroblasts, decreasing from 2.66V/s (control) to 2.32 V/s (5 fibroblasts) and 1.89 V/s (10 fibroblasts), respectively. The CL and APD_{90} are shortened by 12.6% and 12.8%, respectively after

coupling with 10 fibroblasts. When the coupling fibroblast number is increased to 15, the spontaneous activity in the CSAN is abolished. The effects of the coupling fibroblast number of fibroblasts on the transmembrane currents are presented in Figure 3.15, with an increase in the coupling fibroblast number from 0 to 10, both the outward current and inward current are weakened, resulting in a reduction of 17.3 % in I_{tot}. The I_{tot} vanishes after coupling with 15 fibroblasts.

In the PSAN, as shown in Figure 3.16A, the effects of coupling fibroblast number on the AP are very small in the PSAN versus in the CSAN under weak coupling. After coupling with 15 fibroblasts, the PA is decreased slightly and the MDP becomes less negative, therefore resulting in a small reduction in APA; the dV/dt_{max} is decreased from 67.6 V/s (control) to 65.50 V/s; the CL and APD_{90} are both shortened slightly. Figure 3.17 shows the effect of coupling fibroblast number on the transmembrane currents of myocyte. The results suggest under weak coupling, even coupling with 15 fibroblast, the changes in each transmembrane current in PSAN are still very small compared to the results in the CSAN.

In the atrium, as shown in Figure 3.18, when the coupling fibroblast number is increased from 0 to 15, the dV/dt_{max} drops from 163.3 V/s to 157.8 V/s, by 3.4%, and the APD_{50} and APD_{90} are shortened by 28.3% and 3.4%, respectively. The PA becomes less depolarised, with a reduction of 5.9%, while the MDP becomes more positive, with an elevation of 2.3%. As illustrated in Figure 3.19, the coupling fibroblast number does not exert significant effects on the I_{tot} and inward currents (I_{CaL} and I_{Na}) in coupled myocytes, while the outward currents I_{kr} and I_{ks} are slightly strengthened.

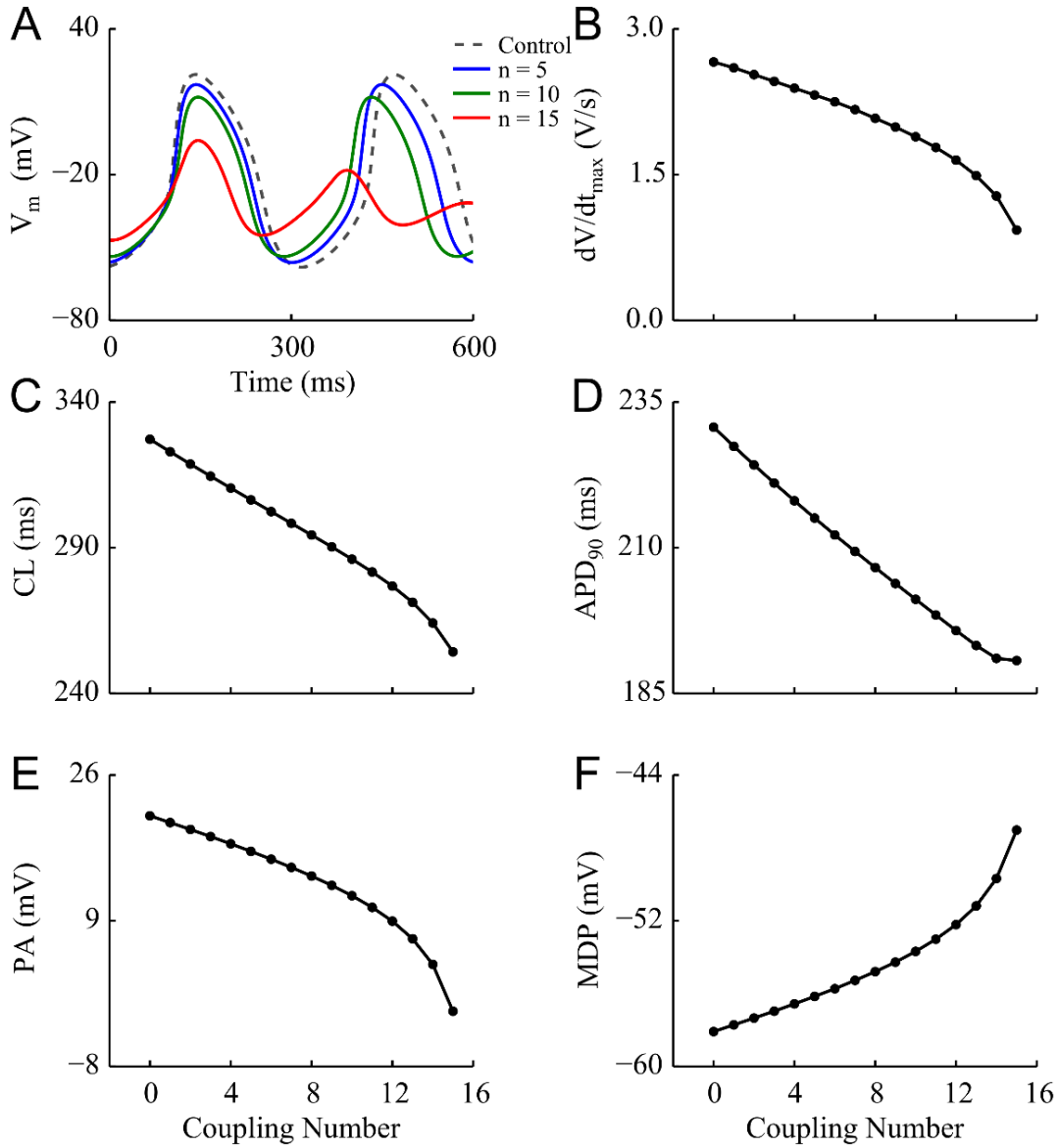

Figure 3.14 Effects of coupling fibroblast number (n) on the AP characteristics of myocytes in the CSAN under weak coupling. Changes in the (A) AP, (B) dV/dt_{max}, (C) CL, (D) APD_{90}, (E) PA, and (F) MDP in the coupled myocytes.

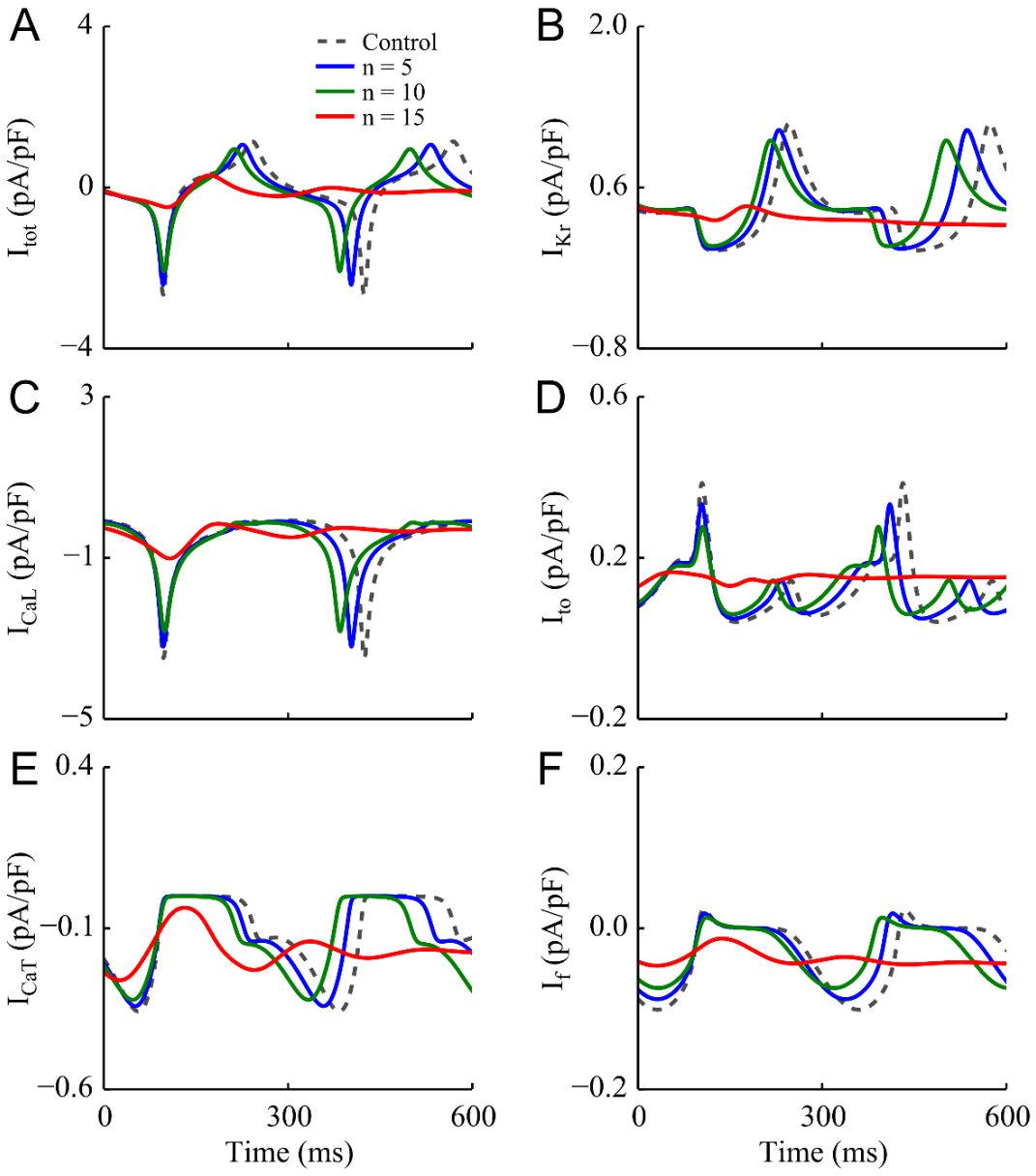

Figure 3.15 Effects of coupling fibroblast number (n) on the transmembrane currents of the myocyte in CSAN under weak coupling as a function of time. Changes in (A) I_{tot}, (B) I_{Kr}, (C) I_{CaL}, (D) I_{to}, (E) I_{CaT}, and (F) I_f after coupling with an increasing number of fibroblasts (G_{gap}= 0.01 nS).

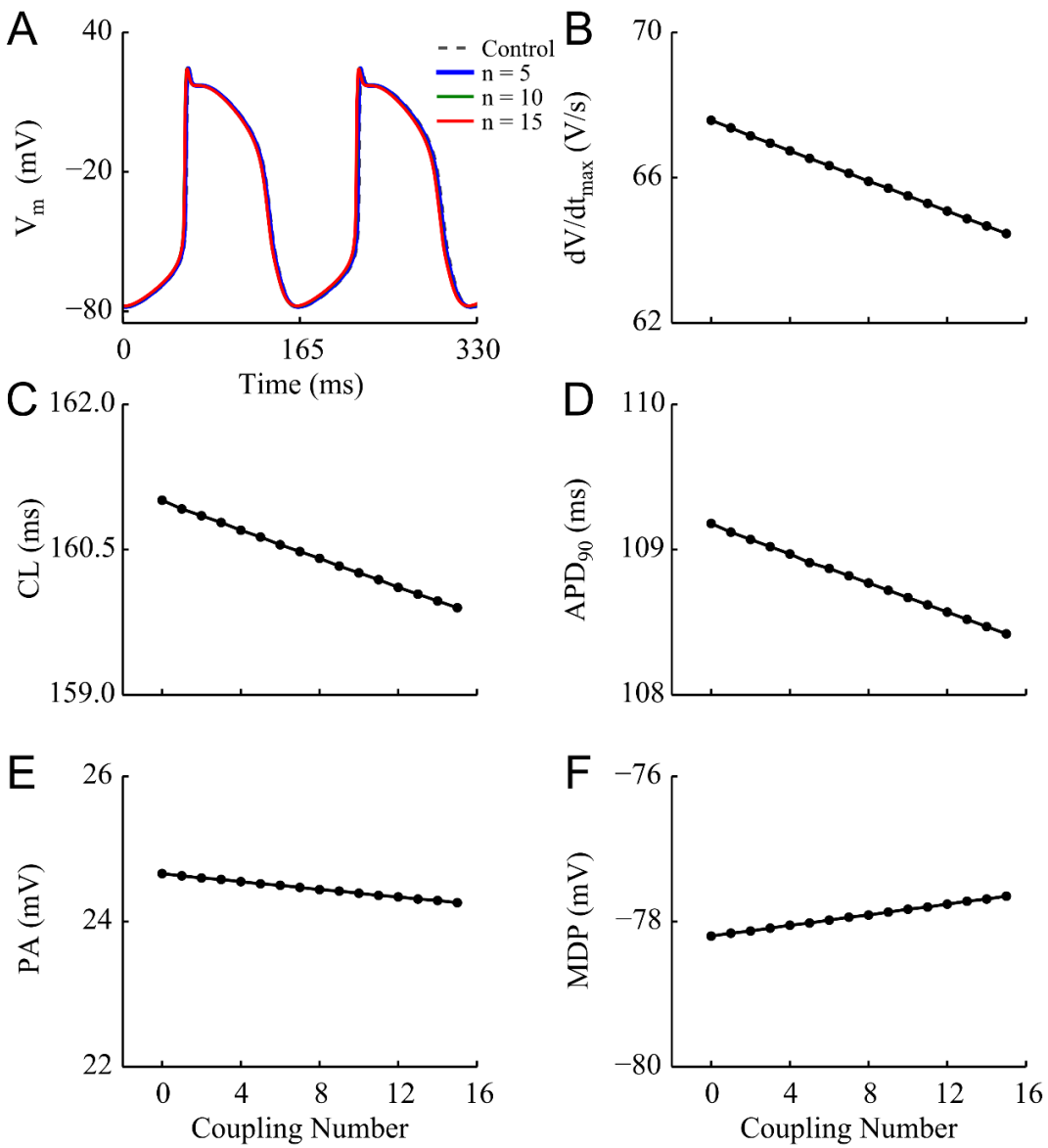

Figure 3.16 Effects of coupling fibroblast number (n) on the AP characteristics of myocytes in the PSAN under weak coupling. Changes in the (A) AP, (B) dV/dt_{max}, (C) CL, (D) APD_{90}, (E) PA, and (F) MDP of the coupled myocytes.

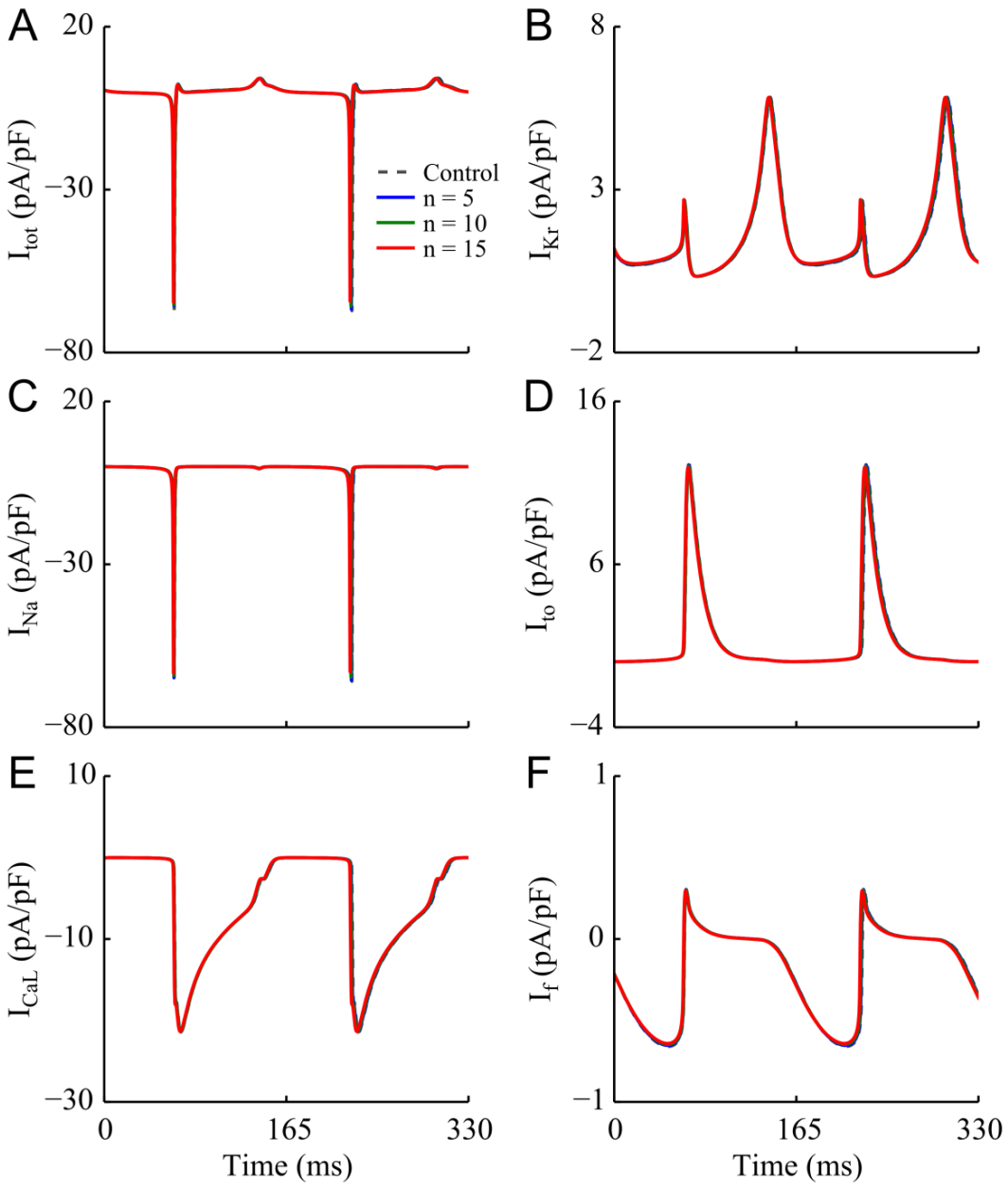

Figure 3.17 Effects of coupling fibroblast number (n) on the transmembrane currents of myocytes in the PSAN under weak coupling as a function of time. Changes in (A) I_{tot}, (B) I_{Kr}, (C) I_{Na}, (D) I_{to}, (E) I_{CaL}, and (F) I_f after coupling with an increasing number of fibroblasts (G_{gap}= 0.01 nS).

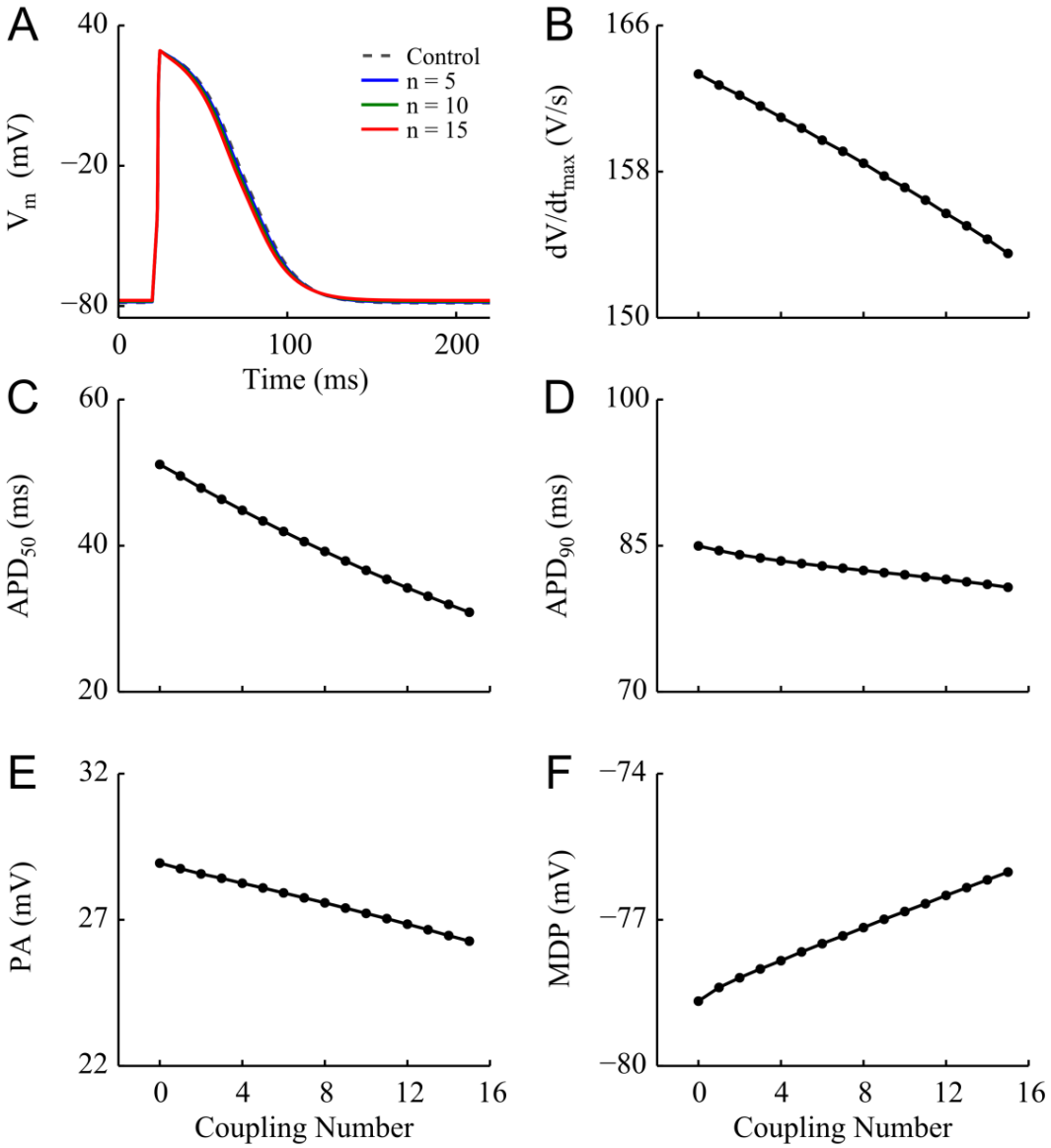

Figure 3.18 Effects of coupling fibroblast number (n) on the AP characteristics of myocytes in the atrium under weak coupling (G_{gap} = 0.01 nS). Changes in the (A) AP, (B) dV/dt_{max}, (C) CL, (D) APD_{90}, (E) PA, and (F) MDP of the coupled myocyte.

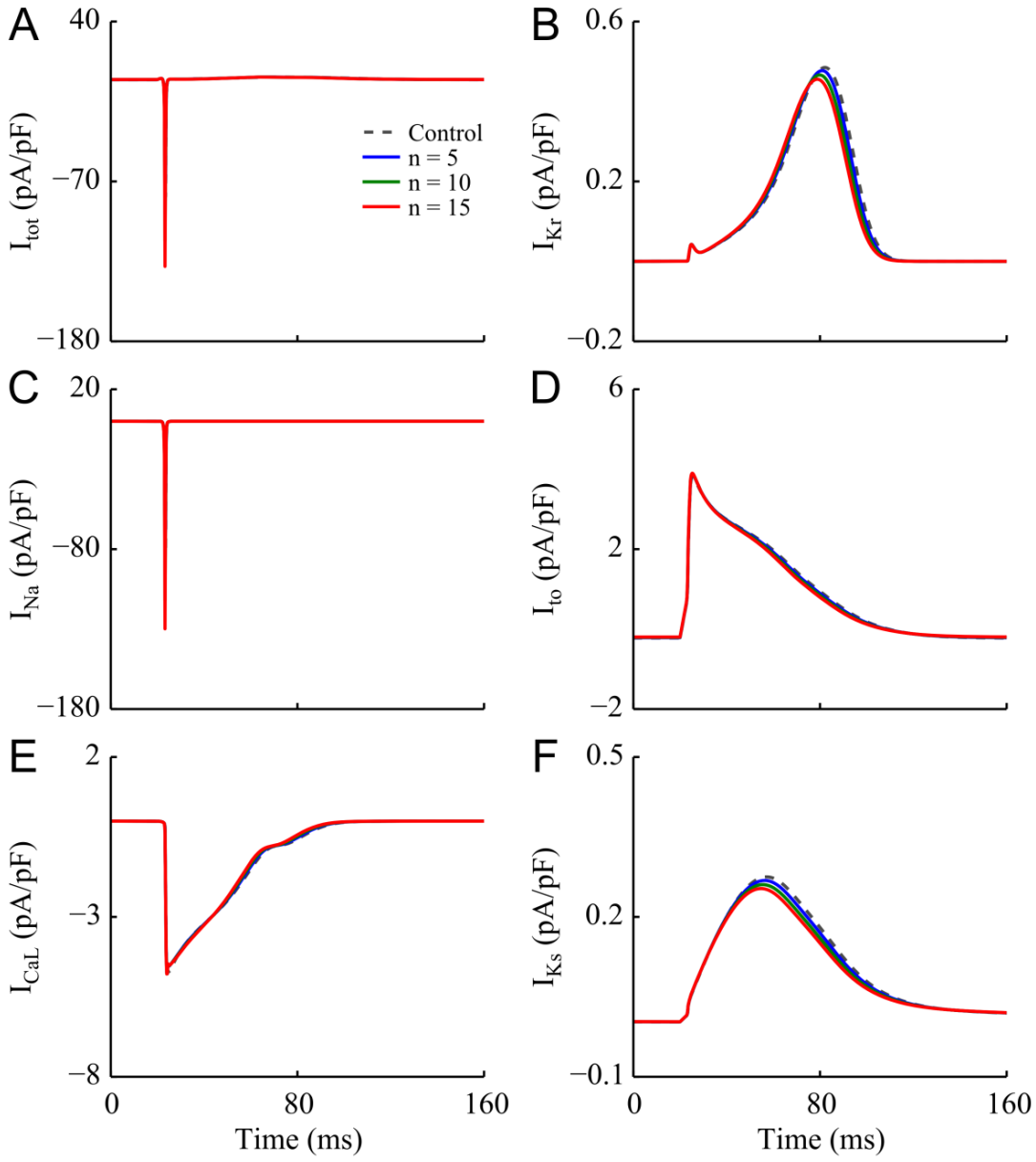

Figure 3.19 Effects of coupling fibroblast number (n) on the transmembrane currents of myocytes in the atrium under weak coupling as a function of time. Changes in (A) I_{tot}, (B) I_{Kr}, (C) I_{Na}, (D) I_{to}, (E) I_{CaL}, and (F) I_f after coupling with an increasing number of fibroblasts (G_{gap}= 0.01 nS).

3.3.4 Effects of Coupling Fibroblast Number under Strong Coupling

In strong coupling case, a varying number of fibroblasts (0, 2, 4, and 8) were coupled to a myocyte in the SAN and atrium with a G_{gap} of 1 and 10 nS. Our previous study

suggests that the spontaneous activity of myocytes in the CSAN is abolished when G_{gap} is increased to 0.18 nS, therefore, we just discuss the effects of coupling fibroblast number on myocytes in the PSAN and atrium in this section in the strong coupling case.

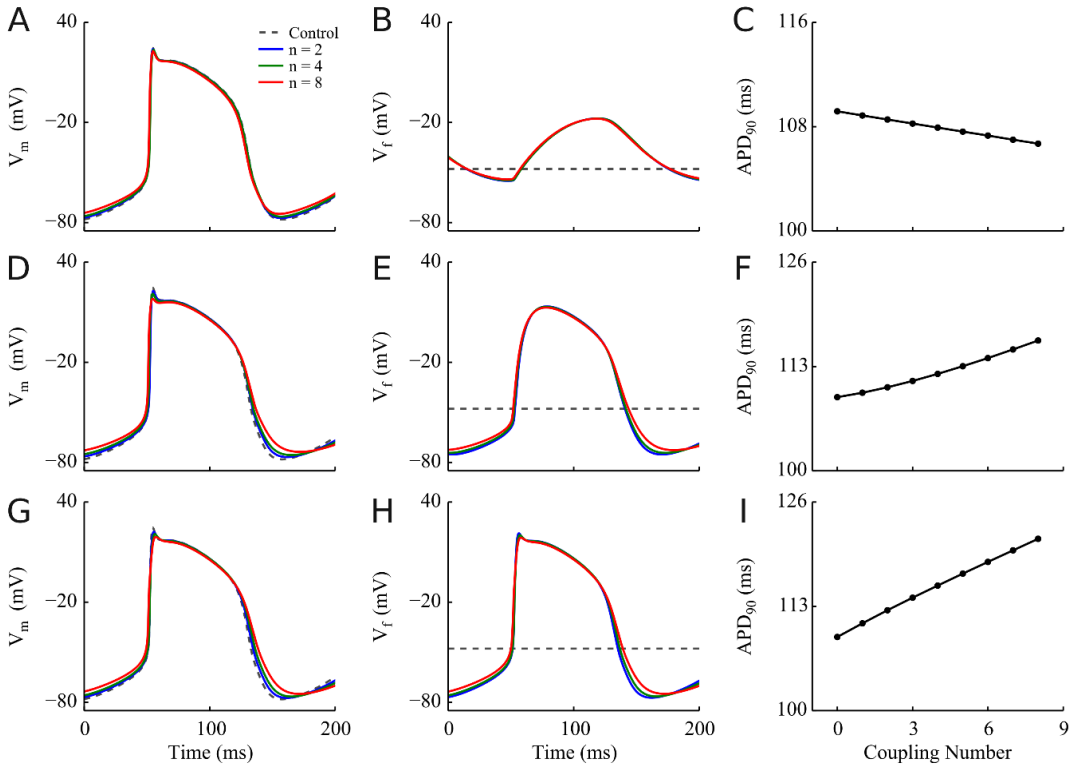

Figure 3.20 Effects of coupling fibroblast number (n) on myocytes in the PSAN with different coupling strengths: (A–C) weak coupling with a G_{gap} of 0.1 nS, (D–F) strong coupling with a G_{gap} of 1 nS, (G–H) strong coupling with a G_{gap} of 10 nS. Coupling effects on the AP of myocyte (A–G), the membrane potential of fibroblasts (B–F), and APD_{90} of myocytes (C–I) are shown.

Figure 3.20 shows the effects of coupling fibroblast number on the AP of myocytes, the membrane potential of fibroblasts, and the APD_{90} of the coupled myocytes. The coupling fibroblast number exerts a larger effect on the AP with a G_{gap} of 1 nS (Figure 3.20D) and 10 nS (Figure 3.20G) in comparison to the results under weak coupling (Figure 3.20A). The APD_{90} decreases along with the increase in the coupling fibroblast number when G_{gap} is 0.1 nS (from 85 ms with 2 fibroblasts to 82.8 ms with 8 fibroblasts). However, it shows a distinct change under strong coupling, where it is prolonged by 12.4% (G_{gap} = 1 nS) and 21.5% (G_{gap} = 10 nS) as the coupling fibroblast number is increased from 2 to 8. Moreover, the reductions in the PA and dV/dt_{max}

resulting from the increase in the coupling fibroblast number become more significant with a larger G_{gap} (Figure 3.21).

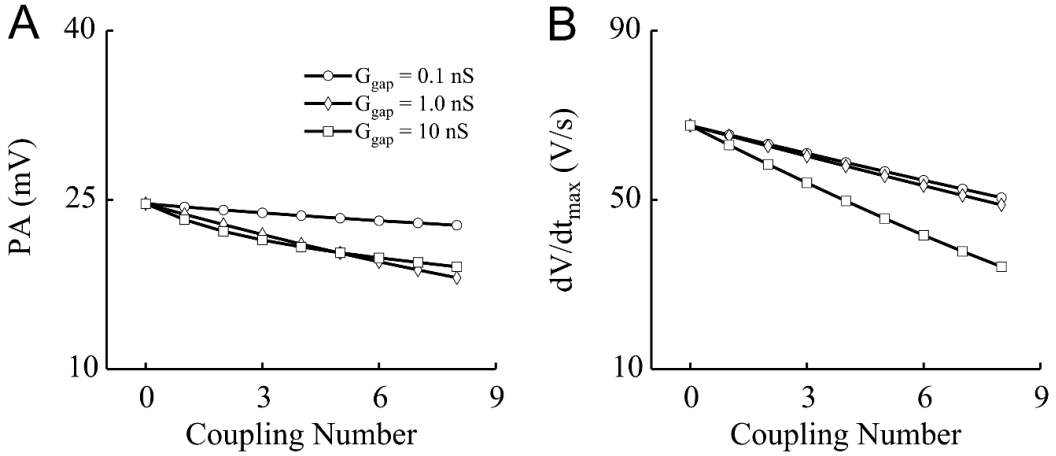

Figure 3.21 Effects of coupling fibroblast number on the characteristics of the coupled myocytes in the PSAN : (A) PA; (B) dV/dt_{max}.

In the atrium, as shown in Figure 3.22, with the increase in coupling strength, the effects of coupling fibroblast number on both myocytes and coupled fibroblasts increase. While coupling with a G_{gap} of 0.1 nS, the increasing coupling fibroblast number exerts a marked effect on the dynamics of myocyte repolarisation. After coupling with 8 fibroblasts, the accelerated repolarisation results in a reduction of 2.6% in APD_{90} versus the control. The dV/dt_{max} is also decreased from 163.3 V/s to 158.5 V/s. More profound effects in the AP of myocytes can be observed after coupling with a G_{gap} of 1 nS as shown in Figure 3.22D and G. After the coupling fibroblast number is increased from 0 to 8, the PA is decreased from 28.9 mV to 13.2 mV, the APD_{90} is prolonged by 41.4%, suggesting a slower repolarisation process, and the dV/dt_{max} is decreased by 13.6% from 163.3 V/s to 141 V/s. When G_{gap} is 10 nS, the prolongation of APD_{90} becomes even more significant, which is increased by 71.5% with 7 fibroblasts. The AP is abolished when coupling with more fibroblasts. The reduction in dV/dt_{max} also increases (Figure 3.23B, from 163.4 V/s in the control to 61.7 V/s with 7 fibroblasts). Moreover, the peak membrane potential of each coupled fibroblast becomes more depolarised with a larger G_{gap}. It decreases along with the increase in the coupling fibroblast number with a fixed G_{gap}.

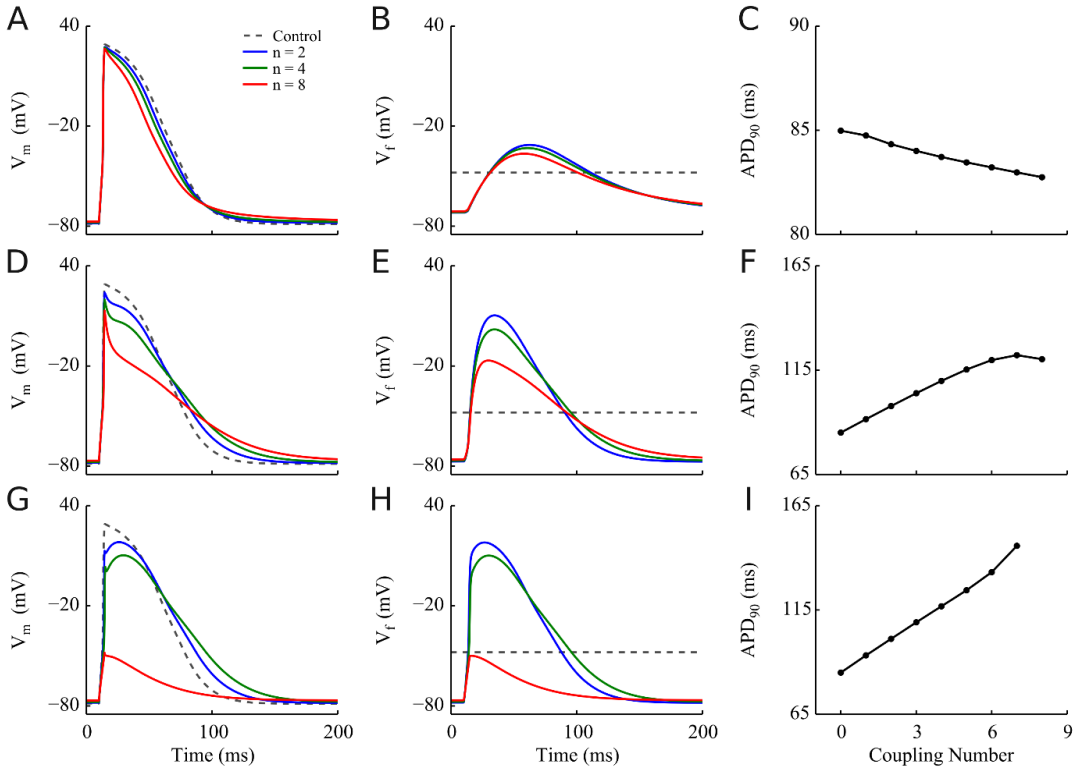

Figure 3.22 Effects of coupling fibroblast number (n) on myocytes in the atrium with different coupling strengths : (A–C) G_{gap} = 0.1 nS, weak coupling; (D–F) G_{gap} = 1 nS, strong coupling; and (G–H) G_{gap} = 10 nS strong coupling. Coupling effects on the AP of myocytes (A–G), the membrane potential of fibroblasts (B–F), and APD_{90} of myocytes are shown.

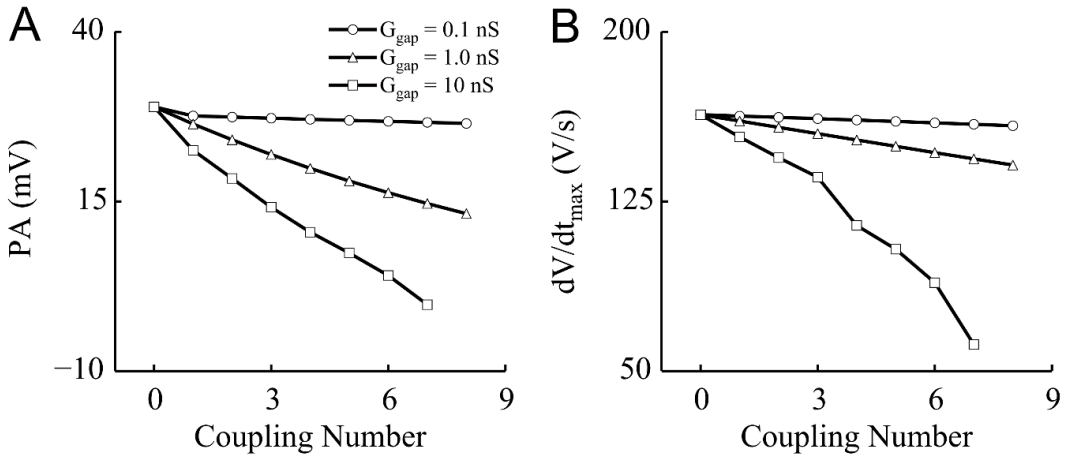

Figure 3.23 Effects of coupling fibroblast number on the characteristics of myocytes in the atrium: (A) PA and (B) dV/dt_{max}.

3.3.5 Action Potential Propagation in M-nF-M Connection

A G_{gap} of 0-30 nS was selected to investigate the effects of G_{gap} on AP propagation in myocyte–fibroblast–myocyte (M-F-M) connection. As shown in Figure 3.24, when no fibroblast connects the two myocytes, the membrane potentials of the first fibroblast and the last myocyte remain at 0. When the G_{gap} is over the threshold value (6 nS), the AP can be propagated to the next myocyte via a connecting fibroblast. The electrophysiology of both myocytes shows some significant changes as compared to it in control. The repolarisation process of the AP in the first myocyte becomes more complicated, involving a second depolarisation after the AP enters its repolarisation process (Figure 3.24A). Moreover, with an increase in G_{gap} from 7 nS to 24 nS, the PA of the first myocyte drops by 81.4% from 20.4 mV to 7.8 mV, while the PA of the last myocyte shows an inverse change, increasing from 10.6 mV to 12.37 mV. The dV/dt_{max} of the first myocyte is decreased from 148.8 V/s to 131 V/s, whilst the dV/dt_{max} in the last myocyte is increased from 116.4 V/s to 142.7 V/s (Figure 3.24D).

The AP propagation from the first myocyte to the next myocyte interconnected with a strand of fibroblasts (M-nF-M) was also studied. We selected a varying number of connecting fibroblast (0, 3, 5, and 7), and G_{gap} was set to 18 nS for each coupling number. As shown in Figure 3.25, the AP waveform of the first myocyte is significantly modulated after connecting with another myocyte with simply one fibroblast with a G_{gap} of 18 nS. The PA is dramatically decreased by 58%, and the APD_{90} is prolonged by 12.5%. After increasing the coupling fibroblast number from 1 to 6, the PA of the first myocyte does not show significant changes, whereas it is decreased from 12.4 mV to -2.53 mV in the last myocyte (Figure 3.26A). The APD_{90} in both myocytes is prolonged first and then dramatically decreases (Figure 3.26B). The dV/dt_{max} in the first myocyte does not show significant changes, but declines by 62.3% from 138 V/s with 1 fibroblast to 52 V/s with 6 fibroblasts (Figure 3.26C). The conduction time for AP to be propagated from the first myocyte to the last myocyte is increased from 2.9 ms with 1 fibroblast to 25.9 ms with 6 fibroblasts. The AP of the last myocyte cannot be activated when the interconnecting fibroblast number is more than 6.

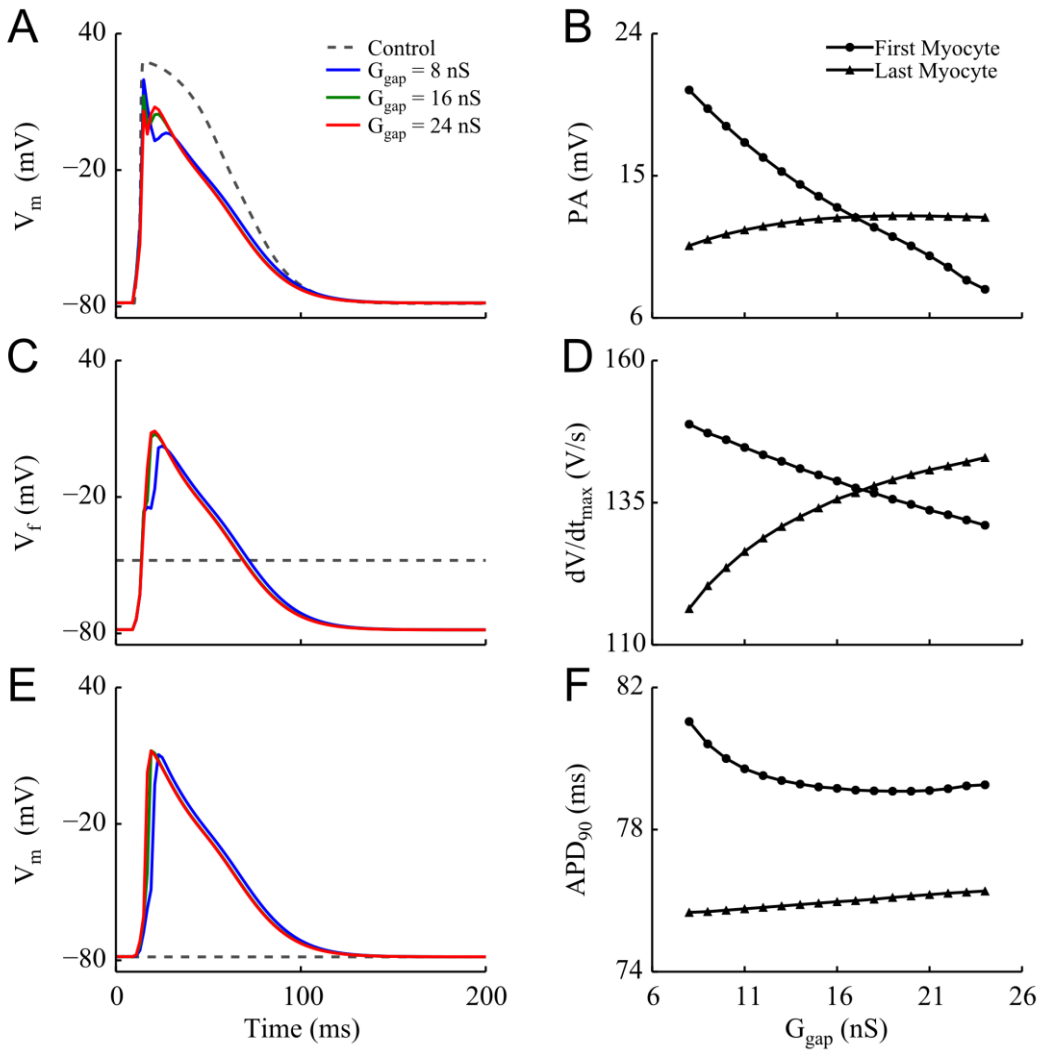

Figure 3.24 Effects of G_{gap} on the electrical activities in the M-F-M connection : (A) AP of the first myocyte, (C) membrane potential of fibroblasts, (E) AP of the last myocyte, (B) PA, (D) dV/dt_{max}, and (F) APD_{90}.

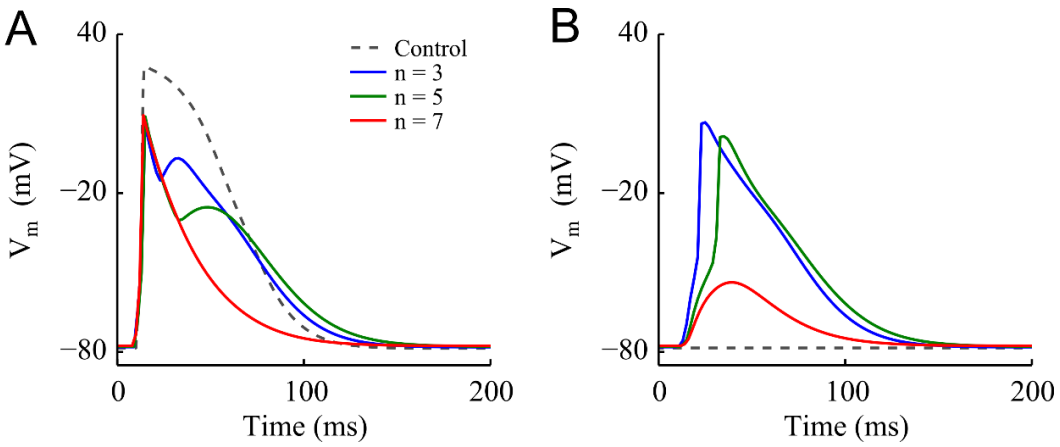

Figure 3.25 Simulated results of AP propagation in M-nF-M strand configuration. (A) AP of the first myocyte; (B) AP of the last myocyte.

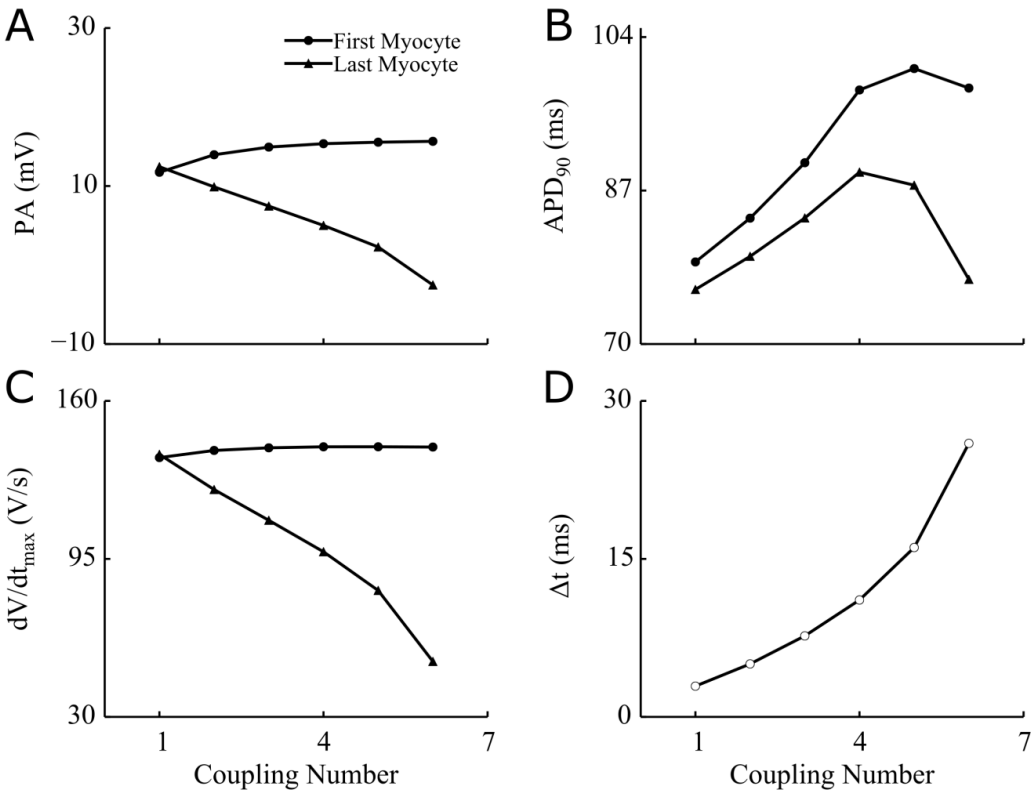

Figure 3.26 Effects of fibroblast number on the AP characteristics of myocytes in M-nF-M strand configuration. (A) PA, (B) APD_{90}, (C) dV/dt_{max}, and (D) conduction time from the first myocyte to the last myocyte.

3.4 Summaries and Discussions

The coupling effect of fibroblasts on the electrical activity of myocytes in the central SAN, peripheral SAN, and atrium were simulated in three fibroblast–myocyte coupling models: a CSAN model, PSAN model, and atrial model. The effects of G_{gap} and coupling fibroblast number on coupling were also investigated. Table 3.1 shows the coupling effect on the AP characteristics in each model under different coupling conditions.

		Weak Coupling		Strong Coupling	
		N = 1, G_{gap} ↑	G_{gap} = 0.01 nS N ↑	N = 1, G_{gap} ↑	G_{gap} = 10 nS N ↑
CSAN	APA	↓	↓	–	–
	dV/dt_{max}	↓	↓	–	–
	APD_{90}	↓	↓	–	–
	CL	↓	↓	–	–
PSAN	APA	↓	↓	↓	↓
	dV/dt_{max}	↓	↓	↓	↓
	APD_{90}	↓	↓	↑	↑
	CL	↑	↓	↑	↑
Atrium	APA	↓	↓	↓	↓
	dV/dt_{max}	↓	↓	↓	↓
	APD_{90}	↓↑	↓	↑	↑
	APD_{50}	↓	↓	↓	↓

Table 3.1 Coupling effects on characteristics of myocytes in the SAN centre (CSAN), SAN periphery (PSAN) and atrium. N is the coupling number, − represents not applicable, ↑ represents an increase, ↓ represents decrease, and ↓↑ represents a decrease followed by an increase.

3.4.1 Mechanism Underlying the Coupling

Generally, the fibroblast acts as a leaky capacitor in the myocyte–fibroblast coupling. It has a more positive resting membrane potential versus myocytes. Therefore, when the fibroblast is coupled to a myocyte, the current flows from fibroblasts to myocytes through the gap junction channels because of the drive of the potential gradient ($I_{gap} < 0$, outflow). After they reach the same potential ($I_{gap} = 0$), the ongoing depolarisation process of myocytes produces a reversal potential gradient; therefore, the current starts to flow back to charge the fibroblast ($I_{gap} > 0$, reflow), and the membrane potential of coupled fibroblasts increases along with the increase in I_{gap}. During the repolarisation phase of myocytes, when the membrane potential of a myocyte drops to the same level as that of the fibroblast (Igap = 0), the charging process of the fibroblasts stops and the discharge process begins; the current flows to the myocyte from the coupled fibroblast ($I_{gap} < 0$, outflow). The duration of each process greatly depends on the gap junction conductance (G_{gap}) and the coupled fibroblast number.

3.4.2 Effects of G_{gap} and coupling fibroblast number on AP Waveform

The dV/dt_{max} represents the maximum upstroke rate in myocytes. As shown in Table 3.2, it decreases along with the increase in G_{gap} after coupling with a single fibroblast. The result is consistent with *in vitro* studies in the murine SAN [47] and atrium [57]. This is because the increase in G_{gap} produces a greater I_{gap} flowing from the myocyte to the fibroblast during the upstroke of the myocyte; as a result, the upstroke rate becomes slower. A reduction in dV/dt_{max} can also be observed after increasing the coupling number with a fixed G_{gap}, because of the enlargement of total I_{gap} leaking from the myocyte to the fibroblasts as shown in section 3.3.3.

The dominant current during the upstroke of a myocyte is I_{CaL} in the CSAN and I_{Na} in the PSAN and atrium. The larger time constant in I_{CaL} results in a slower upstroke in the CSAN. After coupling with a fibroblast, currents flow out from the myocyte through the gap junction to charge the coupled fibroblast; therefore, the upstroke in the CSAN can be abolished when G_{gap} is increased to a certain value. This explains why the AP initiation in the CSAN is abolished under strong coupling. For myocytes in the PSAN and atrium, the effects of coupled fibroblasts on the depolarisation of the corresponding myocytes are much smaller, because of the high intrinsic upstroke rate, showing a small decrease in dV/dt_{max}.

The PA of the myocyte also becomes less depolarised after coupling with a larger G_{gap} or more fibroblasts, which can be attributed to the reduction in dV/dt_{max}. Moreover, because of the more positive resting membrane potential of coupled fibroblasts, the MDP (maximum diastolic potential in the SAN) and RMP (resting membrane potential in the atrium) of the corresponding myocyte are also elevated after coupling with a larger G_{gap} or more fibroblasts. As a result, the APA is decreased to different degrees in the CSAN, PSAN, and atrium. This result agrees with the *in vivo* experiments conducted by Ursell et al. [33] and Davis et al. [58].

Both CL and APD_{90} are shortened in the CSAN model after coupling with larger G_{gap} or more fibroblast under weak coupling because of the elevation of the RMP. The gap current flowing from the fibroblast to the coupled myocyte is able to decelerate the repolarisation of myocyte and therefore results in a larger CL during the discharging process. The significant decrease in APA can also lead to a remarkable reduction in CL, which is more significant in comparison to the increase in CL resulting from the current flowing from the fibroblast. As a result, the CL and APD_{90} are shortened, suggesting a faster pacemaking rate in the CSAN.

In the PSAN model, the charging process of the fibroblast is very slow under weak coupling, which takes a large portion of repolarisation phase. The discharge process does not start until the very end of the repolarisation. With the increase of G_{gap}, the early repolarisation rate is accelerated as the greater current flows to charge the coupled fibroblast, therefore the APD_{90} is shortened, however, the late repolarisation rate becomes slower because of the greater current flow from the fibroblast (discharge process), and therefore the CL is prolonged. In strong coupling case, the charging process of the fibroblast is accelerated, which finishes at the early repolarisation. After increasing the G_{gap}, the repolarisation rate is slowed down, both CL and APD_{90} are prolonged, suggesting a slower pacemaking rate. This may explain the reduction in heart rate in the SAN found in ageing and diseased hearts [59], [60].

In the atrium model, with the increase in G_{gap}, the APD_{90} decreases and is then followed by an increase, which means that the charging process becomes faster with the increase in G_{gap}. The reduction in APD_{50} means that the discharging process does not start until the myocyte is repolarised by 50%.

Our simulation in M-F-M connection suggests that the AP can be propagated to the next myocyte when G_{gap} is in the range of 6 - 30 nS, which is smaller than the G_{gap} used in Sachse et al.'s simulation (50 - 100 nS) [61]. The possible explanation is that the rat ventricular myocyte model they used and some currents they incorporated in the fibroblast model was from rat kidney. In the M-nF-M model, with the increase in the coupling number, the delay in the activation time of the second myocyte is increased. When the coupling fibroblast number is 2, the conduction delay is 6.4 ms in our simulation, which is smaller in comparison to the results in *in vitro* experiments [27]. The conduction block does not show until the coupling fibroblast number fibroblast is more than 6, which is less than reported in the co-cultured experiment [62]. This may be because the cells they used in their experiment were from the rat ventricle, while our myocyte model was developed based on experimental data for cells in the rabbit atrium.

Chapter 4. The Myocyte-Fibroblast Coupling in Tissue Models

4.1 Introduction

Featuring the proliferation of fibroblasts and the deposition of extracellular matrix proteins (ECM), cardiac fibrosis usually occurs in an injured heart region as a response to structural remodelling. It typically contributes to cardiac conduction abnormalities and mechanical dysfunctions and therefore leads to many pathophysiological conditions, such as hypertrophy, failure, and arrhythmias, etc. [63]. Some *in vitro* experiments have demonstrated that fibroblasts can modulate the signalling pathways in tissue both directly and indirectly [18], [64], [65]. For example, it can cause a conduction delay or even interrupt the action potential (AP) propagation by working as an electrical load of myocytes or mechanically separating myocyte connections [66]. Some other clinical recordings and *in vitro* experiments reported that fibroblasts can act as a conductor propagating AP from one myocyte to another, which may improve the electrical communications between myocytes in infarcted myocardial tissue and therefore play an active role in reducing conduction disorders [26], [27], [67].

Some tissue-level computation models also have been developed in healthy and diseased heart to explore the role that fibroblasts play in cardiac conduction. Jacquement et al. developed a 2D rectangular sheet of canine atrial myocytes and investigated the coupling effects on AP propagation in the tissue with fibroblasts attached on the top and randomly inserted in the tissue, respectively. They found that either improving or delaying the AP propagation mostly depends on the coupling type and coupling strength [68], [69]. However, homogeneous coupling between fibroblasts and zero-sided connection were not considered in their simulation.

Clancy et al. investigated the effect of fibroblasts on SAN activity by coupling fibroblasts to the SAN tissue model incorporating the Oxsoft model and the Kurata rabbit SAN model. As their results suggested, fibroblasts worked as an electrical sink and could prolong the conduction time [70]. However, the fibroblast model they used was the passive model; they did not consider the active and independent ion currents in fibroblasts. Moreover, although they considered the double-sided connection and zero-sided connection, they did not consider single-sided connection.

Zlochiver et al.[71], [72] developed a 2D model of ventricular myocytes to simulate the coupling effect on re-entrant arrhythmias according to their previous co-cultured experiment. They suggested that the conduction velocity was first increased and then decreased with the increasing heterocellular coupling. To examine the effects of the coupling ratio on electrical spiral wave conduction during re-entrant activity, they incorporated MacCannel's fibroblast model and the Tusscher model in their later simulation and found that the spiral-wave velocity and re-entrant lifespan depends on the coupling strength and number of coupling fibroblasts. After coupling with more fibroblasts, the conduction velocity was increased under weak coupling, but decreased under strong coupling.

Although some investigations of coupling effects on AP conduction in cardiac tissue have been conducted both *in vitro* and *in silico*, the roles that fibroblasts may play in cardiac conduction is still controversial. Moreover, fibroblast–myocyte coupling has not been studied in the realistic cardiac tissue model with the pacemaker incorporated.

Therefore, in our study, a SAN-atrium tissue model of a rabbit SAN and right atrium was developed to study the AP initiation and propagation with fibroblasts coupled in different ways. Three different fibroblast–myocyte configurations, the zero-sided connection (decoupling model), the single-sided connection (attachment model), and double-sided connection (insertion model), were considered. The coupling effects on the AP waveform, pacemaking cycle length (CL), conduction velocity (CV), activation time (AT), and maximum upstroke velocity (dV/dt_{max}) in the three models will be introduced in the following sections.

4.2 Method

4.2.1 2D Tissue Model

The SAN-atrium tissue model was adopted from Butter et al.'s paper [46]; the anatomical geometry was reconstructed from a single slice of rabbit right atrium cut through the atrial muscle of the crista terminalis (CT) and the intercaval region. The spatial resolution of the geometry was set to 210×45 nodes in a Cartesian grid, with $40\,\mu m$ for each cell corresponding to 2-4 diameters of a single cardiac myocyte according to the immunohistochemistry mapping data [73]. The geometry incorporated the central and peripheral SAN, atrial muscle and septum, and the block zone [8], [73] between the central and peripheral SAN next to the atrial septum. Each

cell in the tissue was labelled with a flag variable to distinguish the cells from different areas. The Zhang et al. equations for the SAN cell model [44] and the Aslanidi et al. equations [56] for the right atrium were used to describe the electrical activities of the cells in the different areas of the tissue.

The initiation and propagation of APs in the myocardial tissue can be formulated by

$$\frac{\partial V}{\partial t} = \nabla \cdot (\mathbf{D} \nabla V) - \frac{I_{ion}}{C_m}, \tag{4.1}$$

where V is the membrane potential of myocyte, t is the time, ∇ is the spatial gradient operator, and $\mathbf{D}$ is a tensor of diffusion coefficient, C_m is the membrane capacitance, and I_{ion} is the total ionic current.

As indicated by the histological experiment, the cell-to-cell gap junction coupling varies in the SAN centre, periphery, and atrium; the density of gap junction shows an increase from the central SAN to the peripheral SAN. Thus, considering the regional differences in the tissue, a spatial gradient of diffusion coefficient, D was introduced, as shown in Figure 4.1F and generated by Equation 4.2:

$$D(x) = D_c + D_p \left(\frac{1.0}{1.0 + e^{-0.5(x - x_1)}} + \frac{1.0}{1.0 + e^{0.5(x - x_2)}} \right), \tag{4.2}$$

where x is the horizontal coordinate through the 2D slice, x_1 and x_2 present the approximate positions of the SAN boundaries, the D_c and D_p represent the diffusion coefficients of cells in the SAN centre and SAN periphery, respectively.

A spatial gradient of C_m was also induced in the SAN region, because of the different electrophysiological properties between the SAN centre and periphery. As the cell size in the SAN periphery was presumed to be larger than in the SAN centre [7], [44], [74], in our model, the C_m was regulated by Equation 4.3 and was smaller in the SAN centre and larger in the SAN periphery:

$$C_m(x) = C_m^c + C_m^p \left(\frac{1.0}{1.0 + e^{-0.1(x - x_1)}} + \frac{1.0}{1.0 + e^{0.1(x - x_2)}} \right), \tag{4.3}$$

where C_m^c and C_m^p are the capacitances of cells in the SAN centre and SAN periphery. Spatial variations in ion channel conductance were defined as a function of C_m.

$$g_z(x) = \frac{C_m(x) - C_m^c}{C_m^p - C_m^c} g_Z^c + \frac{C_m^p - C_m(x)}{C_m^p - C_m^c} g_Z^p, \tag{4.4}$$

where $g_z(x)$ is the conductance of the ion channel for a particular ionic current, Z represents the different ionic current, and g_Z^c and g_Z^p are the conductances of the cells in the SAN centre and periphery, respectively.

As the block zone was also included in our geometry, owing to the low excitability of the cell in the block zone, I_{tot} for the cell in block zone was governed by Equation 4.5:

$$I_{tot} \equiv I_B = G_m(V - V_R), \tag{4.5}$$

where I_B is the passive membrane current of block zone cells, G_m is the membrane conductance, and V_R is the resting membrane potential. In our model, G_m and V_R are assumed to have the same values of neighbouring SAN and atrial cells. Equation 4.2-4.5 are taken from [46].

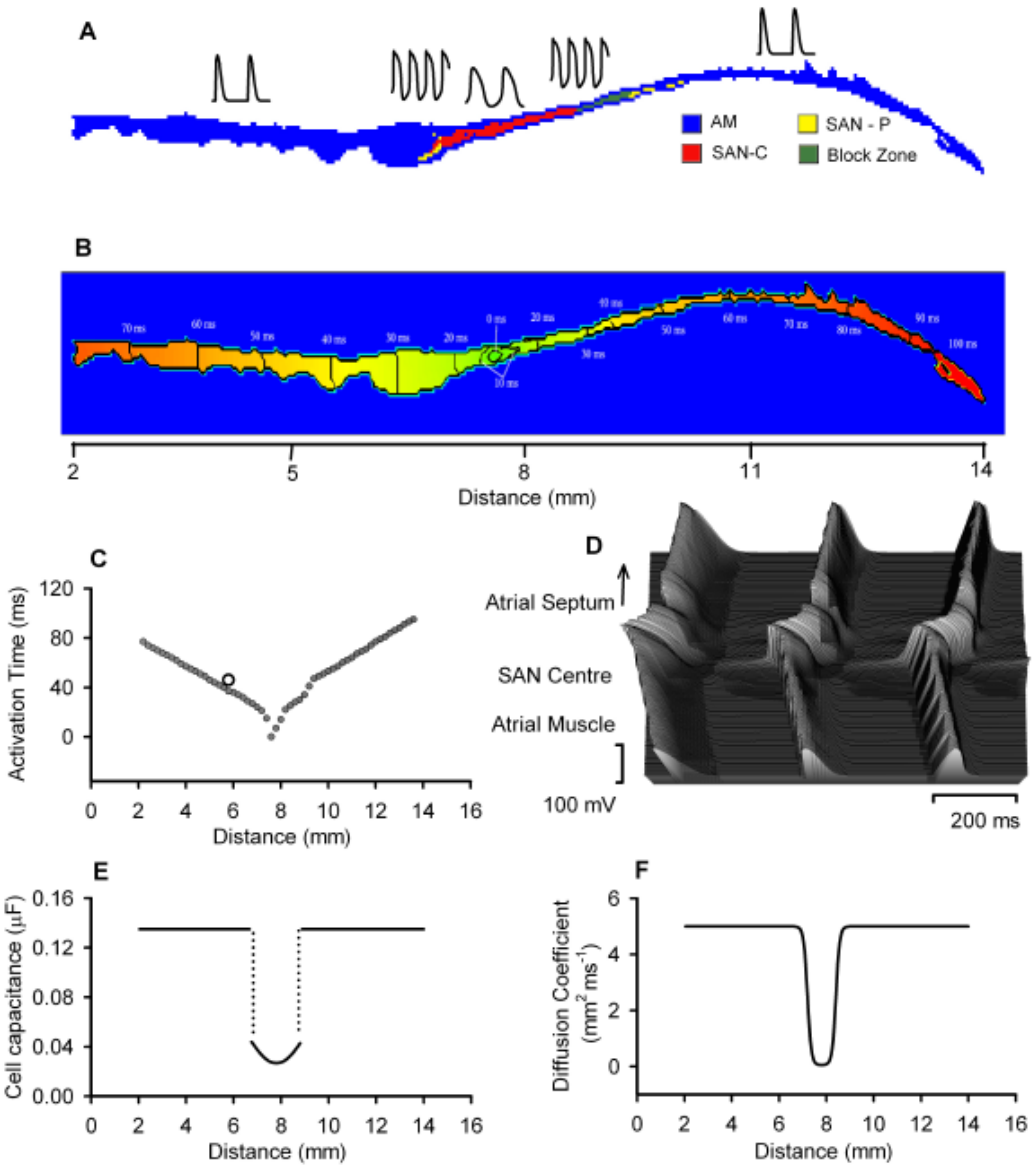

Figure 4.1 2D tissue model of the rabbit SAN with atrial tissue. (A) Cell distribution and AP waveform of each cell type. (B) Activation time sequence during normal AP conduction, (C) AT of the cells in the middle of the 2D slice. (D) AP profiles recorded from the cells in the middle of the 2D slice. (E) Gradient in cell capacitance along the slice. (F) Gradient in the diffusion coefficient along the slice. Figure taken from [75].

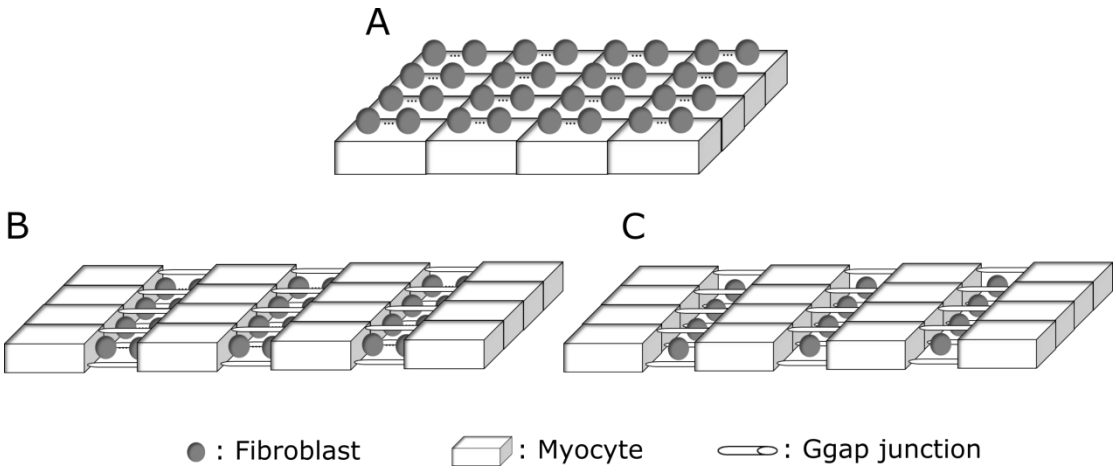

Figure 4.2 Schematic diagrams of the coupling regions in the SAN-atrium tissue. Three different fibroblast–myocyte arrangements were applied: The (A) attachment model, (B) insertion model, and (C) decoupling model.

4.2.2 Fibroblast Model

MacCannell et al.'s active fibroblast model [51] was used in our 2D simulation (the same as in the cellular simulation; see section 3.24).

4.2.3 Myocyte–Fibroblast Coupling Model

In our tissue models, three conceptual configurations of fibroblasts and myocytes were considered based on the experimental observations *in vivo* [76], namely single-sided connection, the double-sided connection, and zero-sided connection (Figure 1.9).

Attachment model: As shown in Figure 4.2A, corresponding to the single-sided connection, a fibroblast was directly attached to a myocyte, working as a current sink. In this case, a fibroblast can heterogeneously couple to a myocyte via gap junctions but has no intercellular coupling with other fibroblasts. Two scenarios were studied to explore the effects of fibroblasts on the pacemaking activity in the SAN and AP propagation in the atrial muscle: (1) a varying number of fibroblasts were simply attached to the myocyte in the central and peripheral SAN (FASN model) and (2) a varying number of fibroblasts were attached to the myocyte in the whole tissue (FAT model). The gap junction conductance (G_{gap}) between myocyte and fibroblast was set to 1 ns, 3ns, 6ns, and 9ns, and a coupling fibroblast number of 1, 3, 5, and 9 was selected for each fixed G_{gap}.

Decoupling model: As shown in Figure 4.2C, the decoupling arrangement is presumed to be the most common type of the existence of fibroblasts in the

myocardium. In this case, the fibroblast acts as an electrical insulator and is not electrically connected to either the adjacent fibroblasts or myocytes, resulting in a decrease in the density of the gap junction coupling between the myocytes. In our decoupling model, a strand of electrically isolated fibroblasts was inserted to reduce gap junctions in the myocyte–myocyte connections in the lateral direction. As the AP propagation through gap junctions is characterised by the diffusion coefficient D, the decrease in gap junction coupling can be simulated by reducing the value of the diffusion coefficient. The transverse diffusion coefficient of the voltage was assumed to be reduced by 50% when decoupled fibroblasts were evenly inserted in the tissue.

Insertion model: According to *in vitro* experiments, fibroblasts can act as conductors to electrically link two myocytes and pass an AP between the myocytes (double-sided connection). Therefore, a number of fibroblasts were inserted in myocyte–myocyte connections (fibroblast number = 1, 5, and 9) in the lateral direction to simulate AP propagation in this case (Figure 4.2B). Because of the insertion of fibroblasts, the gap junctions in myocyte–myocyte connections are reduced, so we reduced the diffusion coefficient by 50% to simulate the reduction in coupling between myocytes after inserting fibroblasts in the tissue. The G_{gap} in fibroblast–fibroblast coupling and fibroblast–myocyte coupling was assumed to be the same in our model (G_{gap} of 1, 5, and 15 nS was selected). Similar to the attachment model, two scenarios were studied to explore the effects of fibroblasts on the pacemaking activity in the SAN and AP propagation in the atrial muscle: (1) a fibroblast was simply inserted in the SAN (FISN model), and (2) a fibroblast was inserted in the whole tissue (FIT model).

4.3 Results

4.3.1 Effects of Coupling Strength on AP Initiation and Propagation in the Attachment Model

The coupling effects of G_{gap} on the AP initiation in the pacemaker and the propagation in the atrium were investigated in the 2D mathematical model. Figure 4.3 shows time-space plots of AP profiles recorded in a line of cells (selected from the middle of the 2D slice) across the tissue under different coupling conditions. As shown in Figure 4.3A and B, when no fibroblast is coupled to the myocytes, the AP is initiated in the SAN centre and then propagated to the atrial muscle and the atrial septum with a CL of 342.4 ms. Despite the less depolarised PA in the block zone between the SAN centre

and atrial septum, the AP propagation is not disrupted in the direction towards the atrial septum. Figure 4.3C and D illustrate the changes in AP profiles when each myocyte couples with three fibroblasts with a G_{gap} of 1 nS in the SAN (FASN model) and whole tissue (FAT model), respectively. The CL is prolonged by 1.9% in the FASN model and 2.1% in the FAT model compared to the results in control conditions, suggesting a slower heart rate. The AP profiles for a larger coupling G_{gap} of 5 nS and 9 nS in the FASN model are shown in Figure 4.3E and G. The results indicate that the CL change is very small after coupling with different G_{gap} in the FASN: 349.05 ms (G_{gap} = 5 nS) and 349.94 ms (G_{gap} = 9 nS) compared to 248.99 ms with a G_{gap} of 1 nS. A slight conduction delay in the SAN can be observed as G_{gap} is increased. In the FAT model, after the G_{gap} is increased from 1 nS to 9 nS, the CL does not show significant changes, while the conduction delay becomes more significant in the FAT model than in the FASN model.

The changes in the AT, CV, and dV/dt_{max} of the selected cells across the centre of the 2D tissue slice are also presented in Figure 4.4. The grey shaded region as marked in the SAN towards the atrial septum corresponds to the block zone, where the AT shows a delay and the CV and the dV/dt_{max} are smaller than those in the adjacent regions. As shown in Figure 4.4, the changes in AT, CV, and dV/dt_{max} are greater in the region from the SAN towards the atrial septum. The tissue in this region is thin and contains more pacemaker cells. According to Figure 4.4A and B, the AT in both the FASN model and the FAT model are prolonged after coupling with fibroblasts compared to the results in control conditions. Moreover, the prolongations in AT are highly dependent on G_{gap}, which becomes larger as G_{gap} is increased. As shown in Figure 4.4C, the CV slows down in the SAN after coupling with fibroblasts and drops to a lower level when G_{gap} becomes larger. For example, it is decreased by ~8.8% and ~11.9% on average in the SAN when the coupling G_{gap} increases to 5 nS and 9 nS from 1 nS in the FASN model. In the FAT model (Figure 4.4D), the reductions in CV occur not only in the SAN but also in the atrium; they are smaller in the SAN (~19.0% for G_{gap} = 5 nS and ~23.9% for G_{gap} = 9 nS) and larger in the atrium (~15.1% for G_{gap} = 5 nS and ~21.4% for G_{gap} = 9 nS). The decreases in CV can be attributed to the decline in dV/dt_{max}, as illustrated in Figure 4.4E and F. A reduction in dV/dt_{max} is shown in the SAN in the FASN model after coupling with fibroblasts and becomes

greater after G_{gap} is increased. Moreover, a decrease in dV/dt_{max} in the atrium can also be observed in the FAT model after coupling.

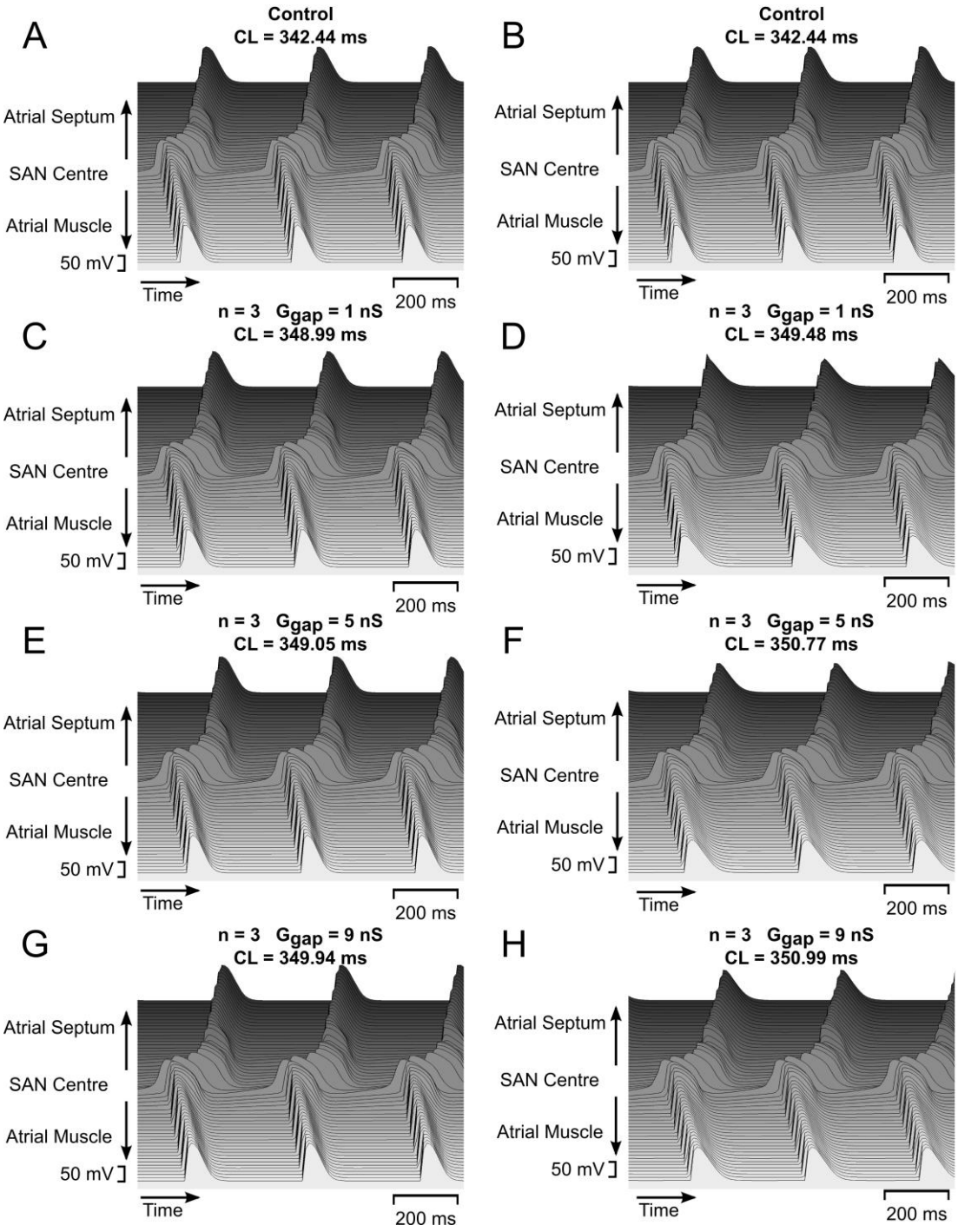

Figure 4.3 Effects of G_{gap} on the AP initiation and propagation in the attachment model as a function of time. AP profiles in the 2D tissue under control conditions and with each myocyte coupled with three fibroblasts (G_{gap} =1, 5, 9 nS) in the SAN (left, A, C, E, G) and in whole tissue (right, B, D, F, H).

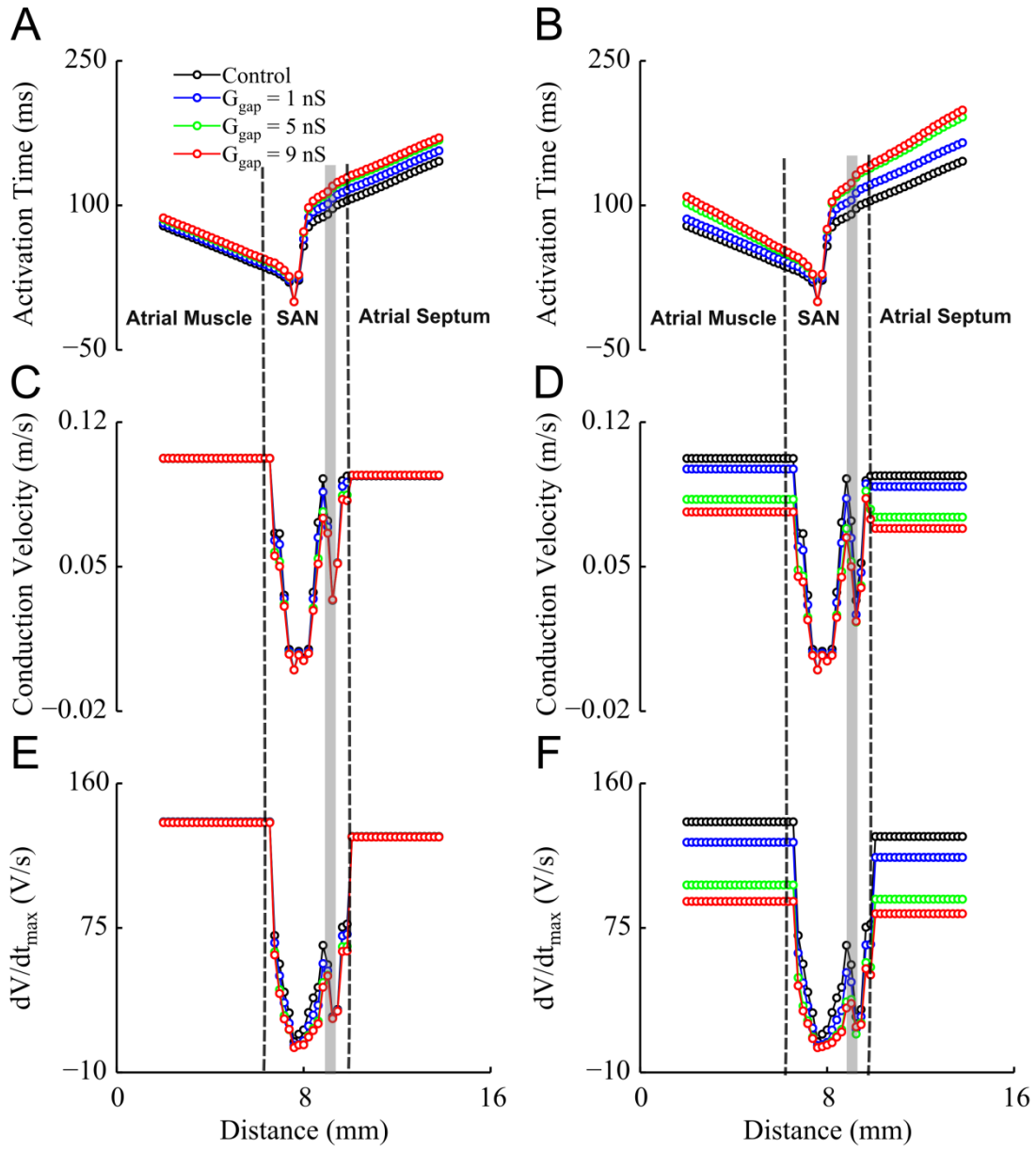

Figure 4.4 Effects of G_{gap} on the AP conduction parameters in the attachment model as a function of distance. The AT, CV, and dV/dt_{max} in the FASN model (A, C, E) and in the FAT model (B, D, F) under control conditions and coupling to three fibroblasts with a G_{gap} of 1 nS, 5 nS, and 9 nS.

4.3.2 Effects of Coupling Fibroblast Number on AP Initiation and Propagation in the Attachment Model

The effects of the coupling fibroblast number on the AP initiation in pacemaker cells and propagation in the atrium were also investigated by coupling a varying number of fibroblasts (n = 0, 1, 4, and 7) with a G_{gap} of 3 nS. As shown in Figure 4.5C, E, and G, after the coupling fibroblast number is increased from 1 to 4 and 7, the CL in the FASN

model is prolonged by 2.8% and 5.9%, suggesting a slower pacemaking rate. A unidirectional conduction block shows from the SAN centre towards the atrial muscle when coupling fibroblast number is 7. Similar to in the FASN model, a prolonged CL (3.1%) shows when the coupling fibroblast number is increased from 1 to 4 in the FAT model. After coupling with 7 fibroblasts, the conduction is blocked in both direction and therefore atrial tissue is not able to be activated.

As shown in Figure 4.6A and B, the AT is increased along with the fibroblasts coupled in both FASN and FAT model. The activation delay in the atrium is larger in the FAT model compared to it in the FASN model under same coupling strength and number. Figure 4.6C and D shows the effects of coupling fibroblast number on CV in FASN and FAT model. The increased coupling fibroblast number results in a greater decrease in CV. For example, after coupling with 1 and 4 fibroblasts in the FASN model, the CV is decreased by ~ 4.5% and ~ 14.6% on average in the SAN, while a decrease of ~17.4% and ~23.8% shows in the SAN and a decrease of ~4.5% and ~18.5% is shown in the atrium in the FAT model. The reductions in dV/dt_{max} occurs in the area with coupled fibroblasts and it becomes lager after coupling with more fibroblasts (Figure 4.6E and F).

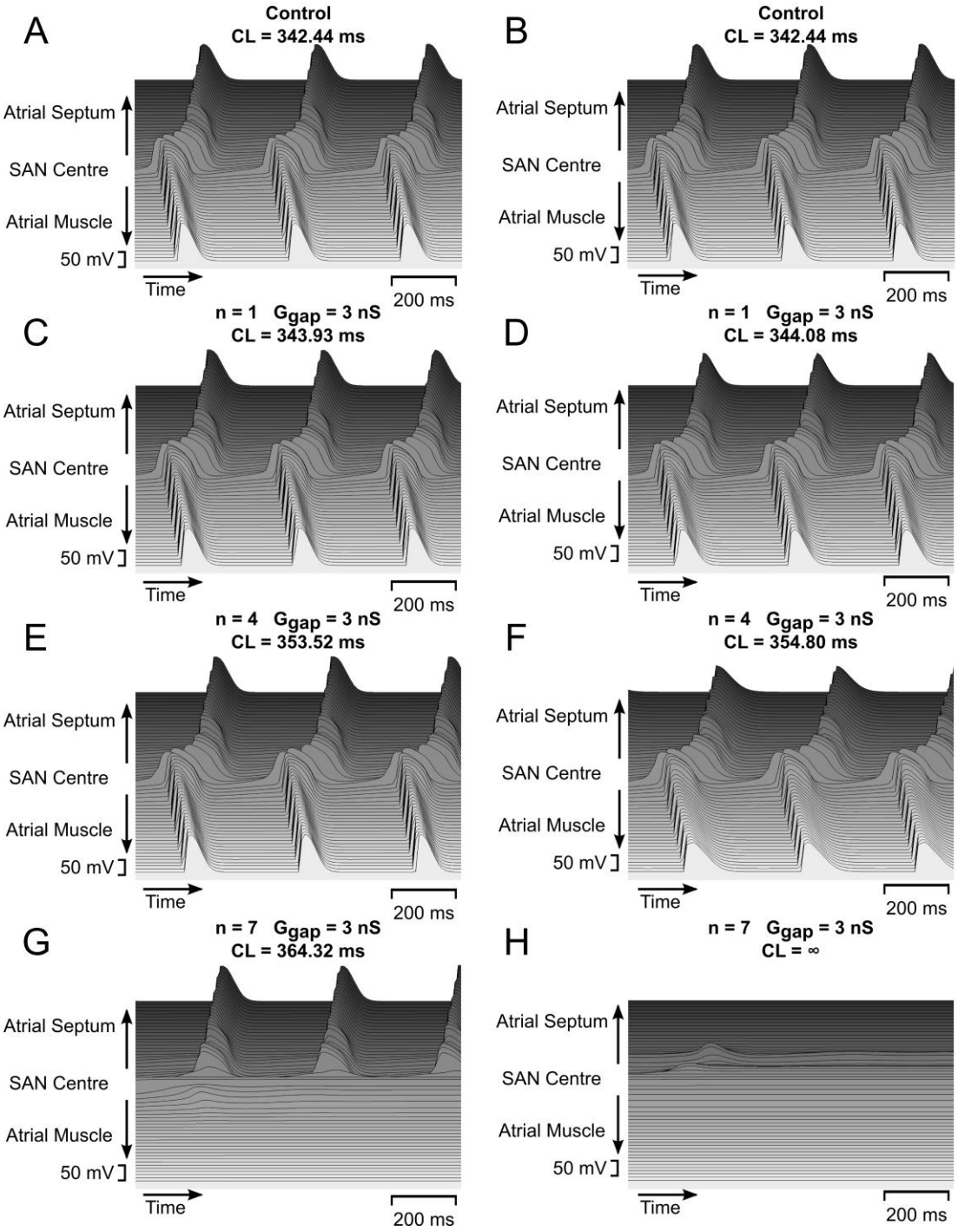

Figure 4.5 Effects of coupling fibroblast number on the AP initiation and propagation in the attachment model as a function of time. AP profiles in the 2D tissue under control conditions and with a varying number of fibroblasts (n = 1, 4, and 7) coupled to each myocyte with a G_{gap} of 3 nS in the SAN (left, A, C, E, G) and in whole tissue (right, B, D, F, H).

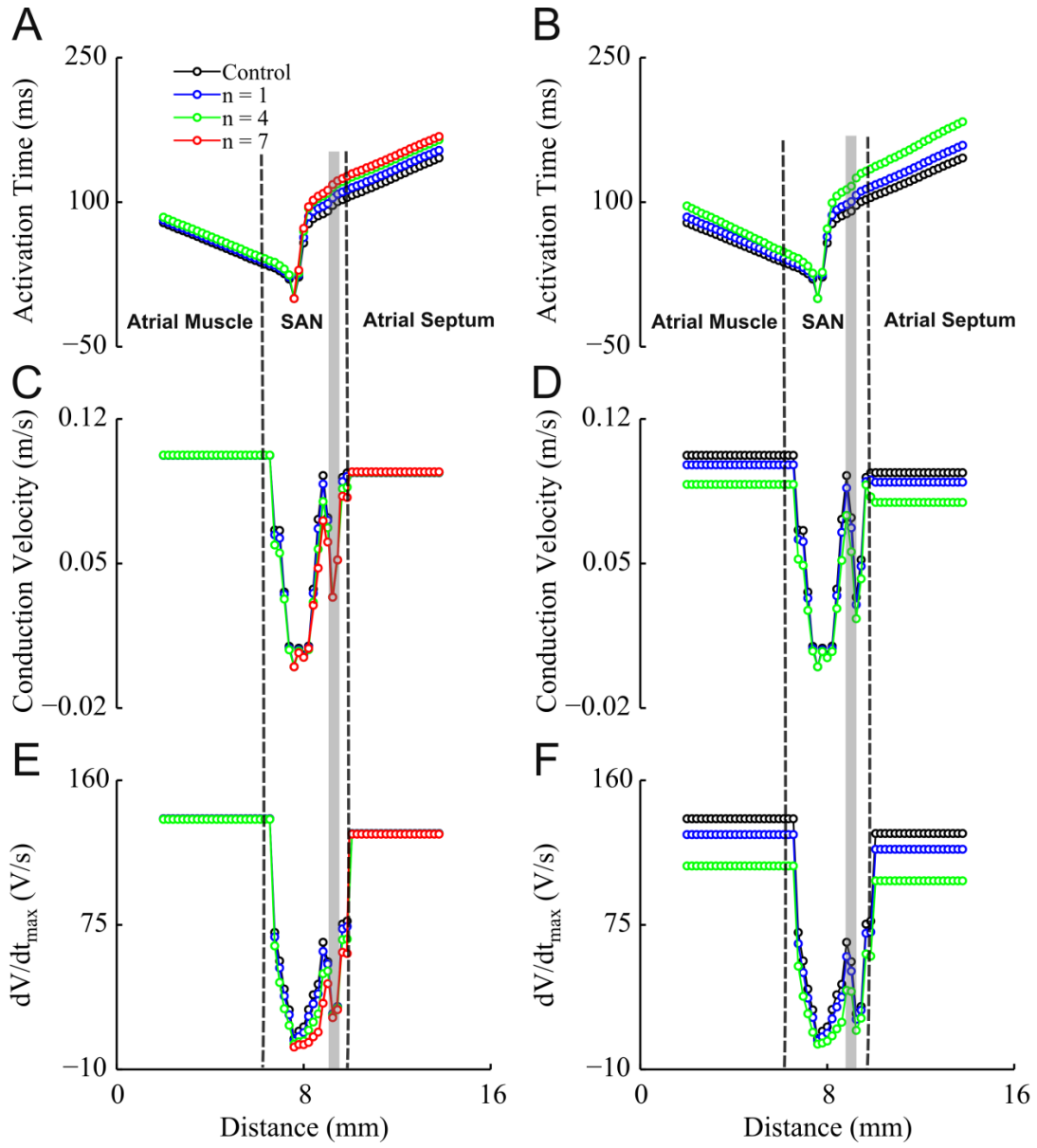

Figure 4.6 Effects of coupling fibroblast number on the AP conduction parameters in the attachment model as a function of distance. The AT, CV and dV/dt_{max} in the FASN model (A, C, E) and in the FAT model (B, D, F) under control conditions and coupling to a varying number of fibroblasts (n = 1, 4, and 7) with a G_{gap} of 3 nS.

4.3.3 Effects of Coupling Strength on AP Initiation and Propagation in the Insertion Model

The coupling effects of G_{gap} on the AP initiation in pacemaker cells and propagation in the atrium were also investigated in the insertion model. The decoupling case was also considered in this study. Figure 4.3 shows time-space plots of recorded AP profiles in the SAN and the atrium under different coupling conditions. The control

case is shown in Figure 4.7A and B. The decoupling case is shown in Figure 4.7C for the FISN model and Figure 4.7D for the FIT model. After the myocyte pairs are decoupled by the fibroblasts, a conduction delay can be observed in the SAN, and the CL also decreases from 342.4 ms to 337.1 ms in the FISN model, while in the FIT model, the conduction delay emerges both in the SAN and atrium; the CL is also decreased by 1.6%, which indicates a faster heart rate after decoupling. The insertion case is shown in Figure 4.7E and F, after myocytes are interconnected with one fibroblast with a G_{gap} of 5 nS; the conduction delay in the SAN is much smaller in the FISN model compared to the results in the decoupling case. The CL shows an increase from 337.12 ms (decoupling) to 348.26 ms (G_{gap} = 5 nS), which is even longer than in control conditions. This suggests that the pacemaking rate is increased. In FIT model, the decrease in the conduction delay can be observed in both the SAN and atrium. The prolongation in CL is larger than in the FISN model, increasing from 336.85 ms (decoupling) to 356.75 ms (G_{gap} = 5 nS). A significant decrease in the conduction delay in the SAN can be observed after the G_{gap} is increased to 15 nS (Figure 4.7G), suggesting faster AP propagation in the SAN in the FISN model. Meanwhile, the CL is prolonged by 3.3%, 4.9%, and 1.6% with respect to the control conditioning, under decoupling, and with a G_{gap} of 5 nS, respectively. When coupling with a G_{gap} of 15 nS, the conduction delay is decreased in both the SAN and atrium; the CL is prolonged from 342.4 ms to 377 ms, 11.9% and 5.7% larger than under decoupling and with a G_{gap} of 5 nS (Figure 4.7H). Though a conduction block occurs in the block zone, the AP can still be propagated to the atrial septum successfully from the peripheral SAN (between the atrial septum and the block zone).

As shown in Figure 4.8A, in the decoupling case, the AT of the myocytes in both the SAN and atrium is prolonged compared to the results in control conditions. After interconnecting myocytes with fibroblasts and increasing the coupling G_{gap} from 0 to 1 nS and 15 nS, the AT shows significant decreases both in the SAN and atrium. In the FIT model (Figure 4.8B), the AT in the atrium is much longer than in the FISN model in the decoupling case. Moreover, after increasing the G_{gap} to 5 nS, the AT in the SAN is decreased and shorter than in control conditions, while the AT in the atrium shows a reduction, but it is still larger than in control conditions.

Figure 4.8C shows the changes in the CV after decoupling and coupling in the FISN model. The CV in the SAN is decreased in the decoupling case, but increases in the

CSAN and decreases in the PSAN after connecting the separate myocytes with fibroblasts. The changes become greater with a larger G_{gap}. For example, an increase of ~15.4% and ~21.5% is shown in the CSAN and a decrease of ~6.3% and ~7.2% in the PSAN after coupling with a G_{gap} of 5 and 15 nS, respectively. Figure 4.8D shows the CV changes in the FIT model; in the decoupling case, a reduction in CV is shown in both the SAN (~14.9%) and atrium (~17.5%). After the G_{gap} is increased from 5 nS to 15 nS in the coupling case, the CV decreases by ~1.2% on average in the PSAN and increases by ~8.2% and ~1.8% in the CSAN and atrium, respectively.

The dV/dt_{max} in the FISN and FIT models is shown in Figure 4.8E and F. The effects of decoupling on dV/dt_{max} are relatively small in the decoupled area in both models. In the coupling case, the dV/dt_{max} decreases along with the increase in G_{gap}, falling almost to 0 in the block zone in the FIT model when G_{gap} is increased to 15 nS, indicating a conduction block in the block zone.

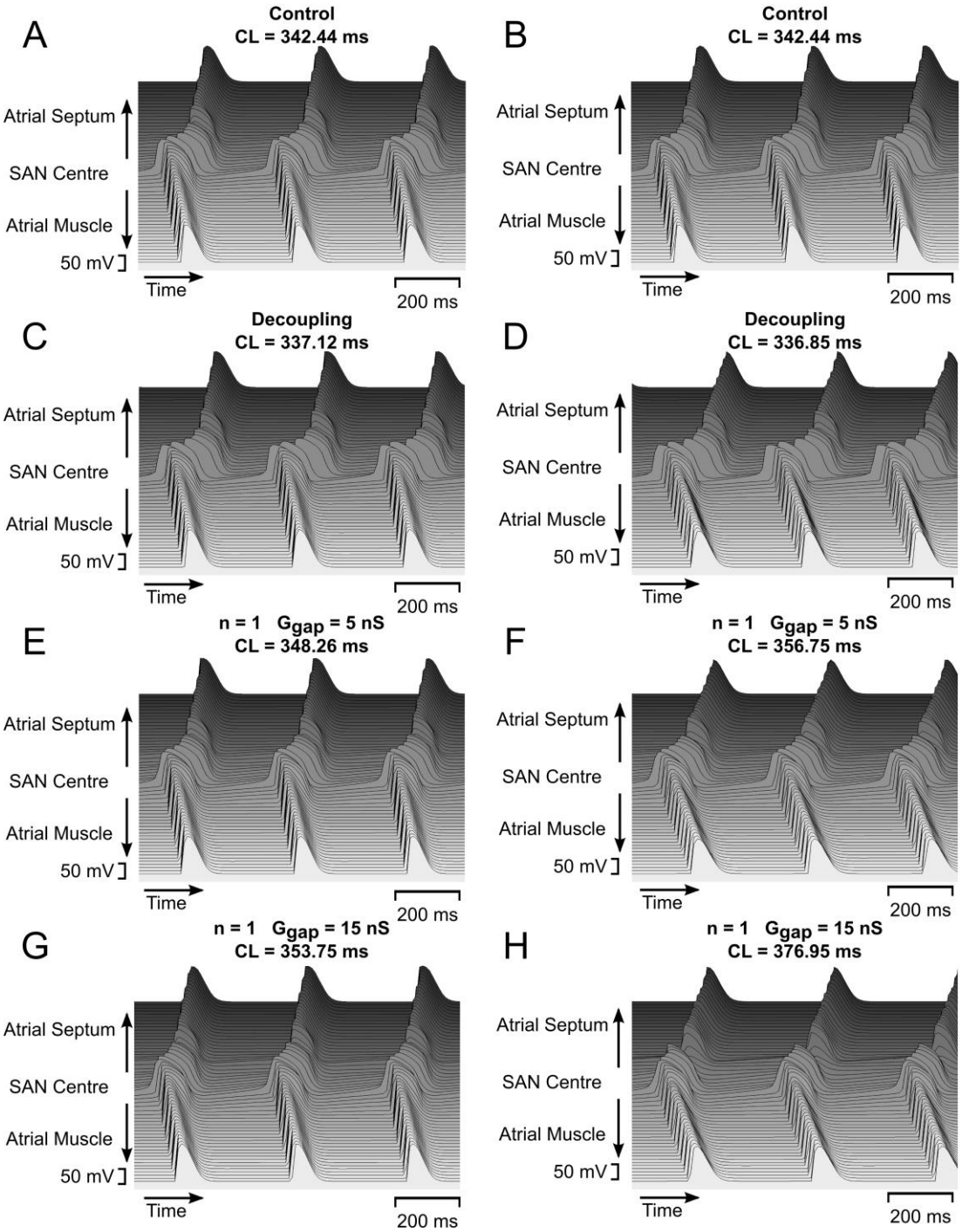

Figure 4.7 Effects of G_{gap} on the AP initiation and propagation in the insertion model as a function of time. AP profiles in the 2D tissue under control conditions and with a fibroblast inserted between myocytes (coupling G_{gap} of 0, 5, and 15 nS was selected) in the SAN (left, A, C, E, G) and in whole tissue (right, B, D, F, H).

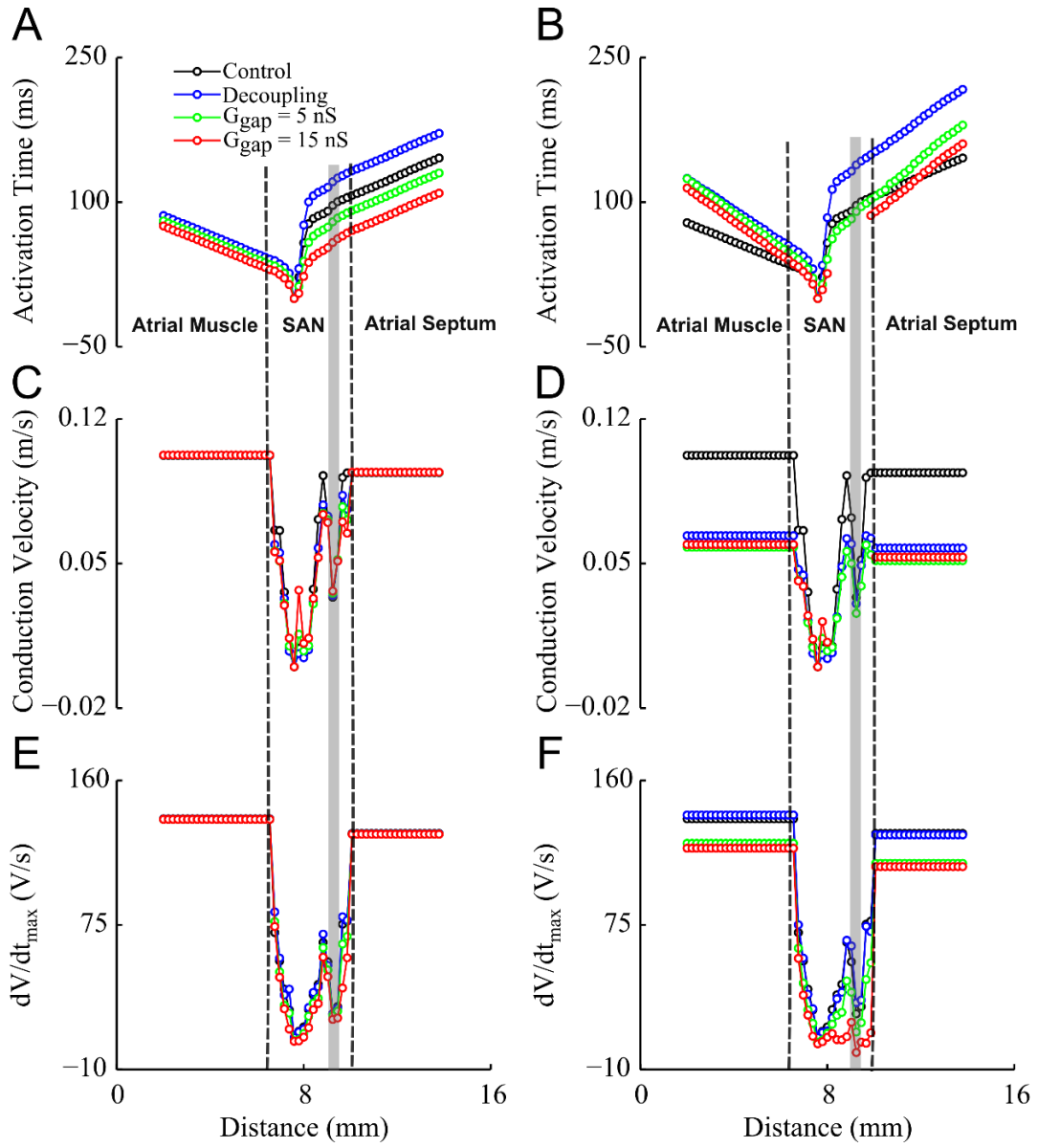

Figure 4.8 Effects of G_{gap} on the AP conduction parameters in the insertion model as a function of distance. The AT, CV, and dV/dt_{max} in the FISN model (A, C, E) and in the FIT model (B, D, F) under control conditions and with a fibroblast inserted in between the myocytes.

4.3.4 Effects of Coupling Fibroblast Number on the AP Initiation and Propagation in the Insertion Model.

The coupling effects of coupled fibroblast number on the AP initiation and propagation were also investigated in the insertion model, in which a coupling G_{gap} of 15 nS was selected. The control case and decoupling case are shown in Figure 4.9A–D. In the coupling cases, as shown in Figure 4.9E and F in the FISN model, the CL is increased

from 353.8 ms to 358.6 ms compared to 342.4 ms in control conditions, which suggests that the increasing coupling fibroblast number can result in a slower pacemaking rate. The conduction delay in the SAN becomes greater in the SAN after coupling with more fibroblasts. The CL is shortened from 377 ms to 372.2 ms after the coupling fibroblast number is increased from 1 to 5 in the FIT model (Figure 4.9G and H). Meanwhile, the conduction delay becomes smaller in the SAN and a conduction block occurs in the block zone when the coupling fibroblast number is 1 and in both the block zone and the atrial septum when the coupling fibroblast number is increased to 5.

After the coupling fibroblast number is increased from 1 to 5, the AT is prolonged in the SAN but is still shorter than in the decoupling case in the FISN model (Figure 4.10A). In the FIT model (Figure 4.10B), the AT is increased in both the SAN and atrial muscle, but cells in the block zone and atrial septum are not activated because of the conduction block.

Figure 4.10C shows the coupling effects on CV in the FISN models; with the increase in coupling fibroblast number from 1 to 5, the conduction is slowed down in the SAN and the CV decreases by ~38.5% on average. In the FIT model, as shows in Figure 4.10D, the CV is decreased by ~42.3% in atrial muscle and ~68.2 % in the SAN towards atrial muscle. There is a conduction block in the SAN towards the atrial septum and in almost all the atrial septum when the coupling fibroblast number is increased to 5. Figure 4.10E and F shows the changes in dV/dt_{max} in both models. With the increase in the coupling number, the dV/dt_{max} is decreased in coupled areas in both models.

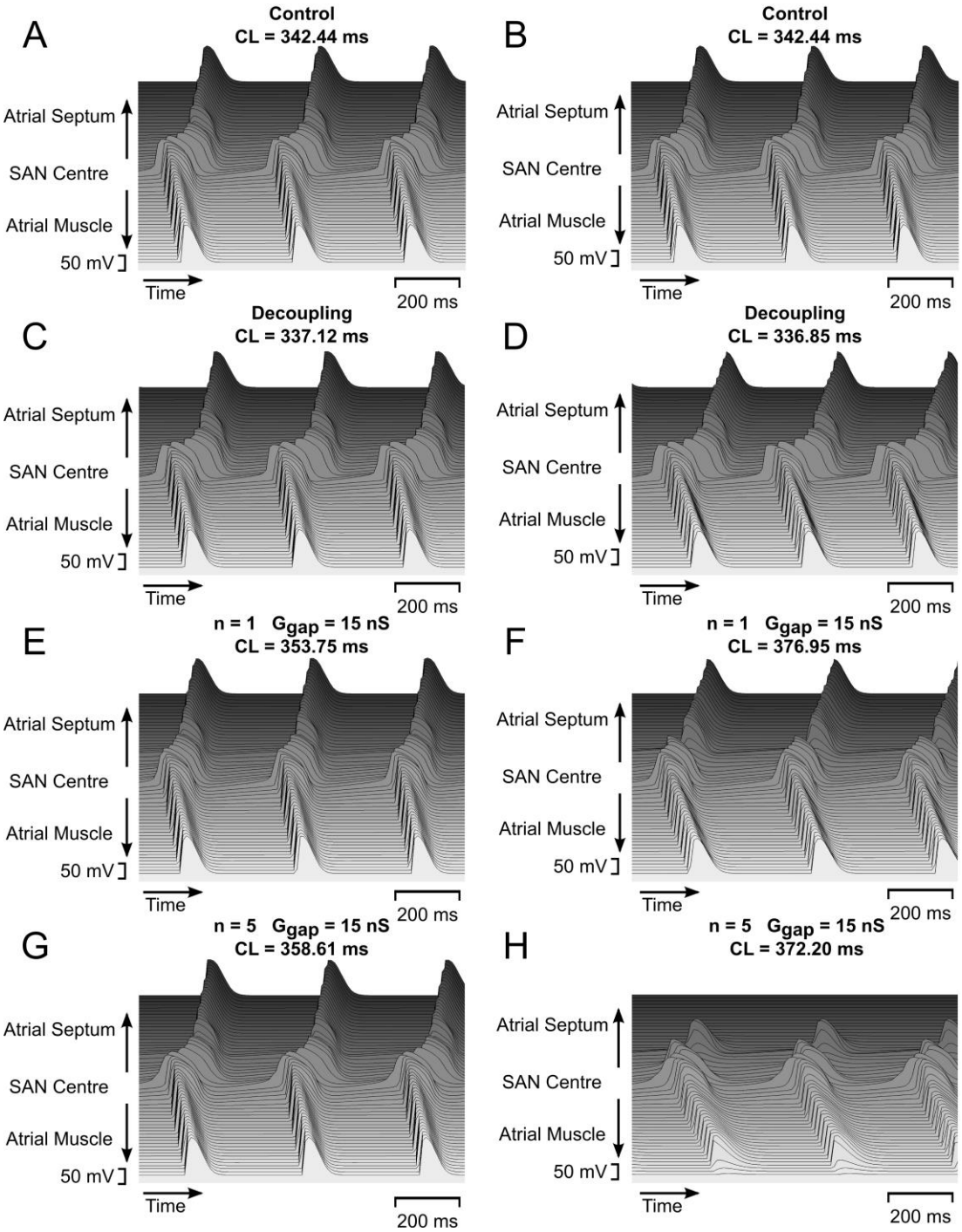

Figure 4.9 Effects of coupling fibroblast number on the AP initiation and propagation in the insertion model as a function of time. AP profiles in the 2D tissue in control (A, B) and under decoupling (C, D) as well as with a varying number of fibroblasts (1 and 5) inserted between myocytes in the SAN (E, G) and in whole tissue (F, H) are shown.

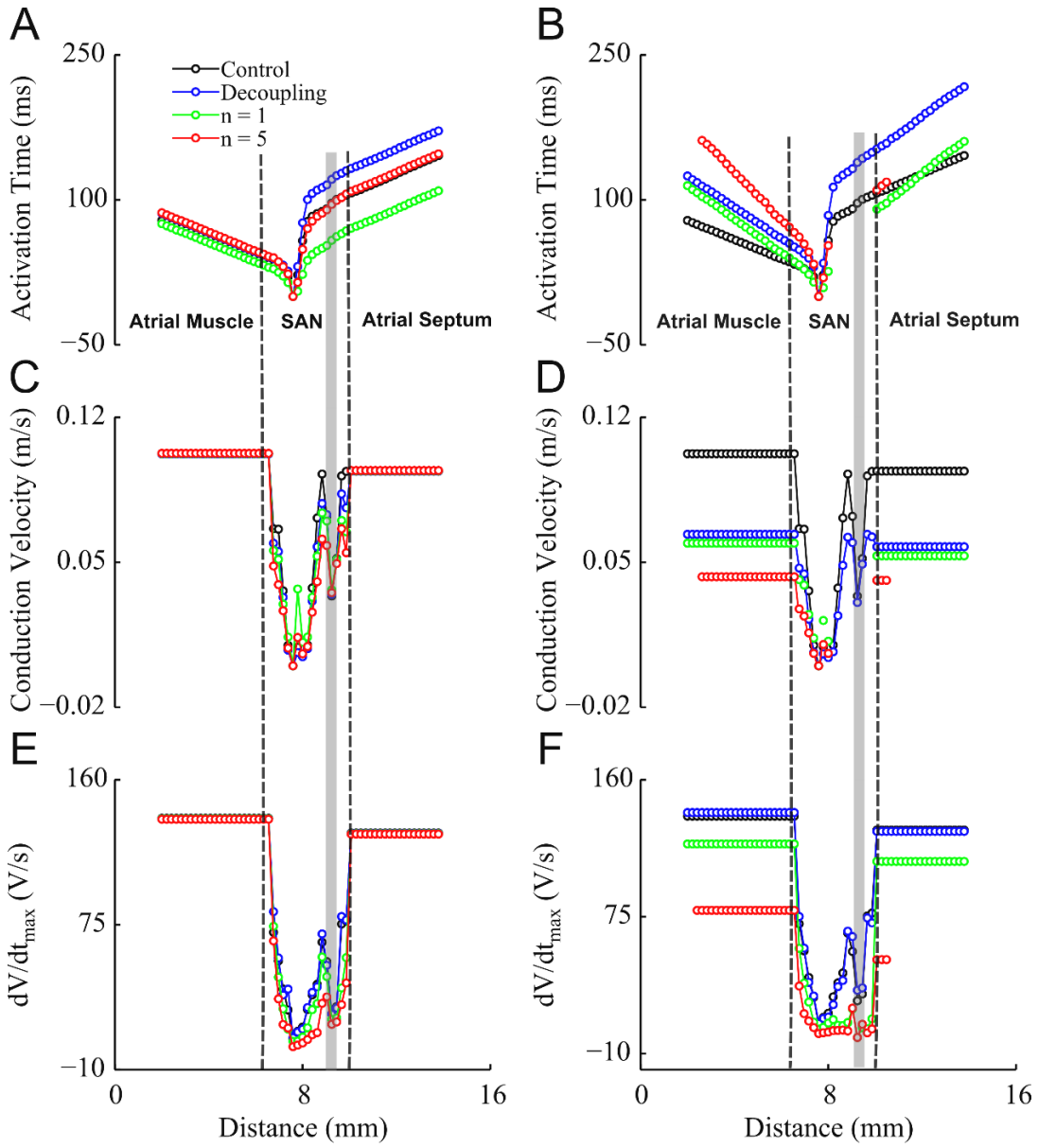

Figure 4.10 Effects of coupling fibroblast number on the AP conduction parameters in the insertion model as a function of distance. The AT, CV, and dV/dt_{max} in the FISN model (A, C, E) and in the FIT model (B, D, F) under control conditions and with a fibroblast interconnecting the myocytes.

4.4 Summaries and Discussions

In the current study, the coupling effects of G_{gap} and coupling fibroblast number on the AP initiation and propagation are studied in the attachment and insertion models. The main findings are shown in Table 4.1.

		Increase in G_{gap}	Increase in coupling fibroblast number
CL	FASN	↑	↑
	FAT	↑	↑
	FISN	↑	↑
	FIT	↑	↑↓
AT	FASN	↑	↑
	FAT	↑	↑
	FISN	↓	↓
	FIT	↓	↓↑
CV	FASN	↓ in CSAN	↓ in CSAN
	FAT	↓	↓
	FISN	↑in CSAN, ↓PSAN	↓
	FIT	↑ in CSAN, ↓ in PSAN, ↓ in the atrium	↓
dV/dt_{max}	FASN	↓ in CSAN	↓ in CSAN
	FAT	↓	↓
	FISN	↓ in CSAN	↓ in CSAN
	FIT	↓	↓

Table 4.1 Effects of coupling fibroblast number and G_{gap} on the AP initiation in the SAN and propagation in the atrium. ↑ represents an increase, ↓ represents a decrease, ↓↑ represents a decrease followed by an increase, and ↑↓ represents an increase followed decrease. CSAN is the SAN centre, PSAN is the SAN periphery, and N is the coupling number.

In the FASN model, after coupling with a larger G_{gap} or coupling number, the CL is prolonged; the dV/dt_{max} is decreased; the AT is increased; and the CV in the SAN is slowed down. This result is consistent with our cellular simulation. The G_{gap} in the FASN model is set from 1 - 9 nS, which corresponds to the strong coupling in the cellular simulation. Therefore, the CL in the PSAN is prolonged because of the slower repolarisation of myocytes after coupling with a larger G_{gap} or more fibroblasts. Moreover, the spontaneous activity in the CSAN is not abolished even under strong coupling in the tissue model, perhaps because of the strongly driven force from the surrounding PSAN cells. In the FAT model, the effects on the AP conduction are similar to those in the FASN model but become more significant because of the larger coupling areas. The CL is prolonged; the dV/dt_{max} is decreased; the AT is increased; and the CV is decreased in coupling regions after coupling with a larger G_{gap} or more fibroblasts.

While coupling with a single fibroblast in the attachment model, the conduction block does not occur even when the G_{gap} is increased to 9 nS. However, when G_{gap} is fixed at 3 nS, a block occurs in the SAN towards the atrial muscle direction in the FASN model and fully blocked in the FAT model after the coupling fibroblast number is increased to 7. This is because the SAN towards the atrial muscle contains fewer PSAN cells in comparison to the SAN towards the atrial septum. Therefore, a conduction block is more likely to occur in the SAN towards the atrial muscle after coupling with more fibroblasts. Our simulated results of the changes in the CV in the attachment model are consistent with Miragoli's experimental study on the impulse conduction in a strand of cardiomyocytes coated with myofibroblasts [27].

In the FIT model, while myocytes are interconnected with a fibroblast, the increasing G_{gap} can result in a larger CL, a shortened AT, a decreased dV/dt_{max} in the SAN and atrium, a faster CV in the CSAN, and a slower CV in the PSAN and atrium. A possible explanation for the diverse changes in CV in the SAN and atrium is that the coupling between myocytes in the CSAN is much weaker than in the periphery and atrium, so the electrical communications between the myocytes are actually enhanced after interconnecting the myocytes with a single fibroblast in the CSAN. More importantly, this improvement becomes more significant with a larger G_{gap}. As a result, the AP is propagated faster in the CSAN after increasing G_{gap}. In contrast, the coupling between myocytes is very strong in the PSAN and atrium; the AP has a faster propagation rate in M-M versus M-F-M. Therefore, the CV is decreased after inserting a fibroblast between myocytes. This decrease becomes greater with a larger G_{gap} or more fibroblasts.

Because the cells in the block zone have a low excitability, a conduction block can first be observed in the block zone region after inserting one or more fibroblasts in the 2D tissue. With the increase in the coupling fibroblast number or coupling strength, the conduction block spreads to the atrial septum and then the whole atrium.

Chapter 5. Discussions and Conclusions

In this thesis, cellular models of fibroblast–myocyte coupling in the SAN and atrium have been developed to explore the mechanism underlying the coupling and the effects of coupling fibroblast number and coupling strength on electrical activity in the coupled myocyte. At the tissue level, a 2D SAN-atrium tissue model has been used to study the effects of coupling fibroblast number and coupling strength on AP initiation and propagation.

5.1 Main Findings

5.1.1 Investigation of Coupling Effects in Cellular Models

Fibroblasts play double roles in the myocyte–fibroblast coupling. When the membrane potential of a myocyte is higher than that of a fibroblast, the fibroblast acts as a passive load, currents flow from the myocyte to the fibroblast via gap junction channels to charge the fibroblast, elevating the membrane potential of the fibroblast. Once the membrane potential of the fibroblast becomes more positive, the fibroblast works as a current source and the currents flow back to the myocyte. The AP waveform of a coupled myocyte can be modulated by the fibroblast by these two different processes.

In the SAN centre, the coupling exerts a significant effect on the AP waveform of coupled myocytes, resulting in a less depolarised PA, a less negative MDP, a prolonged APD_{90}, and a decreased dV/dt_{max}. Meanwhile, the total transmembrane current and each individual current in the myocytes are weakened to different degrees. The modulations become more significant after coupling with a larger G_{gap} or coupling number. The spontaneous activity is abolished when G_{gap} is larger than 0.18 nS (with one fibroblast).

In the SAN periphery and atrium, because of the different electrophysiological properties of myocytes, the coupling effect becomes less significant. The effects of G_{gap} and coupling fibroblast number on AP characteristics are similar to those in the SAN centre under weak coupling (G_{gap} < 0.2 nS), while the APD_{90} shows different changes after coupling with a larger G_{gap} or more fibroblasts under strong coupling, which can be attributed to the slower charging process of fibroblasts in the PSAN and atrium models.

In M-nF-M connections, while interconnecting the myocytes simply by one fibroblast, the AP of the last myocyte can be activated only if G_{gap} is in the range of 6 nS to 30 nS. The PA and dV/dt_{max} in both myocytes arrive at the same value when G_{gap} is 18 nS. When interconnecting the myocytes with a strand of fibroblasts, the activation time for the last myocyte increases along with the fibroblast number.

5.1.2 Investigation of Coupling Effects in Tissue Models

In the attachment models, with the increase in coupling strength and coupling number, the pacemaking CL is prolonged; the AT for each coupled myocyte is increased; and the CV is increased in coupling areas because of the reduction in dV/dt_{max} of coupled myocytes. No conduction block occurs in both the FASN and FAT models even with a large G_{gap} of 9 nS when coupling to one fibroblast. A half block emerges in the SAN towards the atrial muscle direction (Figure 4.5G) when coupling with seven fibroblasts (G_{gap} = 3 nS) in the FASN model. This may be because there are more CSAN cells and fewer PSAN cells in the SAN towards the atrial muscle than those in the SAN towards the atrial septum. In the FAT case, the conductions are blocked in both directions under the same coupling conditions.

In the decoupling model, the insertion of fibroblasts reduces the electrical communication between myocytes by separating the connected myocytes; as a result, the CV is decreased dramatically, the AT is prolonged, and the pacemaking CL is increased.

In the insertion model, the effects of fibroblasts on the CV become more complicated in the SAN. The CV is increased in the CSAN by enhancing the coupling between myocytes with a small number of interconnecting fibroblasts. In the PSAN and atrium, the CV is decreased after the insertion of fibroblasts. This may be because the new conduction pathway (M-nF-M) formed by the inserted fibroblasts takes more time to conduct AP between myocytes. Because of the low excitability of cells in the block zone, it works as a passive load on the conduction system in the tissue. Therefore, after coupling with a larger coupling strength or more fibroblasts, a conduction block occurs first in the block zone region and then spreads to the atrial septum in the FIT model (Figure 4.7 F and H).

5.2 Biomedical Implications

As suggested by our study, fibroblasts can modify APA, APD, and dV/dt_{max} in the AP waveform, modulate the spontaneous activity in pacemaker cells, and change the AT and CV during the AP propagation in cardiac tissue. The extent of these changes is highly dependent on the electrophysiological properties of coupled myocytes, the coupling number, and the coupling strength. Our simulations have shown how fibroblasts modify the electrical activity in myocytes and even AP conduction in tissue. Thus, is it possible in the future to target fibroblasts as a novel therapeutic approach to prevent some fibrosis-associated heart diseases such as atrial fibrillation, heart failure, and arrhythmias by modulating the electrical activity in the myocytes?

It has been proposed to use therapeutic interventions targeting fibroblast coupling to reduce cardiac fibrosis to diminish the risks of arrhythmia in diseased hearts [77]. For example, Roell et al. illustrated that post-infarct arrhythmia can be prevented by engrafting Cx43-expressing non-myocytes into ventricular scars of mice [16]. Inducing scar tissue (which contains abundant fibroblasts) in the arrhythmogenic region in the atria or ventricles has also been proved to eliminate arrhythmias according to some clinical findings [67], [78], [79]. However, how much of the positive effects were caused by electrical coupling between myocytes and fibroblasts is still unknown, so more detailed research on the pathophysiology of fibroblast–myocyte coupling still needs to be conducted.

5.3 Limitations and Future Work

1. The SAN model we used in our simulation did not incorporate some currents known be present in SAN[44], [70], [80] such as the sustained current (I_{st}), the ACh-activated K^+ current ($I_{K,ACh}$), and the Ca^{2+}-dependent inactivation of I_{CaL}

2. The fibroblast model we used in our simulation is adapted from MacCannell's ventricular fibroblast model. However, It has been demonstrated *in vitro* experiment that the atrial fibroblasts have some different electrophysiological properties with the ventricular fibroblasts [81], [82]. For example, K^+ current in atrial fibroblasts are thought to be not as large as in ventricular fibroblast. New models of fibroblast in SAN and atrium can be developed in the future as more experimental data are available.

3. The membrane potential of cardiac fibroblasts have been proved be sensitive to the mechanical stimuli [81]. The mechano-electrical feedback from fibroblast can increases the pacemaking rate by altering the membrane potential and ion concentration of myocyte in SAN, but in our simulation we didn't include the mechanosensitive currents in our fibroblast model.

4. In our 2D simulation the anatomic geometry we used is just a small section of rabbit atria. A larger 2D geometry or 3D whole heart geometry can be used to investigate the coupling effects on the patterns of AP initiation and propagation in healthy or diseased heart on whole organ level.

5. It has been demonstrated that the cardiac fibroblasts intersperse with myocytes in some areas with low fibroblast density, but form island-like clusters in SAN and atrial tissue in some areas with a high fibroblast density[35], [69]. Therefore, a tissue model with fibroblast islands randomly distributed needs to be developed in a future study.

References

[1] K. E. Barrett, S. M. Barman, S. Boitano, and H. Brooks, *Ganong's Review of Medical Physiology, Twenty-Fifth Edition*, 25 edition. McGraw-Hill Education / Medical, 2015.

[2] H. Gray and W. H. Lewis, 'Anatomy of the human body. 20th', *Ed. Phila. Lea Febiger–New York*, 1918.

[3] V. Kumar, A. K. Abbas, and N. Fausto, 'Robbins and Cotran Pathologic Basis of Disease (7th edn) Saunders Elsevier', *Phila. PA*, 2005.

[4] A. Keith and M. Flack, 'The Form and Nature of the Muscular Connections between the Primary Divisions of the Vertebrate Heart', *J. Anat. Physiol.*, vol. 41, no. Pt 3, pp. 172–189, Apr. 1907.

[5] W. Trautwein and K. Uchizono, 'Electron microscopic and electrophysiologic study of the pacemaker in the sino-atrial node of the rabbit heart', *Z. Für Zellforsch. Mikrosk. Anat.*, vol. 61, no. 1, pp. 96–109, 1963.

[6] A. M. G. L. De Mazière, A. C. G. van Ginneken, R. Wilders, H. J. Jongsma, and L. N. Bouman, 'Spatial and functional relationship between myocytes and fibroblasts in the rabbit sinoatrial node', *J. Mol. Cell. Cardiol.*, vol. 24, no. 6, pp. 567–578, Jun. 1992.

[7] M. R. Boyett, H. Honjo, and I. Kodama, 'The sinoatrial node, a heterogeneous pacemaker structure', *Cardiovasc. Res.*, vol. 47, no. 4, pp. 658–687, Sep. 2000.

[8] W. K. Bleeker, A. J. Mackaay, M. Masson-Pévet, L. N. Bouman, and A. E. Becker, 'Functional and morphological organization of the rabbit sinus node.', *Circ. Res.*, vol. 46, no. 1, pp. 11–22, Jan. 1980.

[9] S. E. Campbell, A. M. Gerdes, and T. D. Smith, 'Comparison of regional differences in cardiac myocyte dimensions in rats, hamsters, and guinea pigs', *Anat. Rec.*, vol. 219, no. 1, pp. 53–59, Sep. 1987.

[10] J. M. Cordeiro, K. W. Spitzer, and W. R. Giles, 'Repolarizing K+ currents in rabbit heart Purkinje cells', *J. Physiol.*, vol. 508, no. Pt 3, pp. 811–823, May 1998.

[11] C. A. Walker and F. G. Spinale, 'The structure and function of the cardiac myocyte: A review of fundamental concepts', *J. Thorac. Cardiovasc. Surg.*, vol. 118, no. 2, pp. 375–382, Aug. 1999.

[12] E. E. Verheijck, A. Wessels, A. C. G. van Ginneken, J. Bourier, M. W. M. Markman, J. L. M. Vermeulen, J. M. T. de Bakker, W. H. Lamers, T. Opthof, and L. N. Bouman, 'Distribution of Atrial and Nodal Cells Within the Rabbit Sinoatrial Node Models of Sinoatrial Transition', *Circulation*, vol. 97, no. 16, pp. 1623–1631, Apr. 1998.

[13] M. A. Colman, 'Pacemaking and Autonomic Regulation in the 3D Sinoatrial Node and Atria', in *Mechanisms of Atrial Arrhythmias*, Springer International Publishing, 2014, pp. 185–199.

[14] E. Ongstad and P. Kohl, 'Fibroblast-myocyte coupling in the heart: Potential relevance for therapeutic interventions', *J. Mol. Cell. Cardiol.*, vol. 91, pp. 238–246, Feb. 2016.

[15] B. W. Doble and E. Kardami, 'Basic fibroblast growth factor stimulates connexin-43 expression and intercellular communication of cardiac fibroblasts', *Mol. Cell. Biochem.*, vol. 143, no. 1, pp. 81–87, Feb. 1995.

[16] W. Roell, T. Lewalter, P. Sasse, Y. N. Tallini, B. R. Choi, M. Breitbach, R. Doran, U. M. Becher, S. M. Hwang, T. Bostani, J. von Maltzahn, A. Hofmann, S. Reining, B. Eiberger, B. Gabris, A. Pfeifer, A. Welz, K. Willecke, G. Salama, J. W. Schrickel, M. I. Kotlikoff, and B. K. Fleischmann, 'Engraftment of connexin

43-expressing cells prevents post-infarct arrhythmia', *Nature*, vol. 450, no. 7171, pp. 819–824, 2007.
[17] H. Dobrzynski, M. R. Boyett, and R. H. Anderson, 'New Insights Into Pacemaker Activity Promoting Understanding of Sick Sinus Syndrome', *Circulation*, vol. 115, no. 14, pp. 1921–1932, Apr. 2007.
[18] C. A. Souders, S. L. K. Bowers, and T. A. Baudino, 'Cardiac Fibroblast The Renaissance Cell', *Circ. Res.*, vol. 105, no. 12, pp. 1164–1176, Dec. 2009.
[19] J. D. Lajiness and S. J. Conway, 'Origin, development, and differentiation of cardiac fibroblasts', *J Mol Cell Cardiol*, vol. 70, pp. 2–8, 2014.
[20] B. Hille, *Ion channels of excitable membranes. Sunderland, MA*. Sinauer Associates, Inc, 2001.
[21] M. A. Colman, 'Development of a New Model for Simulating the Electrical Action Potentials of Human Atrial Myocytes', in *Mechanisms of Atrial Arrhythmias*, Springer International Publishing, 2014, pp. 59–85.
[22] A. O. Grant, 'Cardiac Ion Channels', *Circ. Arrhythm. Electrophysiol.*, vol. 2, no. 2, pp. 185–194, Apr. 2009.
[23] R. Klabunde, *Cardiovascular Physiology Concepts*. Lippincott Williams & Wilkins, 2011.
[24] P. Camelliti, 'Fibroblast Network in Rabbit Sinoatrial Node: Structural and Functional Identification of Homogeneous and Heterogeneous Cell Coupling', *Circ. Res.*, vol. 94, no. 6, pp. 828–835, Apr. 2004.
[25] M. B. Rook, A. C. Van Ginneken, B. e de Jonge, A. El Aoumari, D. Gros, and H. J. Jongsma, 'Differences in gap junction channels between cardiac myocytes, fibroblasts, and heterologous pairs', *Am. J. Physiol.-Cell Physiol.*, vol. 263, no. 5, pp. C959–C977, 1992.
[26] G. Gaudesius, 'Coupling of Cardiac Electrical Activity Over Extended Distances by Fibroblasts of Cardiac Origin', *Circ. Res.*, vol. 93, no. 5, pp. 421–428, Sep. 2003.
[27] M. Miragoli, G. Gaudesius, and S. Rohr, 'Electrotonic modulation of cardiac impulse conduction by myofibroblasts', *Circ Res*, vol. 98, no. 6, pp. 801–810, 2006.
[28] L. Chilton, W. R. Giles, and G. L. Smith, 'Evidence of intercellular coupling between co-cultured adult rabbit ventricular myocytes and myofibroblasts', *J. Physiol.*, vol. 583, no. 1, pp. 225–236, Aug. 2007.
[29] Y. Zhang, E. M. Kanter, J. G. Laing, C. Aprhys, D. C. Johns, E. Kardami, and K. A. Yamada, 'Connexin43 expression levels influence intercellular coupling and cell proliferation of native murine cardiac fibroblasts', *Cell Commun Adhes*, vol. 15, no. 3, pp. 289–303, 2008.
[30] C. Vasquez, P. Mohandas, K. L. Louie, N. Benamer, A. C. Bapat, and G. E. Morley, 'Enhanced Fibroblast–Myocyte Interactions in Response to Cardiac Injury', *Circ. Res.*, vol. 107, no. 8, pp. 1011–1020, Oct. 2010.
[31] P. Camelliti, T. K. Borg, and P. Kohl, 'Structural and functional characterisation of cardiac fibroblasts', *Cardiovasc Res*, vol. 65, no. 1, pp. 40–51, 2005.
[32] N. L. Walker, F. L. Burton, S. Kettlewell, G. L. Smith, and S. M. Cobbe, 'Mapping of Epicardial Activation in a Rabbit Model of Chronic Myocardial Infarction: Response to Atrial, Endocardial and Epicardial Pacing', J. Cardiovasc. Electrophysiol., vol. 18, no. 8, pp. 862–868, Aug. 2007.
[33] P. C. Ursell, P. I. Gardner, A. Albala, J. J. Fenoglio, and A. L. Wit, 'Structural and electrophysiological changes in the epicardial border zone of canine

myocardial infarcts during infarct healing.', *Circ. Res.*, vol. 56, no. 3, pp. 436–451, Mar. 1985.
[34] F. Persson, B. Andersson, G. Duker, I. Jacobson, and L. Carlsson, 'Functional effects of the late sodium current inhibition by AZD7009 and lidocaine in rabbit isolated atrial and ventricular tissue and Purkinje fibre', *Eur. J. Pharmacol.*, vol. 558, no. 1–3, pp. 133–143, 2007.
[35] E. Ongstad and P. Kohl, 'Fibroblast–myocyte coupling in the heart: Potential relevance for therapeutic interventions', *J. Mol. Cell. Cardiol.*
[36] I. J. LeGrice, B. H. Smaill, L. Z. Chai, S. G. Edgar, J. B. Gavin, and P. J. Hunter, 'Laminar structure of the heart: ventricular myocyte arrangement and connective tissue architecture in the dog', *Am J Physiol*, vol. 269, no. 2 Pt 2, pp. H571–82, 1995.
[37] M. Aguilar, X. Y. Qi, H. Huang, P. Comtois, and S. Nattel, 'Fibroblast electrical remodeling in heart failure and potential effects on atrial fibrillation', *Biophys J*, vol. 107, no. 10, pp. 2444–2455, 2014.
[38] M. Abrial, C. C. Da Silva, B. Pillot, L. Augeul, F. Ivanes, G. Teixeira, R. Cartier, D. Angoulvant, M. Ovize, and R. Ferrera, 'Cardiac fibroblasts protect cardiomyocytes against lethal ischemia–reperfusion injury', *J Mol Cell Cardiol*, vol. 68, pp. 56–65, 2014.
[39] E. A. Rog-Zielinska, R. A. Norris, P. Kohl, and R. Markwald, 'The Living Scar – Cardiac Fibroblasts and the Injured Heart', *Trends Mol. Med.*, vol. 22, no. 2, pp. 99–114, Feb. 2016.
[40] A. L. Hodgkin, A. F. Huxley, and B. Katz, 'Measurement of current-voltage relations in the membrane of the giant axon of Loligo', *J. Physiol.*, vol. 116, no. 4, pp. 424–448, Apr. 1952.
[41] A. L. Hodgkin and A. F. Huxley, 'A quantitative description of membrane current and its application to conduction and excitation in nerve', *J. Physiol.*, vol. 117, no. 4, pp. 500–544, Aug. 1952.
[42] M. D. Archer, 'Genesis of the Nernst Equation', in *Electrochemistry, Past and Present*, vol. 390, 0 vols, American Chemical Society, 1989, pp. 115–126.
[43] P. Colli Franzone, L. F. Pavarino, and B. Taccardi, 'Simulating patterns of excitation, repolarization and action potential duration with cardiac Bidomain and Monodomain models', *Math. Biosci.*, vol. 197, no. 1, pp. 35–66, Sep. 2005.
[44] H. Zhang, A. V. Holden, I. Kodama, H. Honjo, M. Lei, T. Varghese, and M. R. Boyett, 'Mathematical models of action potentials in the periphery and center of the rabbit sinoatrial node', *Am J Physiol Heart Circ Physiol*, vol. 279, no. 1, pp. H397–421, 2000.
[45] F. H. Fenton, E. M. Cherry, A. Karma, and W.-J. Rappel, 'Modeling wave propagation in realistic heart geometries using the phase-field method', *Chaos Interdiscip. J. Nonlinear Sci.*, vol. 15, no. 1, p. 13502, Mar. 2005.
[46] T. D. Butters, O. V. Aslanidi, S. Inada, M. R. Boyett, J. C. Hancox, M. Lei, and H. Zhang, 'Mechanistic Links Between Na+ Channel (SCN5A) Mutations and Impaired Cardiac Pacemaking in Sick Sinus Syndrome', *Circ. Res.*, vol. 107, no. 1, pp. 126–137, Jul. 2010.
[47] J. P. Fahrenbach, R. Mejia-Alvarez, and K. Banach, 'The relevance of non-excitable cells for cardiac pacemaker function', *J. Physiol.*, vol. 585, no. Pt 2, pp. 565–578, Dec. 2007.
[48] J. G. F. Cleland, S. Chattopadhyay, A. Khand, T. Houghton, and G. C. Kaye, 'Prevalence and Incidence of Arrhythmias and Sudden Death in Heart Failure', *Heart Fail. Rev.*, vol. 7, no. 3, pp. 229–242, Jul. 2002.

[49] L. C. McSpadden, R. D. Kirkton, and N. Bursac, ‘Electrotonic loading of anisotropic cardiac monolayers by unexcitable cells depends on connexin type and expression level’, *Am. J. Physiol. - Cell Physiol.*, vol. 297, no. 2, pp. C339–C351, Aug. 2009.
[50] P. Kohl, A. G. Kamkin, I. S. Kiseleva, and D. Noble, ‘Mechanosensitive fibroblasts in the sino-atrial node region of rat heart: interaction with cardiomyocytes and possible role’, *Exp Physiol*, vol. 79, no. 6, pp. 943–956, 1994.
[51] K. A. MacCannell, H. Bazzazi, L. Chilton, Y. Shibukawa, R. B. Clark, and W. R. Giles, ‘A mathematical model of electrotonic interactions between ventricular myocytes and fibroblasts’, *Biophys J*, vol. 92, no. 11, pp. 4121–4132, 2007.
[52] M. M. Maleckar, J. L. Greenstein, W. R. Giles, and N. A. Trayanova, ‘Electrotonic Coupling between Human Atrial Myocytes and Fibroblasts Alters Myocyte Excitability and Repolarization’, *Biophys. J.*, vol. 97, no. 8, pp. 2179–2190, Oct. 2009.
[53] Y. Xie, A. Garfinkel, J. N. Weiss, and Z. Qu, ‘Cardiac alternans induced by fibroblast-myocyte coupling: mechanistic insights from computational models’, *Am. J. Physiol. - Heart Circ. Physiol.*, vol. 297, no. 2, pp. H775–H784, Aug. 2009.
[54] H. Zhang, A. V. Holden, D. Noble, and M. R. Boyett, ‘Analysis of the Chronotropic Effect of Acetylcholine on Sinoatrial Node Cells’, *J. Cardiovasc. Electrophysiol.*, vol. 13, no. 5, pp. 465–474, May 2002.
[55] D. S. Lindblad, C. R. Murphey, J. W. Clark, and W. R. Giles, ‘A model of the action potential and underlying membrane currents in a rabbit atrial cell’, *Am. J. Physiol. - Heart Circ. Physiol.*, vol. 271, no. 4, pp. H1666–H1696, Oct. 1996.
[56] O. V. Aslanidi, M. R. Boyett, H. Dobrzynski, J. Li, and H. Zhang, ‘Mechanisms of Transition from Normal to Reentrant Electrical Activity in a Model of Rabbit Atrial Tissue: Interaction of Tissue Heterogeneity and Anisotropy’, *Biophys. J.*, vol. 96, no. 3, pp. 798–817, Apr. 2009.
[57] A. Kamkin, I. Kiseleva, K.-D. Wagner, A. Pylaev, K. P. Leiterer, H. Theres, H. Scholz, J. Günther, and G. Isenberg, ‘A possible role for atrial fibroblasts in postinfarction bradycardia’, *Am. J. Physiol. - Heart Circ. Physiol.*, vol. 282, no. 3, pp. H842–H849, Mar. 2002.
[58] J. Davis and J. D. Molkentin, ‘Myofibroblasts: trust your heart and let fate decide’, *J Mol Cell Cardiol*, vol. 70, pp. 9–18, 2014.
[59] M. de Marneffe, J. M. Gregoire, P. Waterschoot, and M. P. Kestemont, ‘The sinus node and the autonomic nervous system in normals and in sick sinus patients’, *Acta Cardiol.*, vol. 50, no. 4, pp. 291–308, 1995.
[60] I. Shiraishi, T. Takamatsu, T. Minamikawa, Z. Onouchi, and S. Fujita, ‘Quantitative histological analysis of the human sinoatrial node during growth and aging’, *Circulation*, vol. 85, no. 6, pp. 2176–2184, 1992.
[61] F. B. Sachse, A. P. Moreno, and J. A. Abildskov, ‘Electrophysiological Modeling of Fibroblasts and their Interaction with Myocytes’, *Ann. Biomed. Eng.*, vol. 36, no. 1, pp. 41–56, Nov. 2007.
[62] M. Miragoli, N. Salvarani, and S. Rohr, ‘Myofibroblasts Induce Ectopic Activity in Cardiac Tissue’, *Circ. Res.*, vol. 101, no. 8, pp. 755–758, Oct. 2007.
[63] L. Yue, J. Xie, and S. Nattel, ‘Molecular determinants of cardiac fibroblast electrical function and therapeutic implications for atrial fibrillation’, *Cardiovasc Res*, vol. 89, no. 4, pp. 744–753, 2011.
[64] J. Pellman, J. Zhang, and F. Sheikh, ‘Myocyte-fibroblast communication in cardiac fibrosis and arrhythmias: Mechanisms and model systems’, *J. Mol. Cell. Cardiol.*, vol. 94, pp. 22–31, May 2016.

[65] T. A. Baudino, W. Carver, W. Giles, and T. K. Borg, ‘Cardiac fibroblasts: friend or foe?’, *Am. J. Physiol. - Heart Circ. Physiol.*, vol. 291, no. 3, pp. H1015–H1026, Sep. 2006.
[66] S. A. Clarke, W. J. Richardson, and J. W. Holmes, ‘Modifying the mechanics of healing infarcts: Is better the enemy of good?’, *J. Mol. Cell. Cardiol.*, vol. 93, pp. 115–124, Apr. 2016.
[67] B. Dinov, A. Arya, L. Bertagnolli, V. Schirripa, K. Schoene, P. Sommer, A. Bollmann, S. Rolf, and G. Hindricks, ‘Early Referral for Ablation of Scar-Related Ventricular Tachycardia Is Associated With Improved Acute and Long-Term Outcomes Results From the Heart Center of Leipzig Ventricular Tachycardia Registry’, *Circ. Arrhythm. Electrophysiol.*, vol. 7, no. 6, pp. 1144–1151, Dec. 2014.
[68] V. Jacquemet and C. S. Henriquez, ‘Modelling cardiac fibroblasts: interactions with myocytes and their impact on impulse propagation’, *EP Eur.*, vol. 9, no. suppl 6, p. vi29-vi37, Nov. 2007.
[69] V. Jacquemet and C. S. Henriquez, ‘Loading effect of fibroblast-myocyte coupling on resting potential, impulse propagation, and repolarization: insights from a microstructure model’, *Am J Physiol Heart Circ Physiol*, vol. 294, no. 5, pp. H2040–52, 2008.
[70] R. V. Oren and C. E. Clancy, ‘Determinants of Heterogeneity, Excitation and Conduction in the Sinoatrial Node: A Model Study’, *PLOS Comput Biol*, vol. 6, no. 12, p. e1001041, Dec. 2010.
[71] S. Zlochiver, V. Muñoz, K. L. Vikstrom, S. M. Taffet, O. Berenfeld, and J. Jalife, ‘Electrotonic Myofibroblast-to-Myocyte Coupling Increases Propensity to Reentrant Arrhythmias in Two-Dimensional Cardiac Monolayers’, *Biophys. J.*, vol. 95, no. 9, pp. 4469–4480, Nov. 2008.
[72] A. Greisas and S. Zlochiver, ‘Modulation of spiral-wave dynamics and spontaneous activity in a fibroblast/myocyte heterocellular tissue–a computational study’, *IEEE Trans Biomed Eng*, vol. 59, no. 5, pp. 1398–1407, 2012.
[73] H. Dobrzynski, J. Li, J. Tellez, I. D. Greener, V. P. Nikolski, S. E. Wright, S. H. Parson, S. A. Jones, M. K. Lancaster, M. Yamamoto, H. Honjo, Y. Takagishi, I. Kodama, I. R. Efimov, R. Billeter, and M. R. Boyett, ‘Computer Three-Dimensional Reconstruction of the Sinoatrial Node’, *Circulation*, vol. 111, no. 7, pp. 846–854, Feb. 2005.
[74] H. Zhang, Y. Zhao, M. Lei, H. Dobrzynski, J. H. Liu, A. V. Holden, and M. R. Boyett, ‘Computational evaluation of the roles of Na+ current, iNa, and cell death in cardiac pacemaking and driving’, *Am. J. Physiol. - Heart Circ. Physiol.*, vol. 292, no. 1, pp. H165–H174, Jan. 2007.
[75] T. D. Butters, ‘Development of a virtual 3D sheep atria for the study of clinical atrial fibrillation’, University of Manchester, 2012.
[76] P. Kohl and P. Camelliti, ‘Fibroblast–myocyte connections in the heart’, *Heart Rhythm*, vol. 9, no. 3, pp. 461–464, Mar. 2012.
[77] T. P. Nguyen, Y. Xie, A. Garfinkel, Z. Qu, and J. N. Weiss, ‘Arrhythmogenic consequences of myofibroblast-myocyte coupling’, *Cardiovasc Res*, vol. 93, no. 2, pp. 242–251, 2012.
[78] H. Ghanbari, K. Baser, M. Yokokawa, W. Stevenson, P. D. Bella, P. Vergara, T. Deneke, K.-H. Kuck, H. Kottkamp, S. Fei, F. Morady, and F. Bogun, ‘Noninducibility in Postinfarction Ventricular Tachycardia as an End Point for

Ventricular Tachycardia Ablation and Its Effects on Outcomes A Meta-Analysis', *Circ. Arrhythm. Electrophysiol.*, vol. 7, no. 4, pp. 677–683, Aug. 2014.
[79] V. M. Mahoney, V. Mezzano, and G. E. Morley, 'A review of the literature on cardiac electrical activity between fibroblasts and myocytes', *Prog. Biophys. Mol. Biol.*, vol. 120, no. 1–3, pp. 128–133, Jan. 2016.
[80] Y. Kurata, I. Hisatome, S. Imanishi, and T. Shibamoto, 'Dynamical description of sinoatrial node pacemaking: improved mathematical model for primary pacemaker cell', *Am. J. Physiol. - Heart Circ. Physiol.*, vol. 283, no. 5, pp. H2074–H2101, Nov. 2002.
[81] A. Kamkin, I. Kiseleva, and G. Isenberg, 'Activation and inactivation of a non-selective cation conductance by local mechanical deformation of acutely isolated cardiac fibroblasts', *Cardiovasc. Res.*, vol. 57, no. 3, pp. 793–803, Mar. 2003.
[82] B. Burstein, E. Libby, A. Calderone, and S. Nattel, 'Differential Behaviors of Atrial Versus Ventricular Fibroblasts A Potential Role for Platelet-Derived Growth Factor in Atrial-Ventricular Remodeling Differences', *Circulation*, vol. 117, no. 13, pp. 1630–1641, Apr. 2008.